MAGNETIC STUDIES BY USING A COMBINED ^{3}HE AND MAGNETIC COOLING SYSTEM BELOW 1 K

by

KAZUO KADOWAKI

Submitted to the Graduate School of Science in
Partial Fulfilment of the Requirements
for
the Degree
of
Doctor of Science
Osaka University
1980

Contents

Part I

Technics for ESR and Magnetization Measurements below 1 K

Synopsis

A new cryostat using a combined system of ^3He and adiavatic demagnetization for ESR measurements below 1 K was developed as shown in A. ESR measurements can easily be done from 24 GHz to 47 GHz down to about 100 mK with good temperature stability around ^3He temperature region. In order to measure the sample temperature just on resonance, AFMR line shift in a typical antiferromagnet $RbMnF_3$ was measured and the temperature increase of the sample was estimated. Two kinds of ^3He cryostat using the fluxgate magnetometer for the magnetization measurements were constructed as shown in B. One of them can measure the temperature dependence of the magnetization in a constant field and another one can be used for measuring the magnetization curve by moving the sample in a various fixed field at a constant temperature. As these systems can detect the magnetization change of about $10^{-3} \sim 10^3$ Gauss, they can be applied for almost all magnetization measurements of weak paramagnets as well as ferromagnets. A carbon resistance thermometer (50 mK $\sim$ 4.2 K) which is calibrated by measuring CMN susceptibility by Hartshorn mutual inductance bridge and a calibrated germanium thermometer (0.5 K $\sim$ 1 K) used for ESR and magnetization measurements are described in C.

A ESR Cryostat below 1 K Using A Combined ^{3}He and Adiabatic Demagnetization System

§ 1 Introduction

Many low-dimensional antiferromagnets have their three-dimensional magnetic ordering temperature T_N below 1 K, because of the weak exchange interaction between magnetic chains or layers. In the short range order region near T_N, the shift and broadening of the ESR line, which are characteristics of the low dimensional magnets, have been observed by previous ESR measurements.[1)-5)] In order to investigate the magnetism of these magnets at low temperatures, especially, the spin dynamics and cooperative excitations in the spin systems below T_N, it is necessary to construct the ESR cryostat which operates in wide frequency and temperature region below 1 K.

So far, all ESR work[6)-12)] below 1 K has been done by using either a ^{3}He refrigerator or an adiabatic demagnetization method at a single microwave frequency. The lowest ESR temperature obtained by Abe et al.[12)] using the adiabatic demagnetization method is about 40 mK while the lowest data for ^{3}He cryostat is 250 mK.[10)] In general, ^{3}He cryostat is simple and useful for ESR measurements down to near 0.3 K, and the temperature is easily controlled. On the other hand, a lower temperature can be obtained in the adiabatic demagnetization method. However, the temperature increase of this method in the ^{3}He temperature region (0.4 K $\sim$ 1 K) is too fast to take ESR data because of the

fact that the specific heat of the paramagnetic salt is small near 1 K. Desorption of ^{4}He gas adsorbed on the salt also promotes the heating of the specimen. The most favorable method is use of a dilution refrigerator but this method is too complicated in handling and needs a large quantity of liquid ^{4}He. So, we combined the ^{3}He refrigerator with the adiabatic demagnetization system to cover a wide ESR temperature region with desirable stability below 1 K. The ESR cryostat constructed is compact and includes two superconducting magnets for ESR and demagnetization. Liquid ^{4}He of only 2.5 litters is used for one cycle operation, as will be described in the next section. A wide frequency range of 24 $\sim$ 47 GHz is covered by changing the length of rectangular cavity in our ESR cryostat and it is useful especially for the antiferromagnetic resonance (AFMR). Detailed constructions of the cryostat and its operations are described in §2 and §3, respectively.

In the ESR measurements below 1 K, estimation of the sample temperature is an important problem. When the sample absorbs the microwave power on the resonance absorption, the temperature in the sample increases isolately from the sample holder. The presence of Kapitza thermal boundary resistance between the sample and its holder is important in this case. As a new experimental method to estimate the sample temperature, the hyperfine shift of AFMR line in a cubic antiferromagnet $RbMnF_3$ was introduced in the present study. Detailed results and discussions on this method are given in §3.

§ 2 Apparatus

(1) Cryostat

In our combined ^{3}He and adiabatic demagnetization refrigerator the ^{3}He system works in one-shot cycle. Outline of the cryostat is shown in Fig. 1. ^{3}He gas is pumped by a shaft-sealed rotary pump of 150 litters/min. through a stainless steel pipe J of 9.5 mm I.D. in the figure. The pumping speed is controlled by the valve B. The pipe E is a stainless steel tube of 12.5 mm I.D. for evacuating the vacuum can V. The symbol A in Fig. 1 is the valve for the evacuating line. A German silver waveguide WRJ-320 is passed through the pipe E and cut in two pieces separated by a few millimeters. These two pieces of german silver waveguide are connected with a slightly large rectangular sleeve, which is soldered to one piece of the waveguide, so as to absorb the difference in thermal expansion of the waveguide and that of the stainless steel tube E. The lower piece of German silver waveguide is soldered to copper waveguide M which is inside the vacuum can V and thermally anchored on a copper rod L at 1.2 K. The radiation through the waveguide is shielded by bending the waveguide M. The vacuum seal for the waveguide is done by the quartz plate of 0.5 mm in thickness at the top of the pipe E at which the copper waveguide C coming from the ESR spectrometer is connected by a frange. The lead wires for the electrical resistance measurements in thermometers such as carbon resistors are also passed through the pipe E. These wires are thermally anchored on a copper rod L at 1.2 K, and they come out through

a hermetic seal D at the top of the cryostat. Liquid ^{4}He is transferred through a pipe H. Two superconducting magnets N and U for the ESR measurements and the demagnetization, respectively, are suspended from the ring plate K. The symbol W in Fig. 1 shows the persistent current mode switch for the superconducting magnet U. The symbol G shows the liquid nitrogen pot. The inlet and outlet pipes to the pot are not drawn in the figure to avoid complication. This pot works effectively as the first thermal sink for the pipes E, J and H, and the lead wires F of the superconducting magnets. The spirally wound part Y of the leads works as the second heat exchanger with cold helium vapor so as to decrease the heat inflow.

Detailed constructions in the vacuum can V is shown in Fig. 2a. The vacuum can is made of SUS 304 stainless steel with 25 mm O.D. and 0.5 mm wall thickness, and attached to the vacuum jacket O by Wood metal. A cylindrical ^{3}He evaporation pot P with a concentric hole of 5 mm in diameter is suspended by the ^{3}He pumping CuNi tube I of 3 mm I.D. × 80 mm in length. The upper end of tube I is connected to the pipe J in Fig. 1 through the radiation shield. The pot P is made of pure copper and has thin fins inside the inner wall as shown in Fig. 2a to increase the contact area with liquid ^{3}He. The capacity of the pot is about 3 cm^3. The bottom of ^{3}He pot has a screw structure to support the salt pill for the demagnetization or to attach the constructions for any other purposes such as resistance or magnetization measurements. The salt pill S for adiabatic demagnetization is constructed from a Bakelite pipe (21 mm O.D., 20 mm I.D. and 130 mm in length) in which about 40 grams of ferric ammonium alum, $FeNH_4(SO_4)_2 \cdot 12\ H_2O$, and about

2000 copper wires of 0.05 mm in diameter are stuffed with thermal contact agent Apiezon J oil. This salt pill S is suspended by the teflon supporter X from the ^{3}He evaporation pot with the screw construction as mentioned above. The fine copper wires out of the salt are bundled at the top of the pill and solidified by the epoxy resin. This strand of copper wires passes through the hole of the cylindrical ^{3}He pot without contact and serves as the thermal link Z between the salt pill and the cavity Q. The connection between the cavity Q and the thermal link Z is done by silver soldering or by tight screw connection. The cavity Q is made of a piece of copper waveguide and resonates on TE_{102} mode. For setting the sample the bottom wall is separated from the cavity at the position of a quarter wave length as schematically shown in Fig. 2b. The cavity Q is cut off about 2 mm from the waveguide M in order to avoid the heat inflow. This cut-off of the waveguide is one of the essential points in the ESR cryostat below 1 K. A wide ESR frequency range above the cut-off frequency of the waveguide WRJ-320, 24 $\sim$ 47 GHz is covered by changing the cavity. The sample is grewed on to the bottom of the cavity by Apiezon N grease. The temperatures of the cavity and ^{3}He pot are measured by carbon resistors R which are Matsushita ERC-18SG, 100 Ω at room temperature. The calibration of the carbon resistors was carefully done by measuring ac susceptibility of CMN (Cerium Magnesium Nitrate, $Ce_2Mg_3(NO_3)_{12}\cdot 24H_2O$). The electrical resistance of these carbon resistors was measured by ac bridge method using IT (Instruments for Technology Ltd. in Finland) automatic selfbalancing resistance bridge, and the power dissipation for the measurements

is within 10^{-11} Watt around 0.1 K. The temperature was measured within the error of 0.5 % in the temperature region 0.1 K ∿ 1 K. These carbon resistors are wound by a thin copper plate and attached onto the bottom of the cavity or the top of ^{3}He pot by a small screw as shown in Fig. 2. As the result, the thermal response time was sufficiently short. The temperature of the cavity can be changed by the heater T wound on the thermal link.

(2) ESR Spectrometer

A conventional reflection type spectrometer was used in the present experiments. In the ESR measurements below 1 K, the following points should be noticed : a usual field modulation method is not applicable because of the eddy current heating on the cavity. Another problem is the sample heating due to the presence of Kapitza thermal boundary resistance between the sample and the cavity wall, so the input microwave power must be as low as to be 10^{-7} ∿ 10^{-9} Watt around 0.1 K as discussed in the next section. Considering these restrictions, the spectrometer as shown in Fig. 3 was used. Instead of the field modulation, the microwave power is modulated by superposing the rectangular pulse voltage with 1 kHz repetition to the dc repeller voltage. The klystron does not oscillate under the dc voltage and the pulse voltage is adjusted so as to obtain the maximum oscillation power with the best tuning condition of the whole cavity system[12]. The microwave power is attenuated by two attenuators in series. After receiving by a crystal diode, 1N26, the ESR signal through the PAR-116 preamplifier and PAR-121A lock-in amplifier is displayed in a XY-recorder.

A magnetic field for ESR measurements is supplied by the superconducting magnet which is 85 mm in length, 150 mm O.D. and 25 mm bore-diameter, and its maximum field is about 30 kOe. The field values were calibrated by DPPH absorption signal at frequencies 24 ∿ 47 GHz.

§ 3 Results and Discussions

(1) Operation of The Cryostat

The time variation of the cavity temperature during the actual ESR measurements is shown in Fig. 4. After transferring liquid ^{4}He of 2.5 litters into the glass Dewar, adjustments of the apparatus such as the power balance in the magic-T of the spectrometer is done during the steps A and B in Fig. 4. Then, ESR measurements are performed from 4.2 K to 1.2 K with slowly pumping of liquid ^{4}He by Kenny type rotary pump of 3000 litters/min. (B ∿ C in Fig. 4). After the measurements at 1.2 K, ^{3}He gas is condensed in the ^{3}He pot and the magnet for the adiabatic demagnetization is operated up to about 25 kOe with the persistent current mode (C ∿ D). After the cavity temperature returns to 1.2 K the ^{4}He exchange gas is pumped out. The Kenny pumping line is closed until the temperature of liquid ^{4}He bath increases up to about 2 K so as the exchange gas to be quickly excluded as possible. In this process, D ∿ E in Fig. 4, the cavity temperature increases slightly by the heat conduction through the remained exchange gas and solid construction supporting the cavity. When the vacuum gauge at the

top of the cryostat shows about $1 \sim 2 \times 10^{-6}$ Torr., the pumping line for liquid ^{4}He bath is again opened, and subsequently, the ^{3}He pot reaches at the lowest temperature of about 0.4 K, the magnetic field in the salt is slowly decreased at the rate of about 1 kOe/min. (F $\sim$ G). After the demagnetization, ESR measurements start at G in Fig. 4. The ESR data are taken many times up to 1.2 K (G $\sim$ H). The input microwave power is about 0.1 μW in the present experiment.

(2) Estimation of The Sample Temperature

In the ESR measurements below 1 K, it is verry difficult to determine the temperature of the sample which is on resonance, though the measurements of the cavity temperature are easily done by a thermometer as previously described. When the sample is just on resonance, the sample absorbs the microwave power and the produced heat does not decay because of the Kapitza thermal boundary resistance between the sample and the cavity wall. The heat flow $\dot{Q}$ is proportional to the temperature difference ΔT of the sample T_s and cavity wall T_c as

$$\dot{Q} = \frac{A\Delta T}{R_K}, \qquad (1)$$

where A is the surface area between them and R_K represents the Kapitza resistance. In a single crystal of CrK-alum adhered on the copper foil by Apiezon N grease, for example, the Kapitza resistance is reported as [13),14)]

$$R_K = 4 \times 10^{-6} \cdot T_c^{-3}. \qquad (K \cdot cm^2 \cdot sec/erg) \qquad (2)$$

Therefore, ΔT is given as

$$\Delta T = 4 \times 10^{-6} \cdot \dot{Q}/A \cdot T_c^{3}. \qquad (K) \qquad (3)$$

We get ΔT = 40 mK for the condition that $\dot{Q}$ = 1 erg/sec, T_c = 0.1 K and A = 0.1 cm^2. This means that the sample temperature increases about 40 mK higher than the cavity temperature for the absorbed microwave power of 0.1 μW. In the actual ESR measurements for various substances, however, the Kapitza resistance is not exactly known. Therefore, it becomes necessary to use another more direct method of the temperature measurement for specimens just under the resonance.

To estimate the exact temperature of the specimen, we measured the shift of AFMR line in a cubic antiferromagnet $RbMnF_3$[15),16)]. This shift comes from the temperature dependent nuclear anisotropy field in AFMR[17)]. Below the Néel temperature of 82.6 K the manganese spins in this compound form the two sublattice antiparallel configuration and point in the body-diagonal direction in the absence of the applied field. When the field H_0 is larger than the critical field H_c ≃ 2.5 kOe, the spin axes are perpendicular to H_0. In this state, AFMR ferquency is written as

$$\left(\frac{\omega}{\gamma}\right)^2 = H_0^2 + 2H_E(H_A + H_N), \qquad (4)$$

where H_E and H_A are the exchange and anisotropy fields coming from the electronic origin, and they are usually constant at low temperatures below T_N. H_N is the hyperfine field coming from the Mn nucleus. This field is always parallel to the d-electron spin moment and acts as the dynamical anisotropy field perpendicular to the applied field in the state, $H_0 > H_c$. Then, H_N is written as[17]

$$H_N = \frac{A^2 I(I+1)\langle S\rangle}{3k\hbar\gamma_e} \cdot \frac{1}{T_n}, \qquad \text{(Oe)} \qquad (5)$$

for $AI\langle S\rangle/kT_n \ll 1$, where A is the hyperfine constant, I the nuclear spin, $\langle S\rangle$ the sublattice spin moment which is saturated at low temperatures below T_N, γ_e the gyro-magnetic ratio of the electron spins, and T_n the nuclear spin temperature. In the AFMR measurements with a constant frequency ω, it is expected from eqs. (4) and (5) that the square of resonance field H_0^2 decreases in proportion to $1/T_n$. In these high concentrated manganese compounds, the nuclear spin lattice relaxation time is considered to be short enough[18]. Assuming $T_n \simeq T_s$, one can estimate the sample temperature by using eqs. (4) and (5).

In our AFMR experiments in $RbMnF_3$, the external magnetic field was applied along the cubic axis and the sample of 1 mm × 1 mm × 0.5 mm was tightly grewed onto the bottom of the cavity

wall by the thermal contact agent Apiezon N grease so as a large surface of the sample to be contact with the cavity wall. The incident microwave power to the cavity was attenuated by two attenuators in series to be about 0.1 μW. The typical AFMR lines observed for 32.44 GHz are shown in Fig. 5 for the cavity temperatures from 4.2 K to 0.14 K. The resonance field H_0 shifts to lower field at lower temperatures. The square of observed field H_0^2 are plotted against the inverse of the cavity temperature $1/T_c$ in Fig. 6. It should be noted that the linear relation in H_0^2 vs $1/T_c$ holds down to $T_c \simeq 0.25$ K and deviates from the linear line below about 0.25 K as is shown by a solid line in Fig. 6. As the condition $AI\langle S\rangle/kT_n \ll 1$ should be satisfied down to about above 0.1 K[12], the linear dependence should be satisfied down to this temperature. The observed deviation below 0.25 K in Fig. 6 is then attributed to the fact that the sample temperature increases due to the Kapitza resistance between the sample and the cavity wall. By extrapolating the linear relation above 0.25 K to lower temperatures, we can estimate the sample temperatures T_s from Fig. 6. The obtained T_s are plotted against the cavity temperature T_c in Fig. 7. The solid line (1) corresponds to the negligible microwave power. The other lines (2) and (3) are calculated for the absorbed microwave power of 0.02 and 0.1 μW, respectively with R_K of CrK-alum. The open circles show the experimental results. As is seen from Fig. 7, the practical heat inflow in our experiment is about 0.6 erg/sec. In ESR measurements for various substances below 1 K, the present method seems to be effective for the determination of the sample temperature.

§ 4 Concluding Remarks

Our combined ^{3}He-demagnetization system was proved to be practically useful for the ESR work in a frequency range of 24 ∿ 47 GHz at temperatures from 4.2 K to about 100 mK, and satisfactorily be applied to the ESR study in the low-dimensional magnets with T_N below 1 K, such as $Cu(NH_3)_4SO_4 \cdot H_2O$[19], $Rb_2PbCu(NO_2)_6$[20] and $CuSO_4 \cdot 5H_2O$[21].

Now it may be necesarry to do a comparative discussion about the merits and demerits of various ESR techniques below 1 K. The simplest way to realize ESR below 1 K is to use ^{3}He cryostat or to use a demagnetization cryostat. The former is limited down to about 0.4 K but a precise temperature setting is available. The latter is effective down to 0.1 ∿ 0.07 K but the temperature control above 0.5 K is very difficult. Our cryostat was designed to cover both merits and the results were satisfactory. However, one of the demerits in our system is the complexity because one must make two stages for refrigeration.

The next problem to be considered is the ESR sensitivity as a whole. As is well known the higher sensitivity can be expected if higher input microwave power is used. However, the high power increases the sample temperature. Our conclusion is summarized as follows : if one uses usual detecting systems such as the crystal video system, i.e., the crystal diode detection using the frequency or amplitude modulation, the microwave power level of the order of microwatt is necessary for the standard ESR measurements. In this case, the lowest temperature of the sample may be about 50 mK even if one uses the optimum experimental condition.

Therefore, the use of the more sensitive detectors such as the superheterodyne detector or the SQUID detector may be necessary when one wishes to do ESR study in more low temperature region, i.e., around 10 mK or in the millikelvin temperature region.

B Magnetization Measurement by Fluxgate Magnetometer below 1 K

§ 1 Introduction

Since the re-entrant superconductivity was discovered in the ternary compounds $(RE)Rh_4B_4$ by Fertig et al.[22] and in the ternary Chevrel-phase compounds $(RE)_xMo_6S_8$ and $(RE)_xMo_6Se_8$ by Ishikawa et al.[23], where (RE) means a rare earth element and $x = 1.0 \sim 1.2$, there have been extensive studies about superconductivity and magnetic order in these compounds. One of the surprising features of these compounds is the coexistence of the magnetic order and the superconductivity. In the case of $RE_{1.2}Mo_6S_8$ for RE = Tb, Dy and Gd, the coexistence of the superconductivity and antiferromagnetic order have been confirmed by neutron scattering experiments[24),25),26)]. In the case of ferromagnets such as $ErRh_4B_4$, however, the nature of the magnetic order coexisting with superconductivity is still controversial. Although the theoretical approachs by several authors[27)-30)] have predicted the coexistence of superconductivity and the helical spin ordering in a narrow temperature region just above the ferromagnetic ordering temperature, $T_{c2} \simeq 0.8$ K in $ErRh_4B_4$, there have been found no experimental evidence for the helical spin phase except for the suggestive neutron scattering data[31),32)]. To check the possibility of the presence of the helical spin ordering, it is desired to investigate the magnetization profile around T_{c2} in $ErRh_4B_4$.

For the measurements of weak magnetization below 1 K, SQUID (Superconducting QUantum Interference Devices) is usually used.

In the present case where the magnetization is large, however, this method is not adequate because of its too sensitive detecting abilities. For the present magnetization measurements in ^{3}He temperature region, the usual Faraday method is also not suitable because it is difficult to operate in such a low temperature region below 1 K. The magnetization curve can also be obtained by observing the induction signal of a pick up coil with scanning the magnetic field. However, the sensitivity of this method is not so high. In order to get higher sensitivity, the scanning speed must be increased. It is, however, undesirable for the present measurements because of the heating due to the eddy current loss. Considering these facts, we adopted the fluxgate magnetometer method[33),34)] using a superconducting transformer. This fluxgate magnetometer was set up by making use of Hewlet Packerd clip-on dc milliammeter (H.P. 428B) with an accessory (H.P. 3529A) for weak magnetic field measurement. This type of magnetometer, which was initially applied to the nuclear magnetization measurements in the millikelvin temperature region by Andres et al.[33),34)] is easy to handle compared with SQUID and has enough sensitivity for present measurement.

In this method, however, it is difficult to scan the magnetic field because the perfect balance of the superconducting transformer under the field scan is difficult. Therefore, the magnetization measurement can only be done by changing the temperature or by extracting and inserting the sample from the superconducting transformer. In the following section, the principle and construction of the fluxgate magnetometer will be shown in detail.

The techniques of the practical operations and the estimation of the sensitivityare shown in §3. Applications to the magnetization measurement will be described in Part (III).

§ 2 Cryostat

^{3}He refrigerator was used for magnetization measurement below 1 K. Two kinds of cryostat were constructed. One of them is the cryostat for the extracting method by which one can measure the magnetization process at a constant temperature. In another one, the sample is fixed and the magnetization change can be measured by changing temperature.

(1) The Cryostat and The Fluxgate Magnetometer

Outline of the magnetization measurements by the fluxgate magnetometer is shown in Fig. 8. The superconducting transformer consists of the astatic pick up coil (sample coil and compensation coil), the probe coil and the connecting leads. All wires are made of NbTi alloys. The astatic pick up coil is located in the vacuum can so as to set the sample just in the center of the sample coil. On the other hand, the field probe is inserted in the probe coil which is covered by the NbTi shield. The transformer system is directly immersed in liquid ^{4}He.

The principle of the fluxgate magnetometer is as follows. When the magnetization of the sample in the sample coil changes due to the temperature change under the constant magnetic field, for example, the supercurrent induced in the sample coil transforms to the probe coil so as to keep the total flux in whole of

the transformer to be constant. This supercurrent produces the magnetic field in the probe coil which is proportional to the change of the flux in the sample coil. The produced field is detected by the field probe with aid of the clip-on dc milliammeter.

As the fluxgate magnetometer probe can detect the magnetic field in the range from 1 mGauss to 10 Gauss corresponding to the meter ranges from 1 mA to 10 A of the clip-on dc milliammeter, the effective measuring range of the magnetization covers from 10^{-3} Gauss to about 10^{3} Gauss by adjusting the sample volume. This means that one can measure the magnetization of weak paramagnets as well as usual ferromagnets. The magnetic field is supplied by the superconducting magnet in the persistent current mode, and its maximum field is about 30 kOe. A desired temperature is obtained by ^{3}He refrigerator and it is measured by a commercial germanium resistance thermometer using IT (Instruments for Technology Ltd.) automatic resistance bridge.

Two types of the sample holding system are designed and used. The model I in Fig. 9 is used for measuring the temperature dependence of the magnetization and the magnetization at a temperature is measured by extracting the sample using the model II system in Fig. 9. In the model II system, the sample position is fixed during the experiment while it is moved by the dc motor for extraction and insertion of the sample from the sample coil of the model II. The sample speed for extraction and insertion is about 4 cm/min. with the total stroke of about 6 cm. The sample and germanium thermometer in the model I are thermally

linked with the ^{3}He pot by about 200 polyurethane coated copper wires of 0.05 mm in diameter which are tightly connected to the sample by Apiezon N grease. The sample in the type II system is immersed directly into liquid ^{3}He. In the both models, liquid ^{3}He of about 2 cm^3 is used. The temperature of the sample is controlled by controlling the vapor pressure of liquid ^{3}He below 1.2 K and by controlling the vapor pressure of liquid ^{4}He between 4.2 K and 1.2 K.

(2) Design of The Transformer Coil

In this section, the optimum design for the superconducting transformer is considered. The total flux ϕ_T of the transformer coil, i.e., both the pick up and probe coils are constant and quantized. Therefore, the relation,

$$\phi_T = i(L_1 + L_2 + L_3) = n\phi_0, \qquad \text{(Gauss)} \qquad (1)$$

is obtained where i is the supercurrent flow in the closed circuit. L_1, L_2 and L_3 are self-inductances of the pick up and probe coils and interconnecting NbTi leads as shown in Fig. 10. ϕ_0 is the flux quantum (2.067×10^{-7} Gauss·cm^2) and n is an integer.

When the flux in the sample coil changes by $\Delta\phi$ due to the change of the magnetization of the sample, the supercurrent must be modified by Δi so as to keep ϕ_T to be constant. Therefore, the relation,

$$\Delta\phi + \Delta i(L_1 + L_2 + L_3) = 0, \tag{2}$$

holds. Δi is then obtained as

$$\Delta i = -\Delta\phi/(L_1 + L_2 + L_3). \quad \text{(emu.A)} \tag{3}$$

This current change induces the magnetic field change ΔH in the long probe coil given by

$$\Delta H \simeq 4\pi\left(\frac{n_2}{l_2}\right)\Delta i = -\left(\frac{4\pi n_2/l_2}{L_1+L_2+L_3}\right)\Delta\phi, \quad \text{(Oe)} \tag{4}$$

where l_2 and n_2 are the length and turn number of the probe coil.

Now, we consider the case where the sample length is much longer than the coil length as is shown in Fig.11. The flux $\Delta\phi$ due to the induced magnetization ΔM is given by

$$\Delta\phi \simeq 4\pi n_1 A\Delta M = \pi^2 n_1 d^2 \Delta M, \quad \text{(Gauss}\cdot\text{cm}^2\text{)} \tag{5}$$

where A is the cross section of the sample in cm^2, d is the diameter of the cylindrical sample and n_1 is the turn number of the sample coil. Thus, the induced magnetic field ΔH in the probe coil is obtained by using eqs. (4) and (5) as

$$\Delta H = -p\Delta M, \quad \text{(Oe)} \tag{6}$$

with

$$p = \frac{4\pi^3 n_1 n_2 d^2}{l_2(L_1+L_2+L_3)}. \tag{7}$$

To keep a high sensitivity of the transformer system, it is necessary to have a large $\Delta H/\Delta M$ value. Therefore, the p-value in eq. (7) should be large. As d and l_2 are substantially limited by the effective volume of the cryostat, the practical variable parameters are n_1, n_2, L_1 and L_2. L_3 is much smaller than L_1 and L_2 so that it is neglected. Thus, p is approximately written by

$$p \simeq \left(\frac{4\pi^3 d^2}{l_2}\right) \times \frac{n_1 n_2}{L_1+L_2}. \tag{8}$$

Noticing the relations $L_1 \propto n_1^2$ and $L_2 \propto n_2^2$, it is simply verified that the maximum p-value is obtained when the relation

$$L_1 = L_2, \tag{9}$$

is satisfied. This is one of the important relations for designing the transformer system.

The sample and compensation coils are astatically wound. The inductances are nearly equal to each other with 12 turns and 1.2 cm in diameter. For the probe coil, the diameter of 0.7 cm, 62 turns and 2.5 cm in length are adopted.

The self-inductances of L_1 and L_2 are numerically evaluated by a standard formula and obtained 6.82 μH and 6.65 μH, respectively. L_3 is also estimated and it was found to be about 0.15 μH.

Using these estimations of L_1, L_2 and L_3, the magnetic field ΔH induced in the probe coil is estimated as

$$\Delta H = -\boxed{0.872} \cdot \pi d^2 \Delta M. \quad \text{(Oe)} \qquad (10)$$

(3) Detailed Construction of The Transformer System

The field probe (H.P. 3529A) is the magnetic field sensor for detecting the magnetic field in the probe coil. Its plastic cover is stripped off. The field probe is drived by 20 kHz signal and the leakage flux becomes a serious noise for the transformer system. In order to shield the transformer system from 20 kHz rf field, the field probe is covered by the copper rf shield of 6 mm I.D., 7 mm O.D. and 35 mm in length as shown in Fig.12. The probe system is located inside the NbTi shield case in liquid ^{4}He bath.

The probe coil is wound around the copper tube. The bias coil for adjusting the detector level of the clip-on dc milli-ammeter is also wound on the probe coil. The bias adjustment can easily be done by feeding an additional dc current to the bias coil from an external current source of Keithley model 225.

The pick up coil was astatically wound around the Bakelite bobbin and it was tightly set in the vacuum can as shown in Fig. 12. All connections of the transformer are connected with spot welding.

A heater wire of about 100 Ω is wound around a part of the NbTi leads. It is used to destroy a residual supercurrent trapped in the transformer and to establish the scale of the clip-on dc

milliammeter to zero before measurements.

The transformer is made of 0.070 mm in core diameter copper coated (0.100 mm in diameter) formval insulated (0.144 mm in diameter) NbTi wire manufactured by Vacuum Metallugical Co. Ltd.

As shown in Fig.12, the superconducting magnet is attached to the vacuum can with the fine adjustment system so as to set the magnet just in the center of the pick up coil.

The main part of the vacuum can is made of 24 mm I.D. and 25 mm O.D. stainless steel tube except the sample part. The central part of the can is made of copper in order to avoid the spurious magnetic effect to pick up coil system. The system given in Fig.12 is used both for the model I and II in common.

§ 3 Operation of The Cryostat

(1) Model I cryostat

The temperature dependence of the magnetization can be observed as follows. After transferring liquid ^{4}He in the Dewar, a desired static magnetic field is supplied by the superconducting magnet in the persistent current mode with breaking the transformer circuit by the heater. Next, the detector level of the clip-on dc milliammeter is adjusted by the bias current so as to cover the desired range of the sample magnetization. The temperature dependence of the magnetization can be measured with decreasing temperature. A desired temperature between 4.2 K and 1.2 K can be obtained by pumping out ^{4}He gas by 3000 litters/min. Kenny type pump. Around 1.2 K, ^{3}He gas is liquified. The exchange gas

is evacuated to about 10^{-6} Torr. by diffusion pump and a required temperature down to ~0.5 K can be obtained by pumping out ^{3}He gas. The temperature dependence of the magnetization is observed and recorded by looking at the change of the detector level of the clip-on dc milliammeter.

(2) Model II cryostat

The magnetization measurement by the model II cryostat can be done in the following procedure. After obtaining a desired temperature by the similar method given in the previous subsection, the required field is supplied by a superconducting magnet with breaking the transformer circuit. The transformer circuit is operated after getting a desired constant field and the detector level of the clip-on dc milliammeter is adjusted as before. The sample is inserted into the pick up coil by driving the dc motor and the magnetization is measured. After the temperature measurement by the germanium thermometer, the sample is extracted and the magnetization is measured again. The difference between the maximum and the minimum values of the detector level should be proportional to the magnetization of the sample. Repeating this insertion and extraction in the various fixed magnetic field under the coustant temperature, the magnetization curve can be obtained between 0.5 K and 4.2 K.

§ 4 Characteristics of The Cryostats

The experimental test of the present cryostats for magnetization measurements was done by using a typical paramagnetic CMN sample. There are two important parts for obtaining high sensitivity of the magnetization measurements. One of them is the noise level of the transformer signal corresponding to the field fluctuation in the probe coil and the other is the long time drift in the coil. A typical experimental datum without sample is shown in Fig. 13. It shows an output of the fluxgate magnetometer showing the field fluctuation level in the probe coil. The result shows that both the fluctuation and drift are within 1.2×10^{-4} mA of the magnetometer which corresponds to the sensitivity of the magnetization change ΔM in the sample coil as $\Delta M \simeq 7 \times 10^{-5}$ Gauss. This may be enough for usual magnetization measurements except the nuclear paramagnetism.

It is difficult to determine the absolute value of the magmetization change by using the present equipment. Therefore, it is usually calibrated by the Faraday method in higher temperature region.

Typical magnetization data of CMN are shown in Fig. 14. The CMN powder is mixed with Apiezon N grease and is holded with a cylindrical shape of 3 mm in diameter. The output current (A) which is proportional to the susceptibility is proportional to 1/T, therefore, the accuracy of the equipment is garanteed.

An example of the output signal of the magnetometer due to the sample motion is shown in Fig. 15. Fig. 15a shows relative positions of the sample and coil and the corresponding signal is illus-

trated in Fig. 15b. When the sample is far from the pick up coil, the signal level is zero as is shown in the position A and the level shows its maximum at B, i.e., the sample is just at the center of the sample coil. The level becomes negative around C because of the negative flux change due to the compensation coil. The level shows a similar change by extracting the sample as is easily seen in Fig. 15b. This magnetization measurement can easily be done by using the present fluxgate magnetometer.

C Thermometry below 1 K

§ 1 Introduction

There are several methods of measuring temperatures below 1 K. In the ^{3}He temperature region, i.e. 1 ∿ 0.3 K, use of the germanium thermometer is most convenient because the commercial one has enough calibrations in the above temperature range. Therefore, the germanium thermometer was used both for the model I and II systems, as was described in the previous section. The used thermometer is GR-200A-100 calibrated by Lake Shore Cryotronics. Below 0.3 K, however, the thermometer has no reliable calibration. So, we must use other thermometers, especially for the ESR study around 0.1 K. Generally speaking, the magnetic susceptibility thermometer using typical paramagnets such as CMN may be the most reliable one around 0.1 K. However, it is not so convenient because the field sensor, i.e. the Hartshorn coil and the sample, is not so small. Moreover, it is sensitive for the magnetic field near by. Considering these facts, a carbon resistor was used for the ESR study and the CMN thermometer was used for the calibration of the carbon thermometer. The practical design and operation of the CMN thermometer is described in the next section and the calibration of the carbon resistor is shown in §2.

§ 2 ac Susceptibility Measurement by Hartshorn Mutual Inductance Bridge and Calibration of The Carbon Resistor

The ac Hartshorn mutual inductance bridge has been constructed in our laboratory in order to measure the ac susceptibility of CMN for the calibration of the carbon resistor below 1 K.

A block diagram of the bridge is shown in Fig.16. A low frequency of about 100 ∿ 200 Hz oscillating field of about 1 Oe is supplied into the primary coil A. PAR 124A lock-in amplifire is used as a detector in high sensitive ac voltmeter mode. Two mutual inductors M_1 and M_2 are used for the bridge balance. M_1 is the type 4229 calibrated variable mutual inductor of H. Tinsley Co. Ltd. and M_2 is the Brooks type variable mutual inductor of YEW (Yokogawa Electric Works).

Cut view of the cryostat for the ac susceptibility measurements is shown in Fig.17. ^{3}He and adiavatic demagnetization stage are similar to those of ESR measurements described in A in Part I. ^{3}He gas is condensed in ^{3}He pot C through the evacuation pipe A. About 40 grams of Fe ammonium alum is packed in the pill F with Apiezon J oil and about 1000, polyurethane insulated copper wires of 0.05 mm in diameter. The salt pill F is suspended by the teflon supporter E from the bottom of ^{3}He pot C. The manganin heater P of about 100 Ω is also immersed in the pill in order to control the temperature. The sample M, the germanium thermometer I and the carbon resistor H are immersed in the thermal link O made of about 300 polyurethane insulated copper wires of 0.05 mm in diameter. The coil set N (primary coil K and secondary coil L) for the susceptibility measurements is attached

to the bottom of the adiavatic vacuum can B. The vacuum cell J for the coil set was made of STYCAST 2850-GT by Emerson & Cuming Japan K.K.. D is lead wires for the coils and thermometers. G is the superconducting magnet for the adiavatic demagnetization.

Operations of this cryostat is similar to that of ESR one.

(1) Coil Design and Construction

There have been many studies[35), 36)] for the precise temperature measurement below 1 K using ac Hartshorn mutual inductance method. The present coils were also designed according to their results and its geometrical constructions are shown in Fig.18.

For the geometry in Fig.18, the mutual inductance L_M due to the sample of CMN is given by [35)]

$$L_M = 16 \cdot \pi^2 n_s n_p V \chi f_s f_p \quad (\times 10^{-9}), \quad (H) \qquad (1)$$

for a spherical sample where f_s and f_p are geometrical factors as

$$f_s = \frac{1}{(b_s^2+\tilde{l}^2)^{1/2}} + \frac{1}{2}\frac{d_1+\tilde{l}}{[b_s^2+(d_1+\tilde{l})^2]^{1/2}} - \frac{1}{2}\frac{d_1+3\tilde{l}}{[b_s^2+(d_1+3\tilde{l})^2]^{1/2}} \qquad (2)$$

and

$$f_p = \frac{1}{2}\left\{\frac{d_2+\tilde{l}}{[b_p^2+(d_2+\tilde{l})^2]^{1/2}} + \frac{d_1+d_2+3\tilde{l}}{[b_p^2+(d_1+d_2+3\tilde{l})^2]^{1/2}}\right\} \qquad (3)$$

In eq. (1), n_p and n_s are the number of turns per unit length on the primary and secondary windings, V is the volume of CMN, χ is its susceptibility and b_s and b_p are effective radii for the secondary and primary coils. The dimensions of the present coil such as $\tilde{l}$, d_1 and d_2 are shown in Fig.18. From these parameters, f_p and f_s are given to be 0.820 and 0.879. n_p and n_s are determined as 1683 turns/cm and 2041 turns/cm, respectively.

(2) Sensitivity and Calibration of The Carbon Resistor

The sensitivity of the present coil was calibrated by measuring the powdered susceptibility of about 1 gram CMN between 4.2 K and 1.2 K. As already described in (1) in this section, the parameters n_p, n_s, f_p and f_s are known. Then eq. (1) is written by

$$L_M = 0.391 \times \chi V. \quad \text{(H)} \qquad (4)$$

In the present system, the minimum detectable change of the mutual inductance $\Delta L_{M\ min.}$ under the usual condition was obtained as

$$\Delta L_{M\ min.} \simeq 3.3 \times 10^{-2}. \quad (\mu H) \qquad (5)$$

Then, the minimum detectable change of the susceptibility $\Delta\chi_{min.}$ per unit volume for the present system was determined as

$$\Delta\chi_{min.} \simeq 8.4 \times 10^{-8}. \quad \text{(emu)} \qquad (6)$$

This sensitivity is enough for the calibration of the carbon resistor below 4.2 K using CMN of about 1 gram. The accuracy of the temperature determination is about 0.1 % below 4.2 K.

In our ESR measurements, a commercial Matsushita carbon resistor ERC-GJ, 1/8 W, 100 Ω resistor was used as a thermometer down to 100 mK. A famous carbon resistor made by Speer is also effective but the size of Matsushita carbon resistor is smaller than that of the Speer. So, we used the former one.

The calibration of the carbon resistor was done by simultaneously measuring the ac susceptivility of CMN and the resistance of the carbon resistor using the already mentioned cryostat as shown in Fig.17. The resistance was measured by the automatic resistance bridge of IT (Instruments for Technology Ltd). It can measure the resistance within 10^{-11} W power dissipation with about 0.5 % precision even below 0.1 K.

The temperatures of the ESR measurements done in the present study was calibrated using Fig.19. The field dependence of the resistor is expected to be within a few percents up to 30 kOe. For the aging effect of the resistor, the similar CMN calibration was done after one week and tried again after about one year. The drift was found to be a few percents.

References

1). K. Okuda, H. Hata and M. Date : J. Phys. Soc. Jpn. 33 (1972) 1574.

2). K. Oshima, K. Okuda and M. Date ; J. Phys. Soc. Jpn. 41 (1976) 475.

3). K. Oshima, K. Okuda and M. Date : J. Phys. Soc. Jpn. 44 (1978) 757.

4). K. Okuda, K. Oshima and M. Date ; J. Phys. Soc. Jpn. 44 (1978) 801.

5). K. Okuda and K. Kadowaki : J. Phys. Soc. Jpn. 46 (1979) 45.

6). R. H. Ruby, H. Benoit and C. D. Jeffries : Phys. Rev. 127 (1962) 51.

7). I. Svare and G. Seidel : Phys. Rev. 134 (1964) A172.

8). J. A. Cowen, R. D. Spence, H. Van Till and H. Weinstock : Rev. Sci. Instrum. 35 (1964) 914.

9). N. C. Ford, Jr and C. D. Jeffries : Phys. Rev. 141 (1966) 381.

10). T. L. Bohan and H. J. Stapleton : Rev. Sci. Instrum. 39 (1968) 1707.

11). D. D. Thornton : Phys. Rev. B1 (1970) 3193.

12). H. Abe and K. Koga : Jpn. J. Appl. Phys. 13 (1974) 1145.

13). J. I. Conolly, W. R. Roach and R. J. Sarwinski : Rev. Sci. Instrum. 36 (1965) 1370.

14). O. E. Vilches and J. C. Wheatley : Rev. Sci. Instrum. 37 (1966) 891.

15). D. T. Teaney and M. J. Freider : Phys. Rev. Lett. 9 (1962) 212.

16). P. H. Cole and W. J. Ince : Phys. Rev. 150 (1966) 377.

17). A. J. Heeger, A. M. Portis, D. T. Teaney and G. L. Witt ; Phys. Rev. Lett. 7 (1961) 307.

18). H. Abe and K. Koga : J. Phys. Soc. Jpn. 38 (1975) 99.

19). to be published in J. Phys. Soc. Jpn.

20). to be published in J. Phys. Soc. Jpn.

21). K. Okuda and K. Kadowaki ; to be published in J. Phys. Soc. Jpn.

22). W. A. Fertig, D. C. Johnston, L. E. DeLong, R. W. McCallum, M. B. Maple and B. T. Matthias : Phys. Rev. Lett. 38 (1977) 987.

23). M. Ishikawa and Ø. Fischer : Solid State Commun. 23 (1977) 37.

24). D. E. Moncton, G. Shirane, W. Thomlinson, M. Ishikawa and Ø. Fischer : Phys. Rev. Lett. 41 (1978) 1133.

25). W. Thomlinson, G. Shirane, D. E. Moncton, M. Ishikawa and Ø. Fischer : J. Appl. Phys. 50 (1979) 1981.

26). C. F. Majkrzak, G. Shirane, W. Thomlinson, M. Ishikawa, Ø. Fischer and D. E. Moncton : Solid State Commun. 31 (1979) 773.

27). H. Matsumoto, H. Umezawa and M. Tachiki : Solid State Commun. 31 (1979) 157.

28). E. I. Blount and C. M. Varma : Phys. Rev. Lett. 42 (1979) 1079.

29). L. N. Bulaevski, A. I. Rusinov and M. Kulić : Solid State Commun. 30 (1979) 59.

30). M. V. Jarić and M. Belić : Phys. Rev. Lett. 42 (1979) 1015.

31). D. E. Moncton, D. B. McWhan, J. Eckert, G. Shirane and W. Thomlinson : Phys. Rev. Lett. 39 (1977) 1164.

32] D. E. Moncton ; J. Appl. Phys. 50 (1979) 1880.

33] K. Andres and E. Bucher ; J. Low Temp. Phys. 9 (1972) 267.

34] K. Andres and J. H. Wernick ; Rev. Sci. Instrum. 44 (1973) 1186.

35] W. R. Abel, A. C. Anderson and J. C. Wheatley : Rev. Sci. Instrum. 35 (1964) 444.

36] W. L. Pillinger, P. S. Jastram and J. G. Daunt ; Rev. Sci. Instrum. 29 (1958) 159.

Figure Caption

Fig. 1. Schematic view of the ESR cryostat. The symbols in the figure are explained in the text.

Fig. 2a. Detailed constructions of ^3He and adiavatic demagnetization stages. The symbols in the figure are explained in the text.

Fig. 2b. Schematic view of the cavity.

Fig. 3. Block diagram of the ESR spectrometer with the microwave power modulation.

Fig. 4. An example of the cavity temperature during the ESR measurements.

Fig. 5. Recorder traces for the AFMR line in $RbMnF_3$ at the cavity temperatures T_c = 4.2 K ∿ 0.14 K for the frequency ν_0 = 32.44 GHz. The vertical spike-like lines are field marks.

Fig. 6. The square of resonance field H_0^2 versus the inverse of the cavity temperature $1/T_c$, for ν_0 = 32.44 GHz and H_0 parallel to the cubic axis in $RbMnF_3$. A solid line shows the linear relation H_0^2 versus $1/T_s$.

Fig. 7. The sample temperature T_s as a function of the cavity temperature T_c. The theoretical lines (1), (2) and (3) are given in the text.

Fig. 8. Outline of the fluxgate magnetometer.

Fig. 9. Cut views of the sample holders in the models I and II systems.

Fig. 10. Schematic view of the transformer coil system.

Fig. 11. Relation of the pick up coil and sample.

Fig. 12. Detailed structure of the vacuum can and transformer system.

Fig. 13. An example of the recorder trace without the sample at the fixed field of 200 Oe.

Fig. 14. Experimental results of the magnetization measurements in CMN.

Fig. 15a. Schematic view of the sample motion.

Fig. 15b. A recorder trace of the magnetometer output under the sample motion.

Fig. 16. Block diagram of the low frequency ac susceptivility measurement system by Hartshorn mutual inductance bridge.

Fig. 17. Cut view of the low temperature cryostat for low frequency ac susceptivility measurement by Hartshorn mutual inductance bridge.

Fig. 18. Construction of Hartshorn coil. The coil length is given by mm unit.

Fig. 19. Temperature dependence of the resistance in Matsushita ERC-18GJ, 1/8 W carbon resistor.

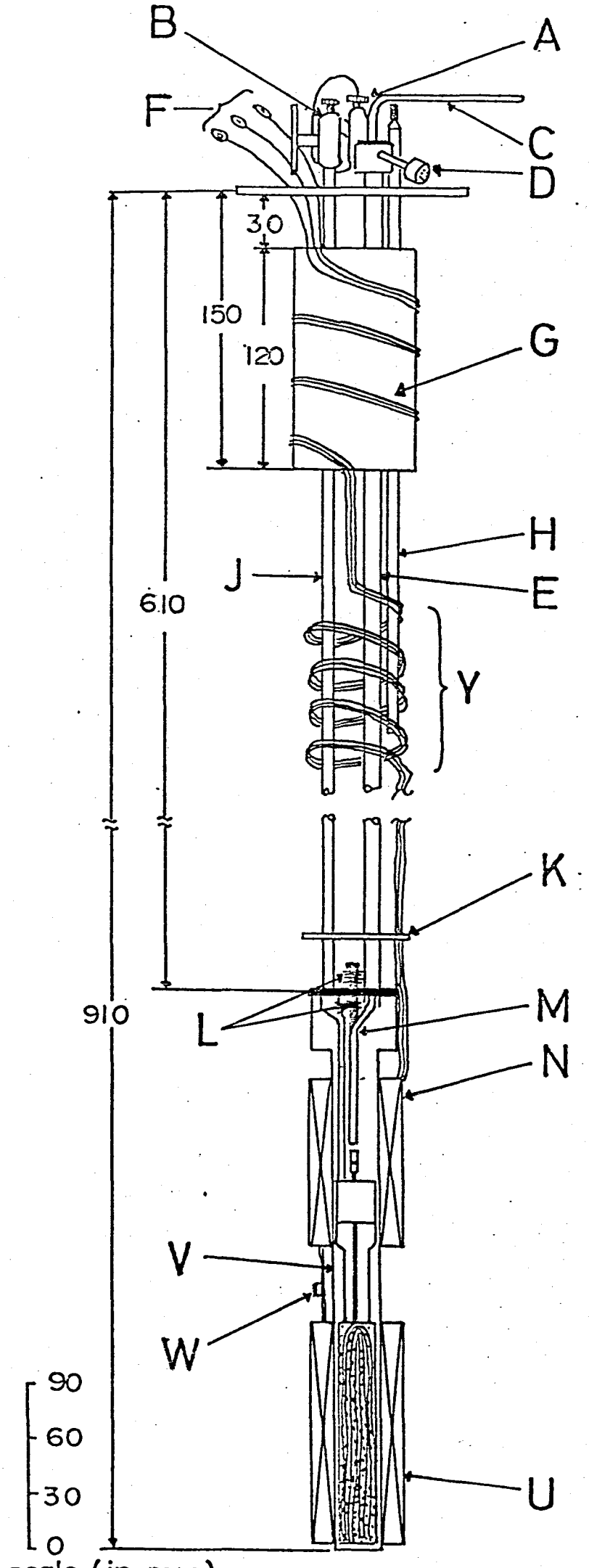

Fig. 1

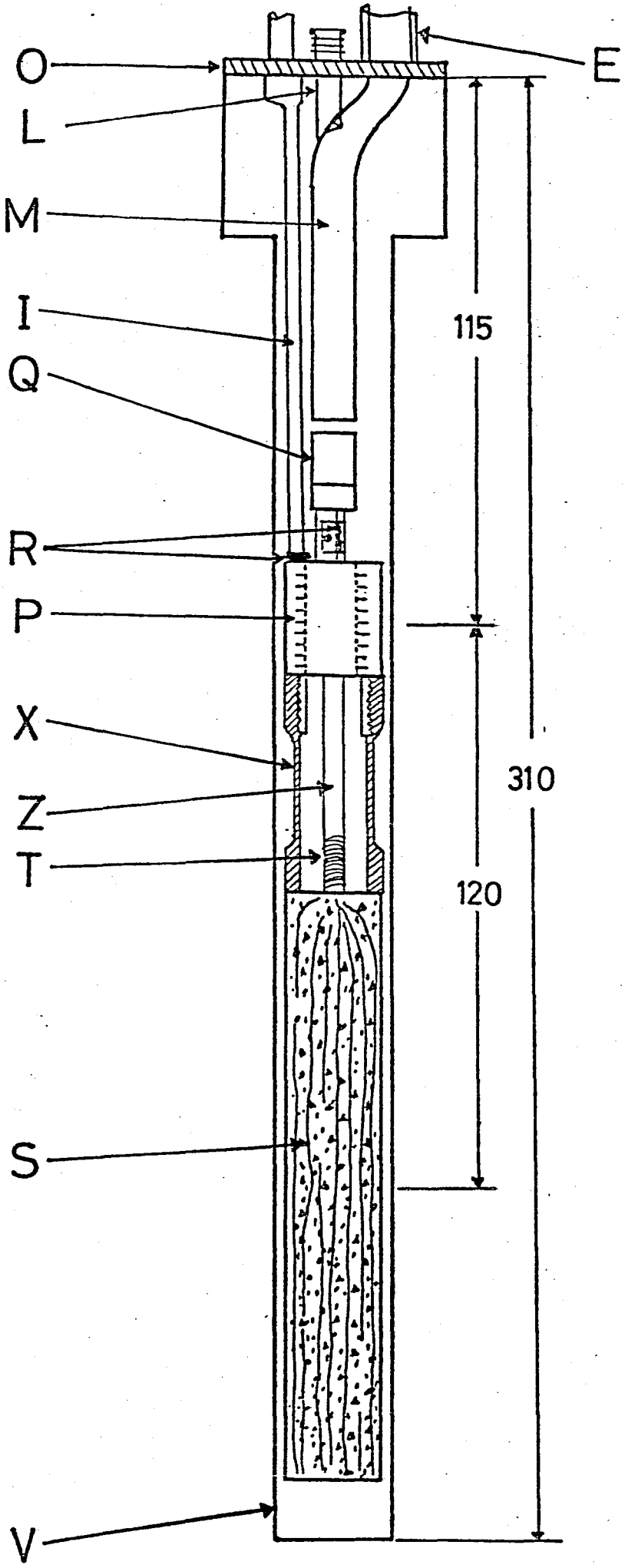

Fig. 2 a

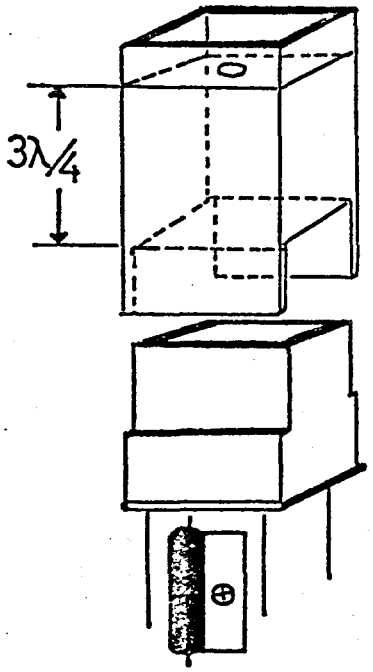

Fig. 2b

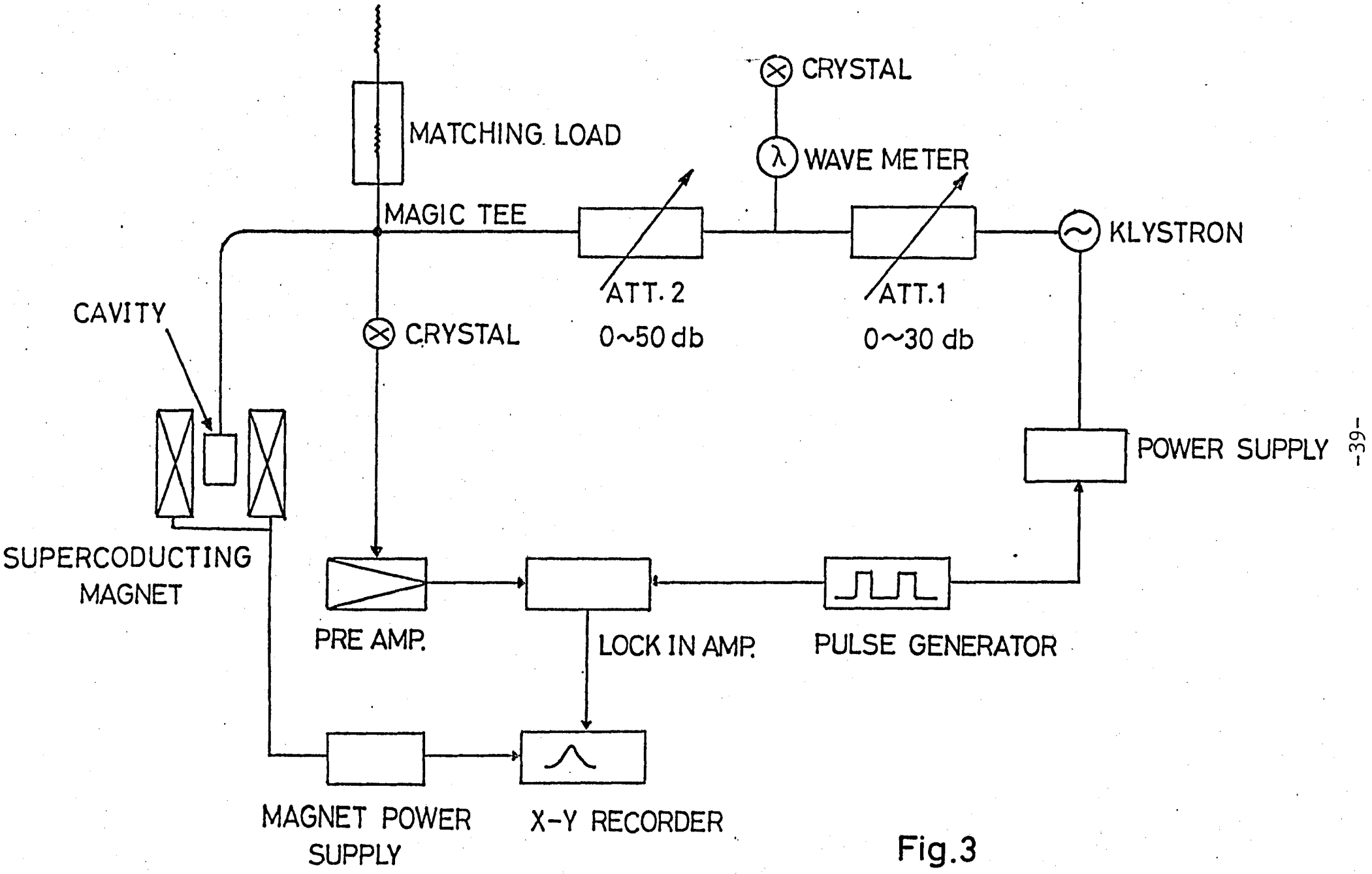
CRYSTAL
MATCHING LOAD
WAVE METER
MAGIC TEE
KLYSTRON
ATT. 2
0~50 db
ATT.1
0~30 db
CAVITY
CRYSTAL
POWER SUPPLY
SUPERCODUCTING MAGNET
PRE AMP.
LOCK IN AMP.
PULSE GENERATOR
MAGNET POWER SUPPLY
X-Y RECORDER

Fig.3

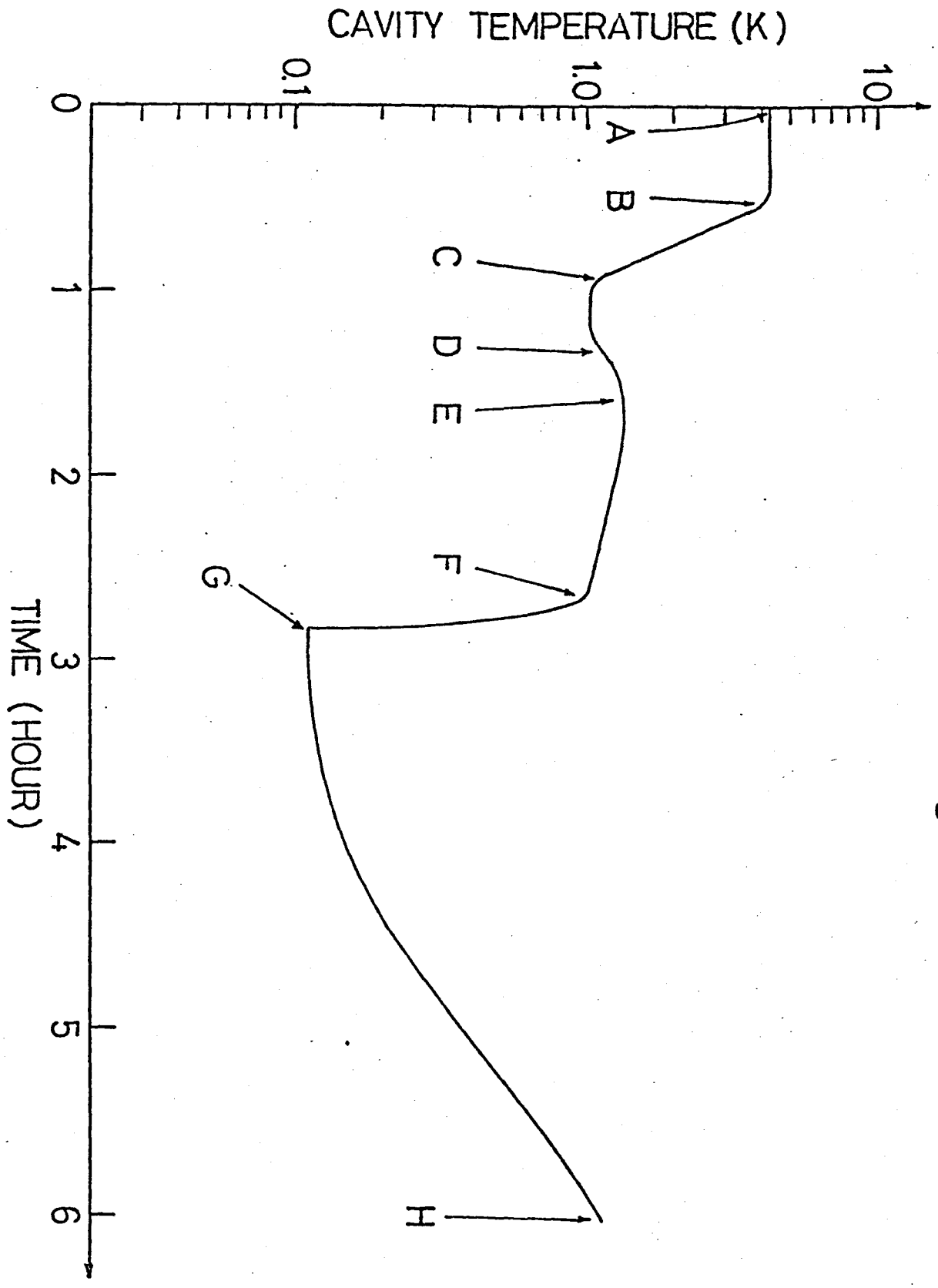

Fig. 4

Fig. 5

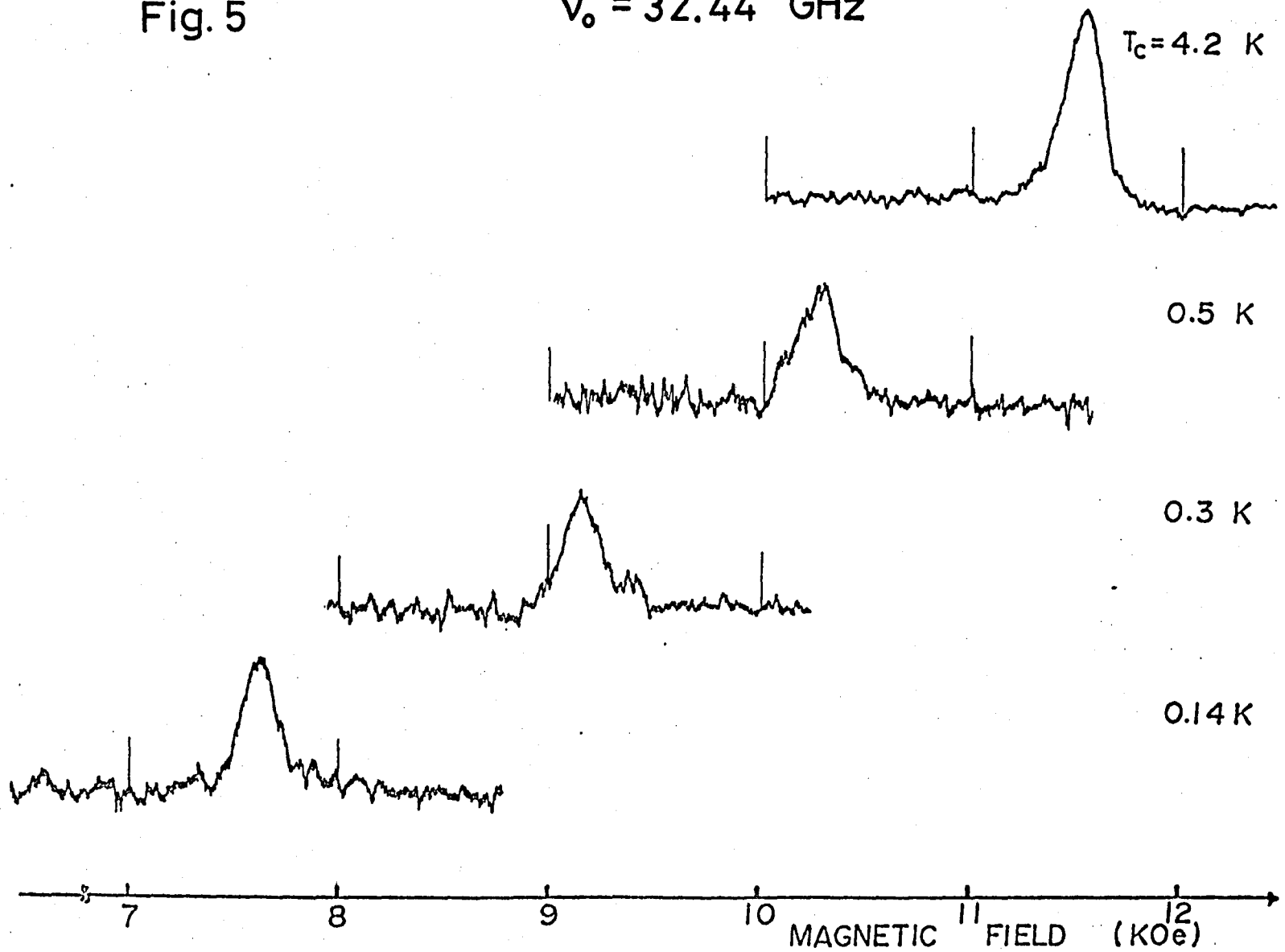
ν_o = 32.44 GHz
T_c = 4.2 K
0.5 K
0.3 K
0.14 K
7
8
9
10
11
12
MAGNETIC FIELD (KOe)

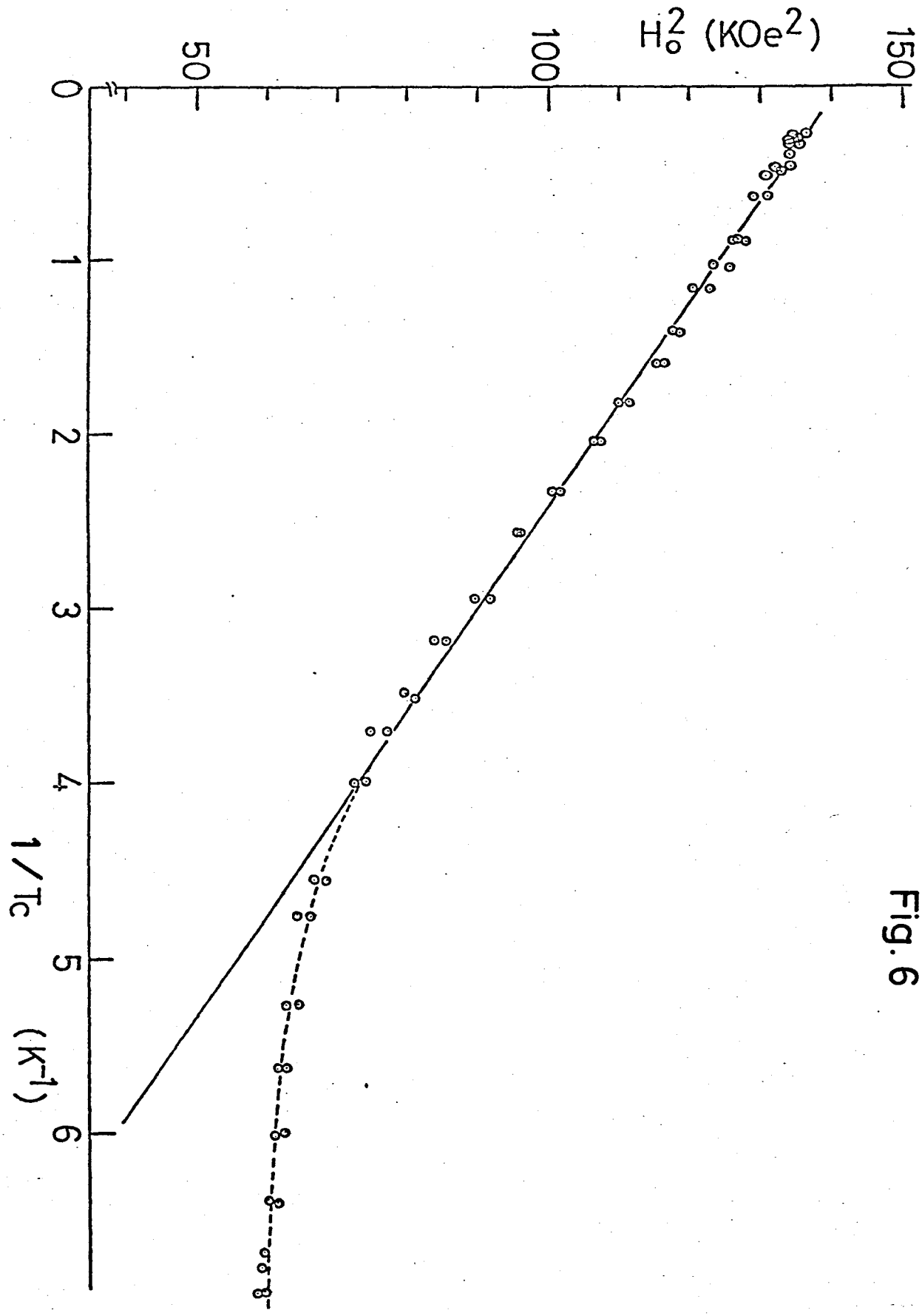

Fig. 6

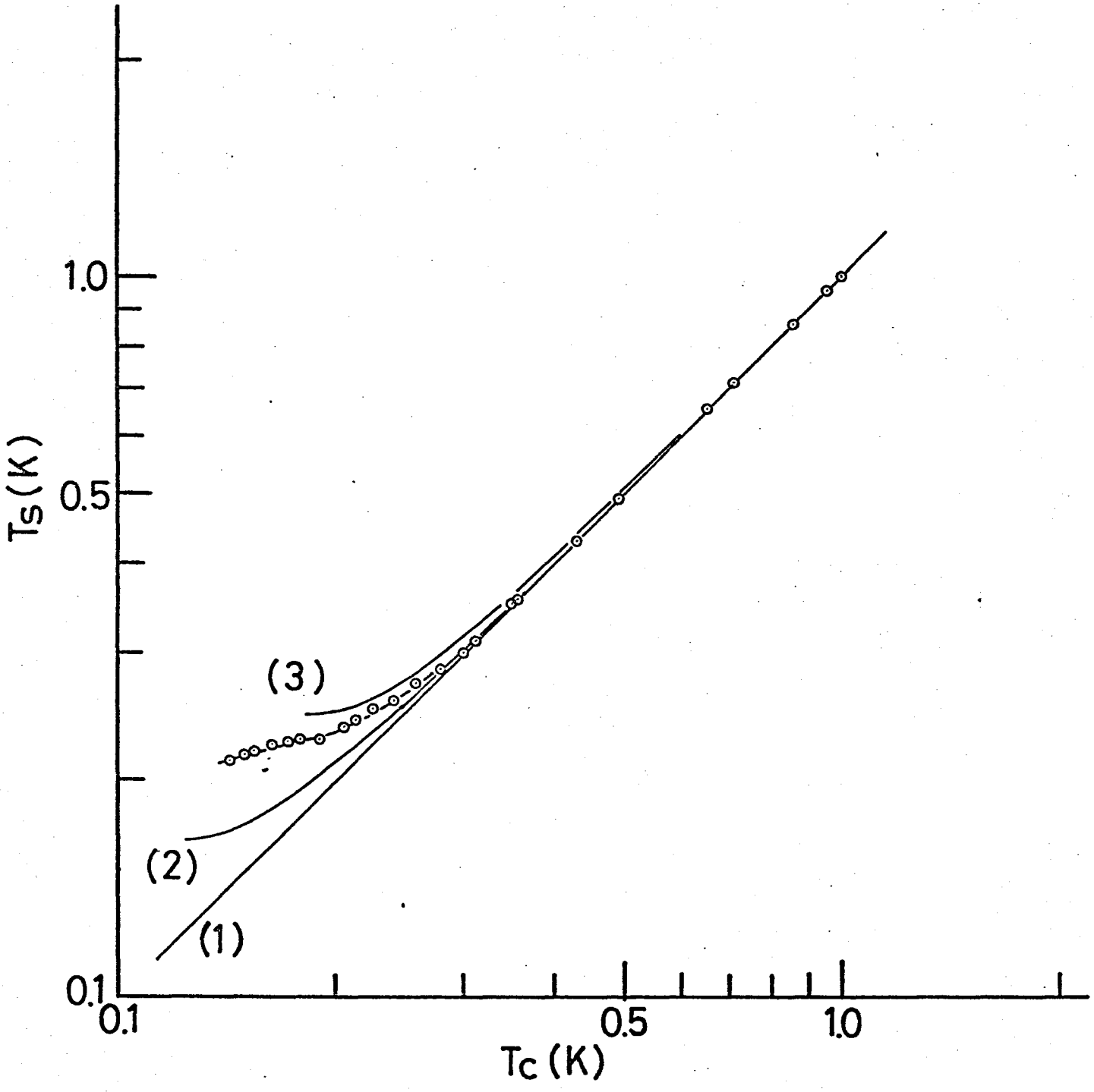

Fig. 7

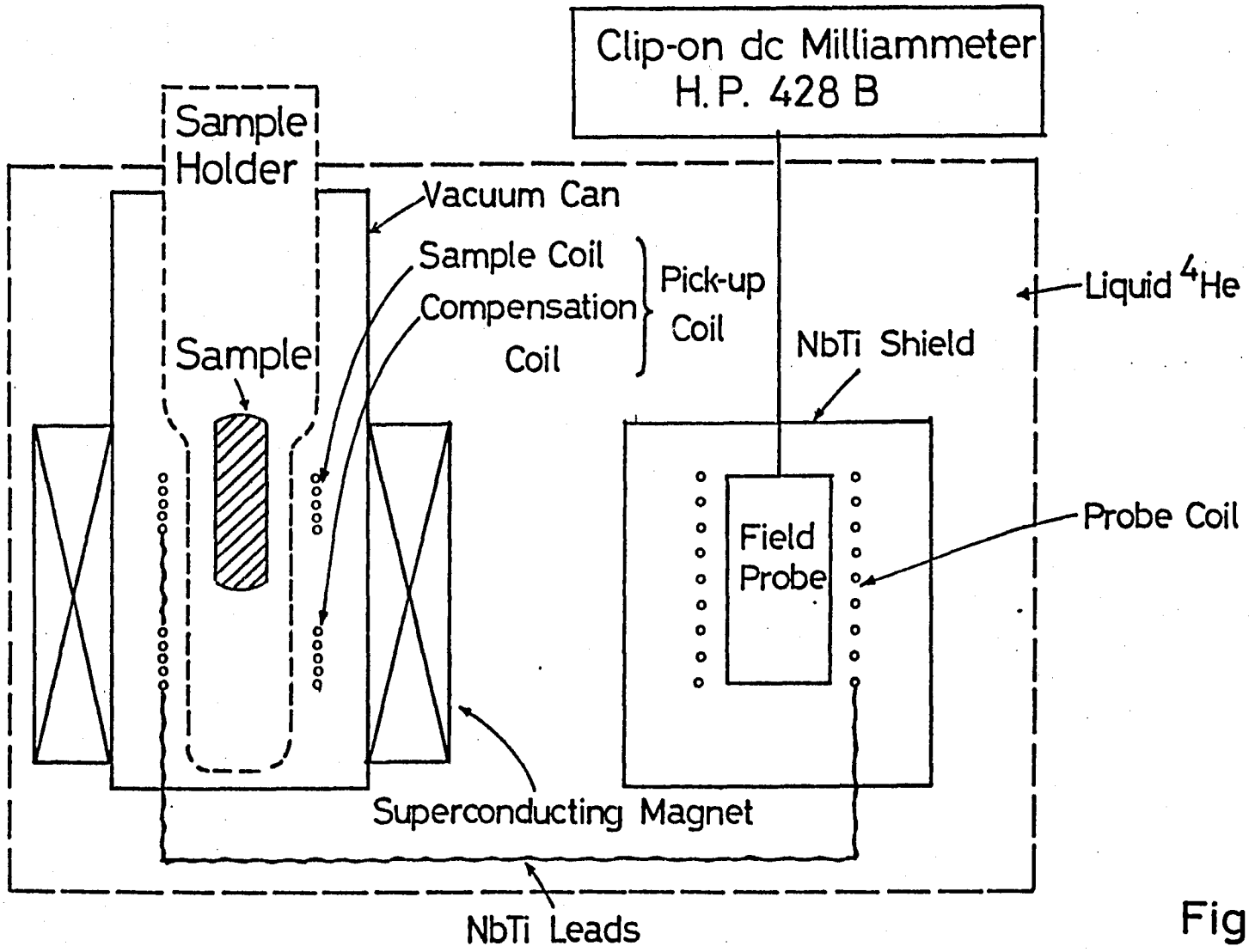
Clip-on dc Milliammeter
H.P. 428 B
Sample
Holder
Vacuum Can
Sample Coil
Compensation
Coil
Pick-up
Coil
Liquid ^{4}He
Sample
NbTi Shield
Field
Probe
Probe Coil
Superconducting Magnet
NbTi Leads

Fig. 8

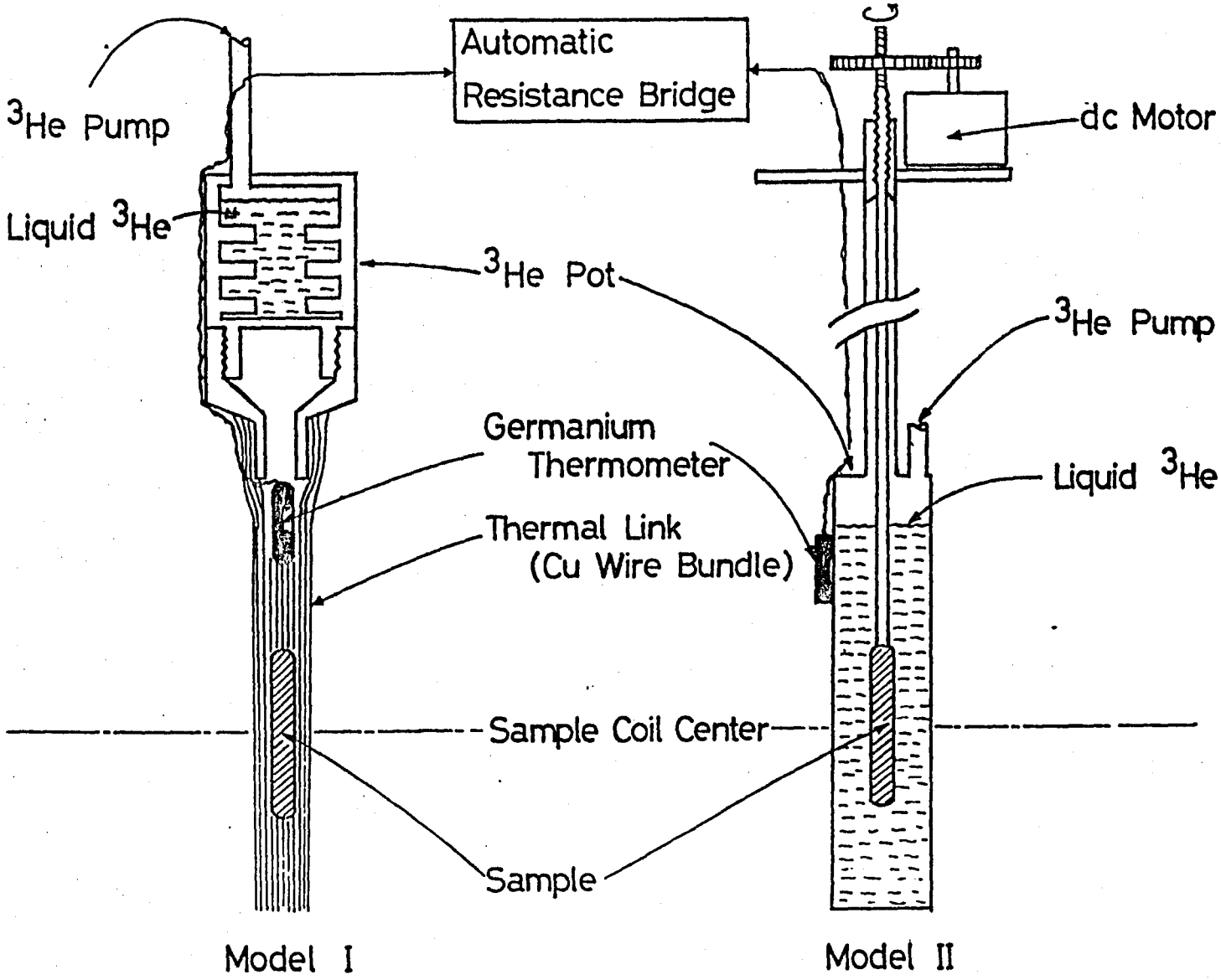
Automatic
Resistance Bridge
^{3}He Pump
dc Motor
Liquid ^{3}He
^{3}He Pot
^{3}He Pump
Germanium
Thermometer
Liquid ^{3}He
Thermal Link
(Cu Wire Bundle)
Sample Coil Center
Sample
Model I
Model II

Fig. 9

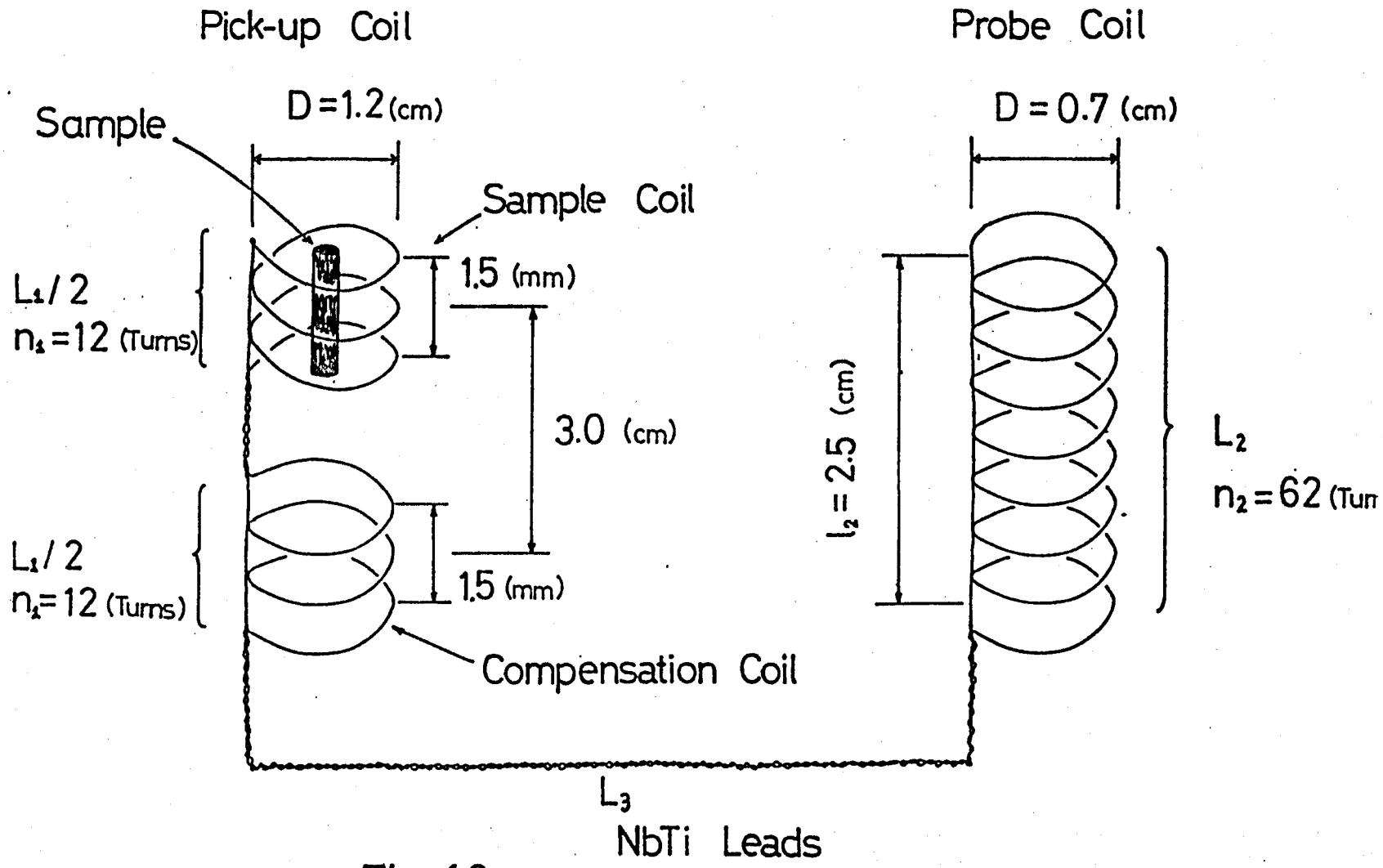
Pick-up Coil
Probe Coil
Sample
D=1.2(cm)
D=0.7 (cm)
Sample Coil
1.5 (mm)
L₁/2
n₁=12 (Turns)
3.0 (cm)
L₁/2
n₁=12 (Turns)
1.5 (mm)
Compensation Coil
l₂=2.5 (cm)
L₂
n₂=62 (Tur
L₃
NbTi Leads

Fig.10

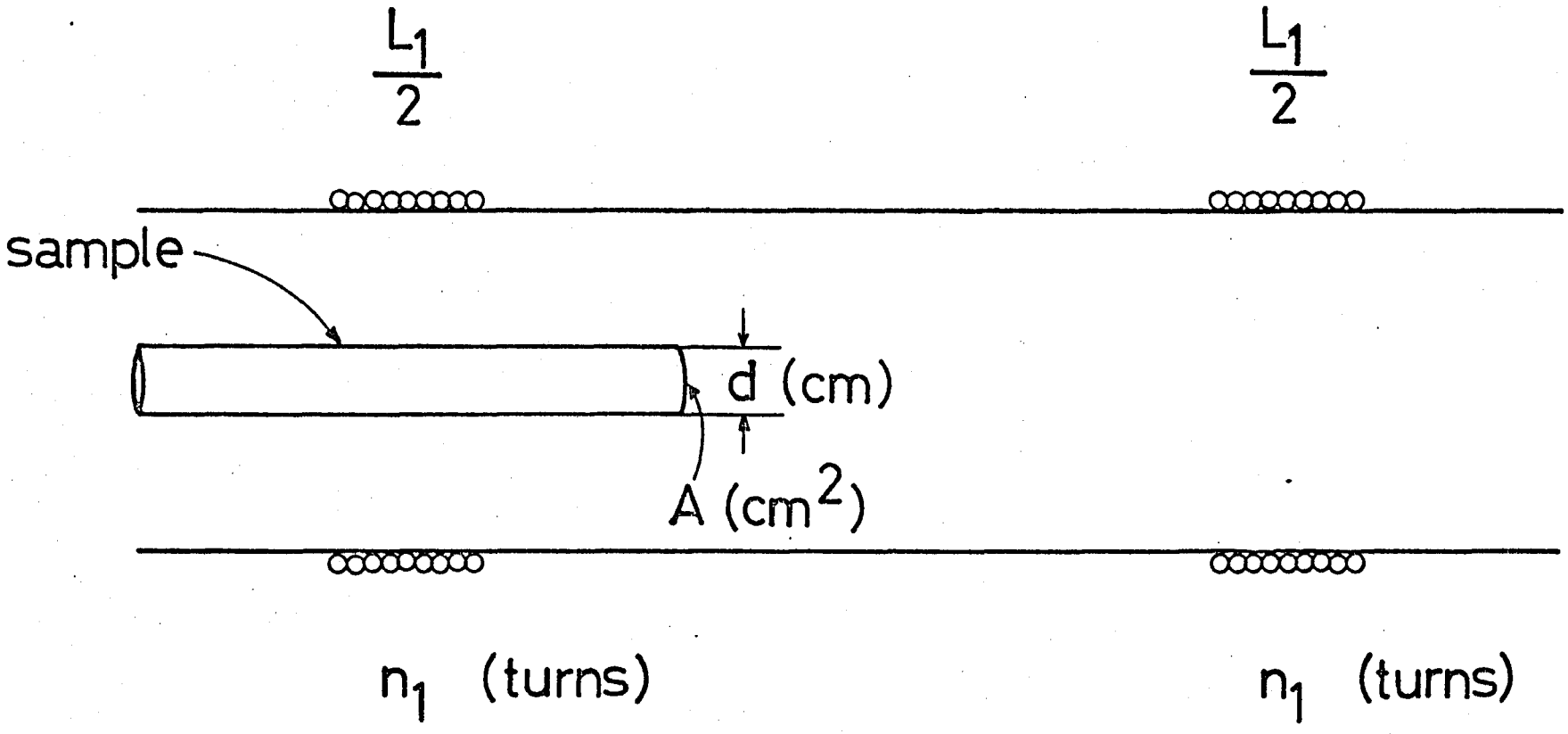

Fig.11

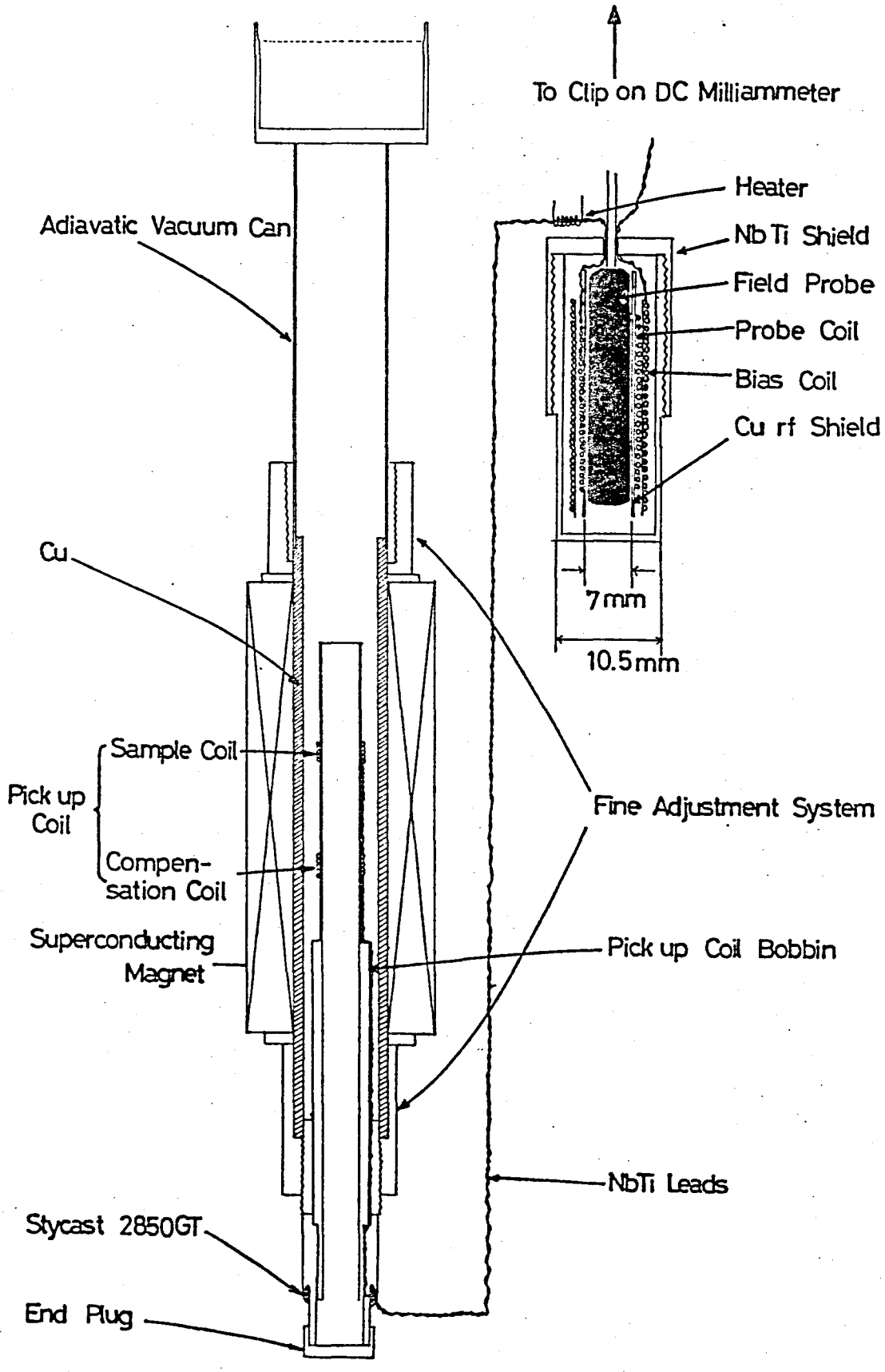
To Clip on DC Milliammeter
Heater
Adiavatic Vacuum Can
NbTi Shield
Field Probe
Probe Coil
Bias Coil
Cu rf Shield
Cu
7mm
10.5mm
Sample Coil
Pick up Coil
Compen-sation Coil
Fine Adjustment System
Superconducting Magnet
Pick up Coil Bobbin
NbTi Leads
Stycast 2850GT
End Plug

Fig.12

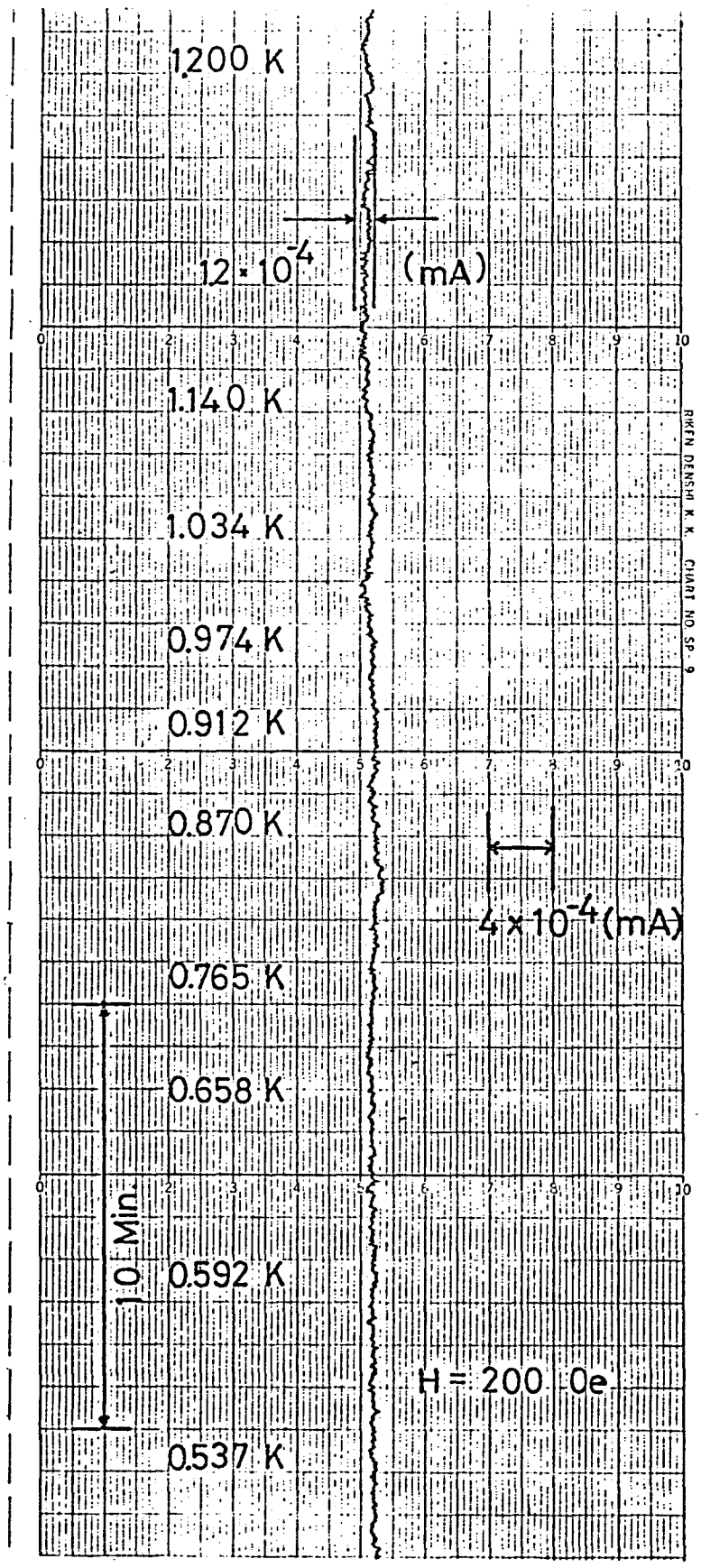
1.200 K
12 × 10⁻⁴ (mA)
1.140 K
1.034 K
0.974 K
0.912 K
0.870 K
4×10⁻⁴(mA)
0.765 K
0.658 K
10 Min.
0.592 K
H = 200 Oe
0.537 K
RIKEN DENSHI K.K. CHART NO. SP-9

Fig.13

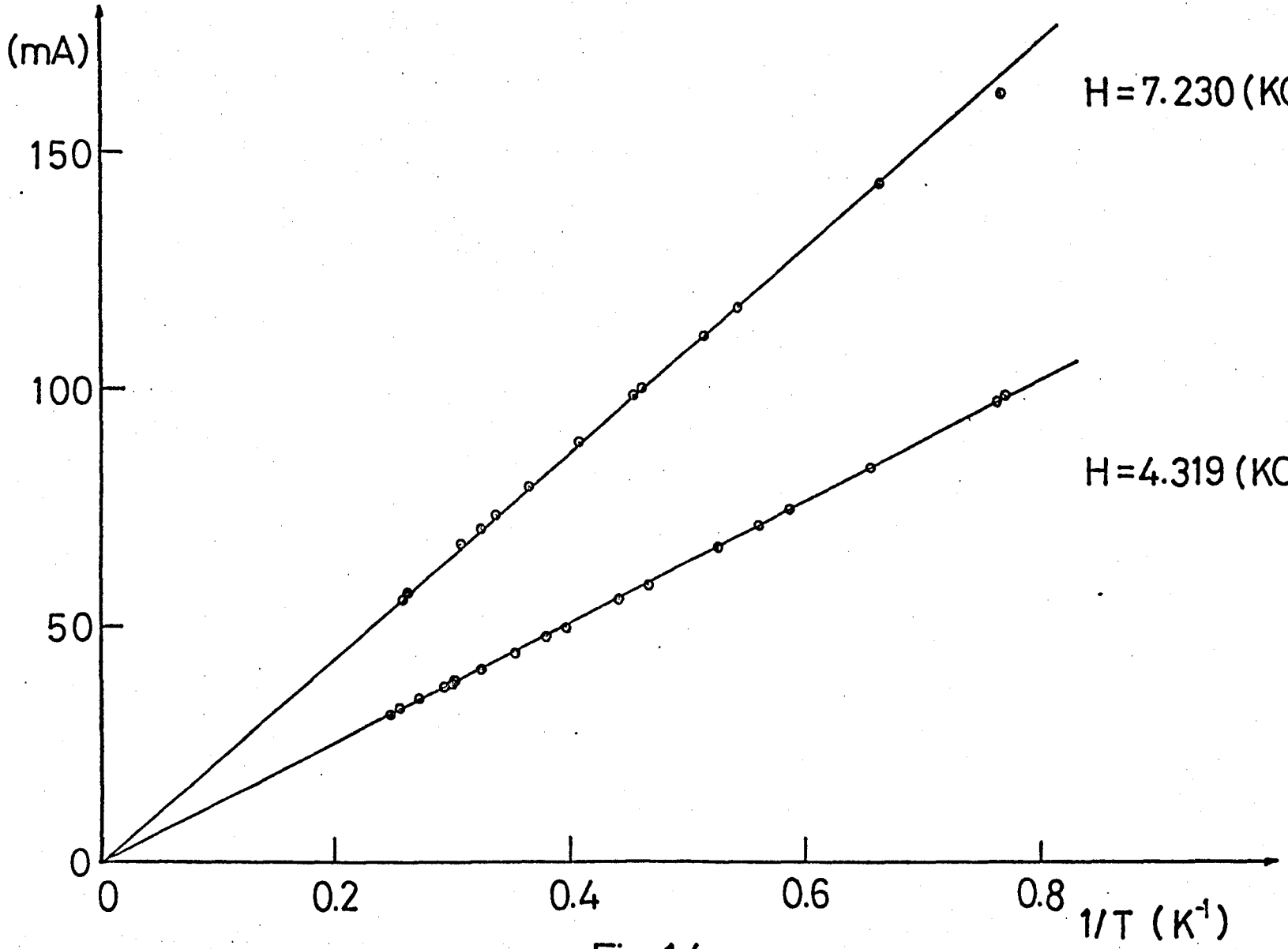

Fig.14

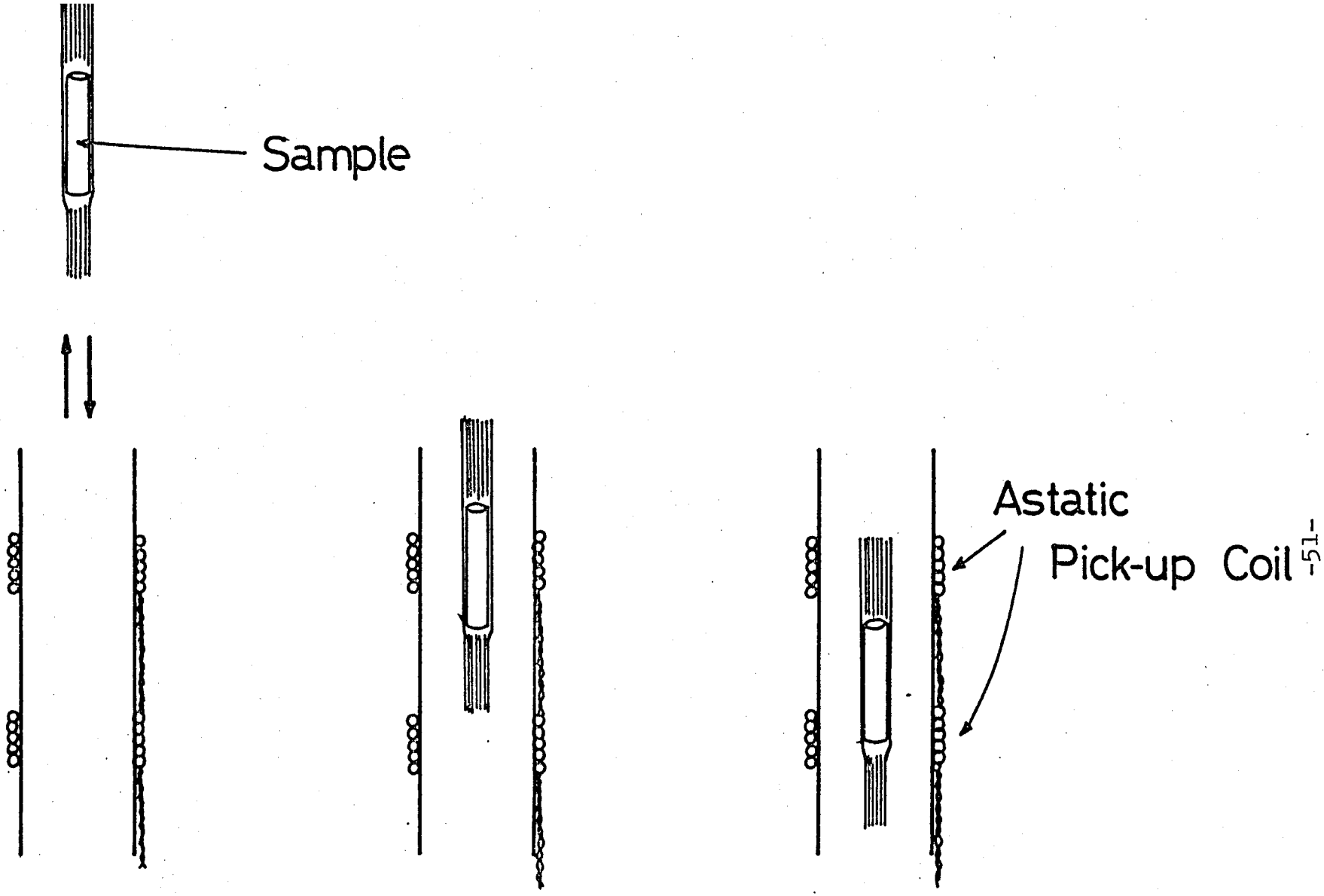

Fig.15a

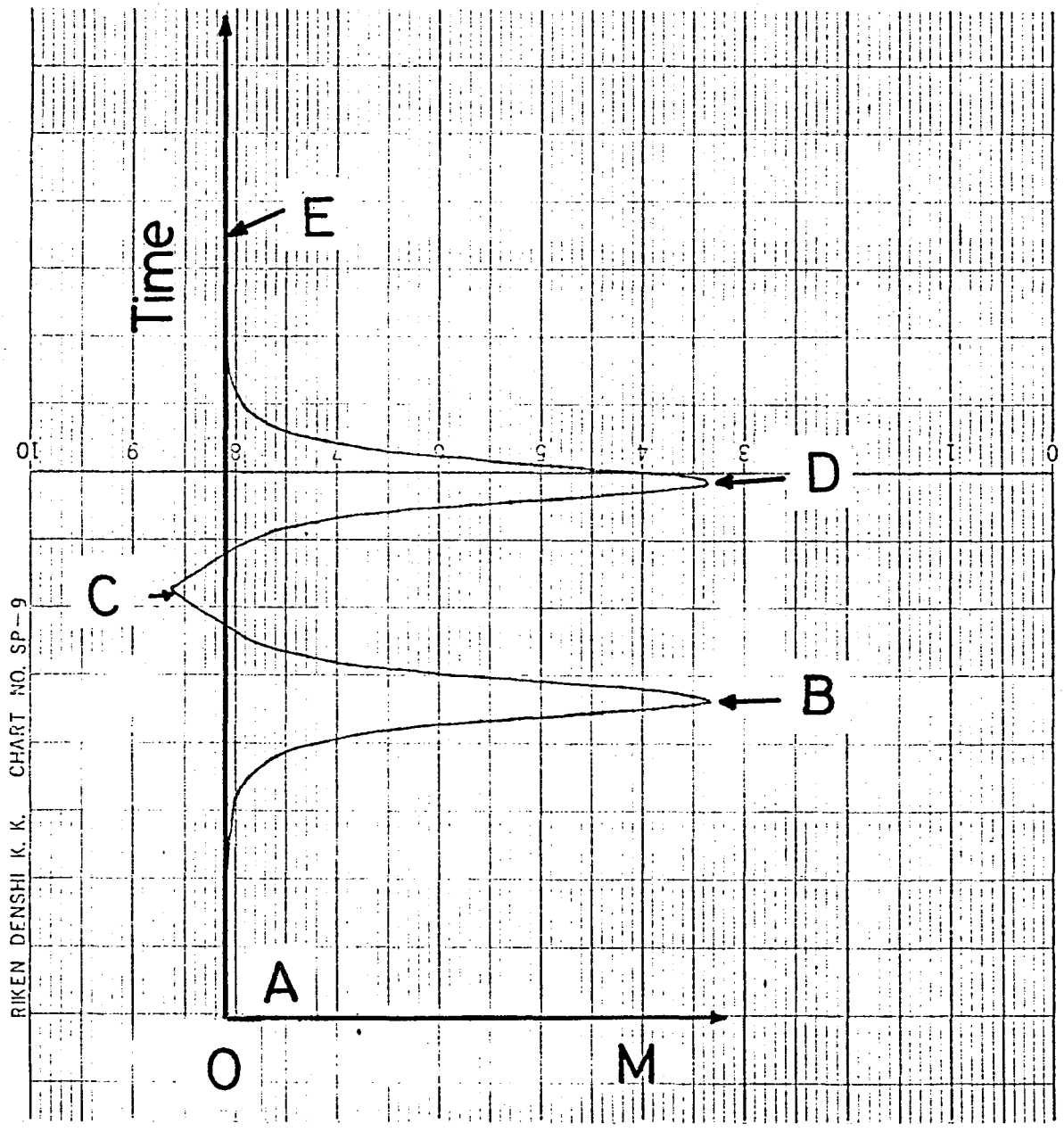

Fig. 15b

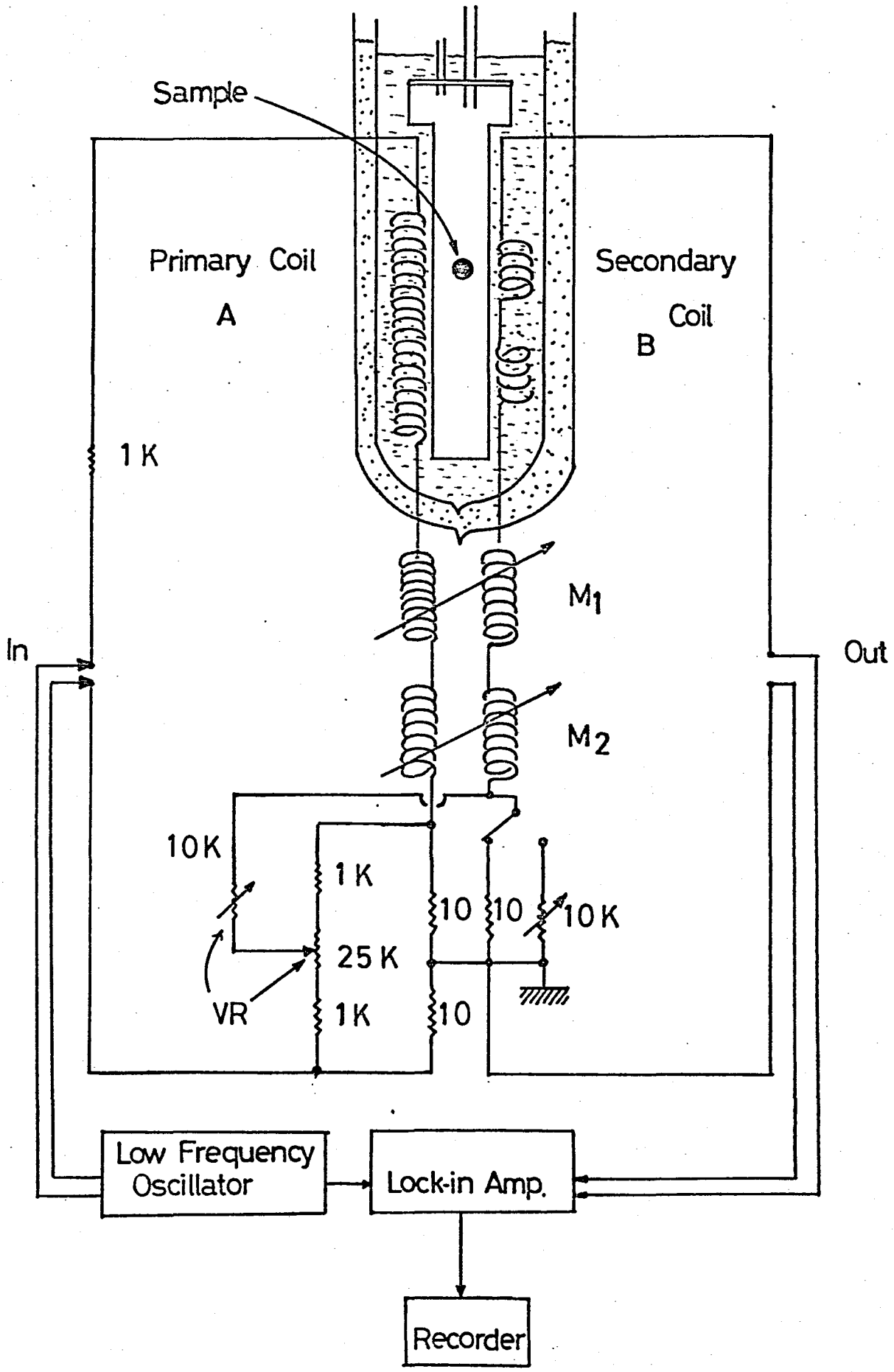
Sample
Primary Coil
A
Secondary
Coil
B
1 K
M1
M2
In
Out
10 K
1 K
10
10
10 K
25 K
VR
1 K
10
Low Frequency
Oscillator
Lock-in Amp.
Recorder

Fig.16

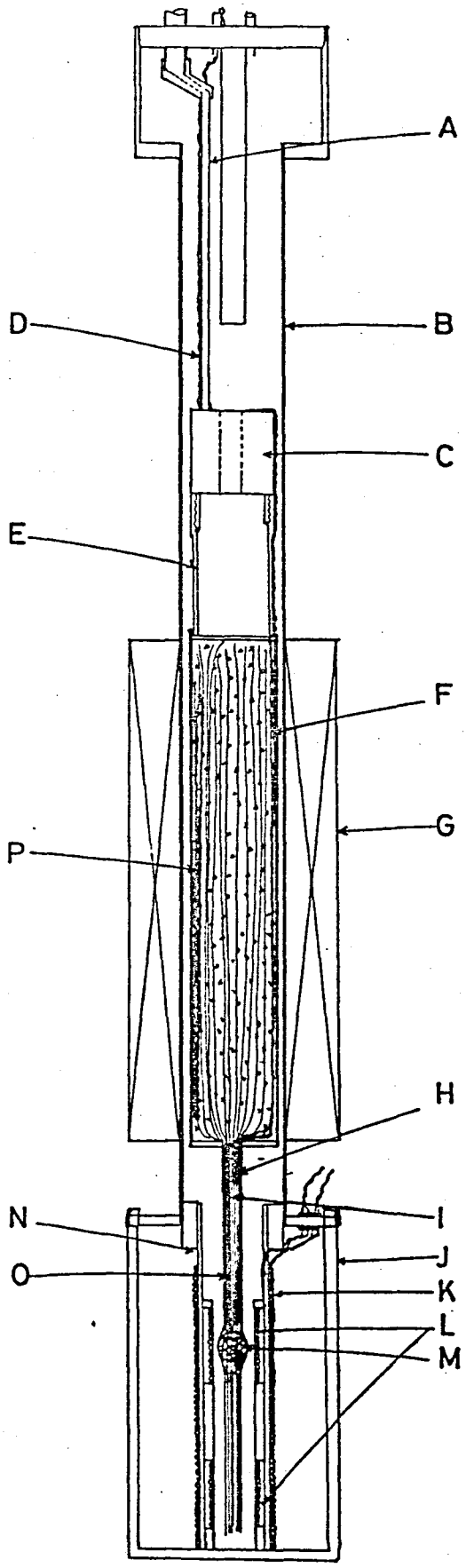

Fig.17

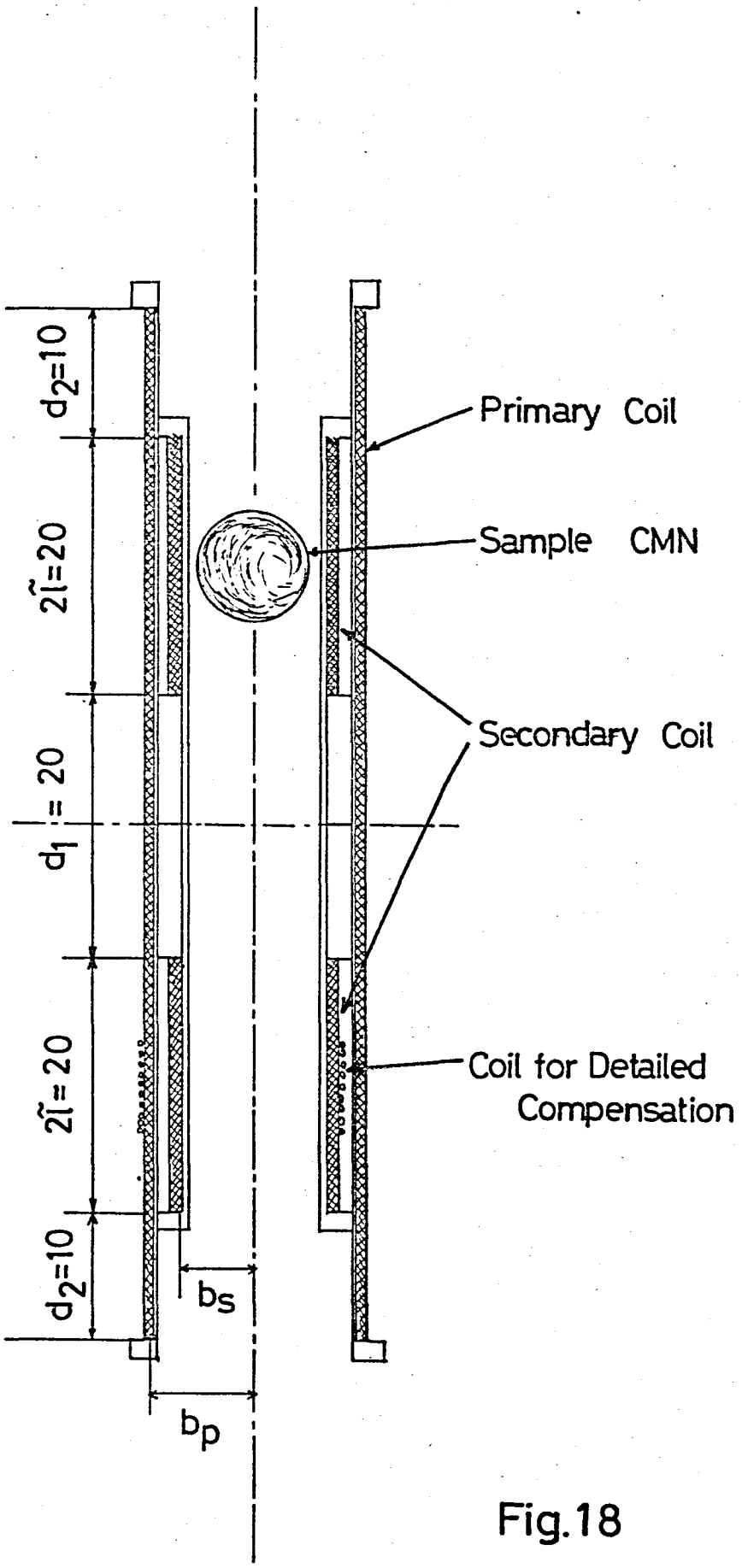
d_2=10
$2\tilde{l}$=20
d_1 = 20
$2\tilde{l}$= 20
d_2=10
b_s
b_p
Primary Coil
Sample CMN
Secondary Coil
Coil for Detailed Compensation

Fig.18

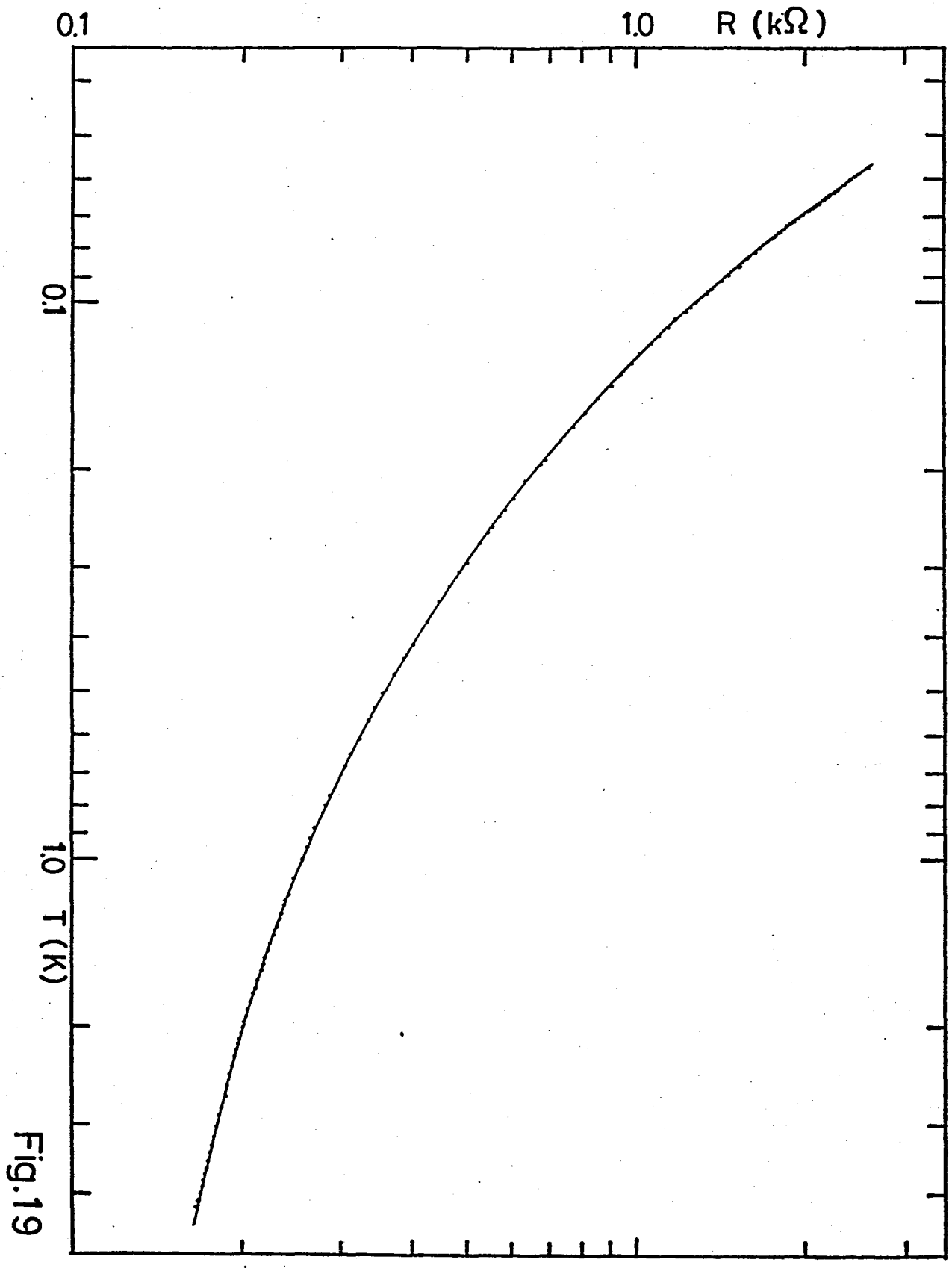

Fig.19

Part II

Electron Spin Resonance in Copper Sulphate Pentahydrate down to 100 mK

Synopsis

Copper sulphate pentahydrate $CuSO_4 \cdot 5H_2O$ is investigated by electron spin resonance at 9, 17, 24, 35 and 45 GHz bands down to about 100 mK using a combined cryostat of ^3He and adiabatic demagnetization described in Part I. Above 70 K the temperature dependent exchange interaction between two inequivalent sites A and B in the crystal is found. Below 20 K the temperature dependent shifts of resonance lines are observed and it is analized by taking into account the H/T effect in the dissimilar spin sites using the molecular field theory.

§ 1 Introduction

In recent years, there have been many intensive studies in magnetic properties of low dimensional ferro- or antiferromagnets. In contrust with usual three-dimensional magnets, these low dimensional magnets are characterized by the short-range ordering in a wide temperature range around its characteristic temperature zJ/k_B, where J is the main exchange interaction in the chain or layer and z is the number of the nearest neighbor interacting spins. In the short-range ordered region, many interasting magnetic behavior such as a broad peak in magnetic susceptibility and specific heat, the shift of g-value and the characteristic temperature dependent line width of ESR line have been observed by many researchers. In our laboratory, so far, ESR studies have been done to investigate the spin dynamics in the short-range ordering region as well as below T_N in some low dimensional antiferromagnets such as $Cu(NH_3)_4SO_4 \cdot H_2O$[1], $KCuF_3$[2], $Cu(HCOO)_2 \cdot 4H_2O$[3], TMMC[4], $Cu(C_6H_5COO)_2 \cdot 3H_2O$[5], $CuCl_2 \cdot 2NC_5H_5$[6], $Rb_2PbCu(NO_2)_6$[7] and $Cu(ND_3)_4SO_4 \cdot D_2O$[8] etc.

The series of the low dimensional magnet studies in our laboratory are now extended to $CuSO_4 \cdot 5H_2O$. According to the proton NMR experiments by Poulis et al.[9), 10)], this crystal consists of weakly coupled two spin systems A and B, where A and B spins belong to the inequivalent A and B sites, respectively. The A spin system shows a characteristic of Heisenberg antiferromagnetic linear chain and exibits a transition to a long-range ordered state at $T_c \simeq 100$ mK[11)], even though the B system is still paramagnetic at this temperature. This partial ordering[12)] of the A

spin in addition to the one-dimensional spin dynamics is one of the attractive subjects of the present ESR study.

ESR measurements of this compound were performed by Arnold and Kip[13], Wheatley and Halliday[14] and Bagguley and Griffiths[15]. The exchange splitting of ESR lines was first observed in Q band region by Bagguley et al.[15] and the exchange interaction between two crystallographic inequivalent spins was determined to be about 0.11 K at room temperature. The low temperature ESR measurement down to 1.2 K was performed by Abe et al.[16] in the plane containing the two inequivalent copper spins. They found that one of the two well-split lines at room temperature was anomalously broadened below 20 K at Q band measurements and they concluded that the line broadening comes from the short range ordering effect in the A site linear chain.

We performed the ESR measurements in $CuSO_4 \cdot 5H_2O$ using a combined cryostat of ^3He and adiavatic demagnetization in a temperature range from room temperature down to about 100 mK at 9, 17, 24, 35 and 45 GHz bands. One of the remarkable results is that the temperature dependent exchange interaction between two inequivalent sites of copper spins was observed above 70 K and it increases with decreasing temperature. The similar phenomenon was first observed by Okuda and Date[17] in $K_2CuCl_4 \cdot 2H_2O$ and $K_2CuCl_4 \cdot 2D_2O$. Another interesting result is that the temperature dependent shift of the resonance lines in a low temperature region below about 20 K to 0.5 K was observed. These resonance line shifts are analyzed by taking into account the H/T effect between the dissimilar sites A and B using the molecular field theory as

was done in some copper compounds by Kuroda et al.[18] These results are summerized in §3 and are discussed in §4.

§ 2 Crystal and Magnetic Structure

The X-ray analysis of the crystal structure of $CuSO_4 \cdot 5H_2O$ was performed by Beevers and Lipson[19] and neutron scattering experiment for the determinations of more detailed and complete atomic positions was done by Bacon and Curry[20]. According to their results, $CuSO_4 \cdot 5H_2O$ has a triclinic structure with space group C_i^1. The dimension of the unit cell is a = 6.141 Å, b = 10.736 Å and c = 5.986 Å, and the interaxial angles $\alpha = 82° 16'$, $\beta = 107° 26'$ and $\gamma = 102° 40'$[20]. The projection of the crystal structure on the ab-plane is shown in Fig. 1. The unit cell has two inequivalent Cu^{2+} ions at (0, 0, 0) and (1/2, 1/2, 0) positions, which are abbriviated as A and B sites, respectively, as shown in Fig. 1. Each of the two cupric ions is surrounded by four water molecules and two oxygen atoms of SO_4^{2-} group in a slightly distorted octahedral arrangement as shown in Fig. 2. The nomenclatures in Figs. 1 and 2 were quoted from the paper of Beevers and Lipson[19]. The two remaining H_2O molecules $9(H_2O)$ and $9'(H_2O)$ are at a somewhat long distance from both Cu^{2+} ions at A and B sites. Local electric fields acting on the two Cu^{2+} ions are nearly tetragonal. The angle θ between the two tetragonal axes of A and B sites which are defined as the lines connecting two oxygens belonging to the SO_4^{2-} group, and are called L_2 and L_4 directions[15], respectively, is 94.7°. The calculated

angular relations between the crystal and the two tetragonal directions using the data of Bacon and Curry[20] are shown in Fig. 3 and they are slightly different from those of previous data.[21]

Magnetic and thermal properties of this single crystal of $CuSO_4 \cdot 5H_2O$ were studied by many reserchers[21)-29)]. A broad maximum in the specific heat[24)] was found near 1 K and it was first believed that the B site copper ions make a one-dimensional chains along the c-axis. Recent proton NMR experiments[9),10),30)], however, showed that the A site copper ions along the a-axis are coupled by the dominant exchange interaction $J/k_B = -1.45$ K and compose the bundle of linear chains along the a-axis. Further NMR and specific heat investigations[11)] in lower temperatures showed the onset of antiferromagnetic long-range order in the A site copper ions at about 100 mK, even though the B site copper ions are still paramagnetic down to about 35 mK[29)]. The interchain exchange energy among the A site chains was estimated to be $zJ'/k_B \simeq -0.14 \pm 0.03$ K[11)]. These peculiar magnetic phase transition was also obtained in the similar isomorphous systems such as $CuSeO_4 \cdot 5H_2O$[12)] and $CuBeF_4 \cdot 5H_2O$[31),32)].

The g-tensors of A and B sites have the tetragonal symmetry corresponding to the symmetry of the crystal field acting on the Cu^{2+} ions and the values were determined by ESR measurements to be

$$\begin{cases} g_{\parallel} = 2.412 \pm 0.005 \\ g_{\perp} = 2.102 \pm 0.005 \end{cases} \qquad (1)$$

where $g_{\parallel}$ and $g_{\perp}$ mean the principal g-values parallel and perpendicular to the tetragonal axis, respectively. These values are consistent with the results of previous work [15), 16)]. Though the local environment of two Cu^{2+} ions belonging to the A and B sites is different, the principal g-tensors are almost the same. If the exchange interaction J_{AB} between two inequivalent sites A and B is sufficiently weak compared with the difference of the Zeeman energy between them, two well-split ESR lines should be observed. If the condition is opposite, two lines should be amalgamated. Considering the simplest exchange coupled two spin system, the splitting criterion is given as

$$\Delta g \mu_B H \simeq 2J_{AB} \tag{2}$$

where $\Delta g = g_A - g_B$, and g_A and g_B are g-tensors corresponding to two inequivalent copper spins. This exchange splitting phenomenon was first observed by Bagguley and Griffiths[15)] in the Q-band ESR at room temperature in $CuSO_4 \cdot 5H_2O$. According to above criterion, the exchange constant J_{AB} was determined by them to be $2J_{AB}/k_B \simeq$ 0.11 K at room temperature.

The linear chain mechanism of the exchange interaction may be understood by considering the configuration of the wave function of Cu^{2+} ions as follows: The Cu^{2+} ion in a tetragonal local environment has the ground state wave function of $d(x^2-y^2)$, which spreads in the plane of four H_2O molecules as shown in Fig. 2. This is confirmed by looking at the g-tensor symmetry. Thus, the exchange interaction through the path (I) of A site ions along the

a-axis as shown in Fig. 4 is considered to be dominant, compared with the other exchange path (II) along the c-axis. Other exchange interactions, i.e., the A-B and intra-B site interactions may be small compared with the path (I) exchange.

§ 3 Experimental and Results

(1) Experimental

Electron spin resonance was performed in the temperature range from room temperature down to about 100 mK at 35 and 45 GHz bands. Above 1.2 K the conventional transmission type of cryostat with 100 kHz field modulation was also used at the frequency 9, 17, 24, 35 and 45 GHz. The temperature was measured by using $AuCo_{2.1\%}$-Cu thermocouple. Below 1.2 K the combined ^3He and adiavatic demagnetization cryostat was used. The detailed construction and operation of this cryostat are described in A in Part I.

The crystal was grown from saturated aqueous solution by slow evaporation at room temperature and it has a well-developed [0,0,1]-zone plane.

In every experiments the sample was checked by taking the angular dependence of ESR lines at 35 GHz at room temperature in order to ascertain the desired direction of the crystal and to avoid the twin crystal. The setting error of the crystal direction is less than about $\pm$ 5° in the all present ESR measurements.

(2) Summary of The Experimental Results

(a) Temperature, Frequency and Angular Dependences of The Exchange Splitting

Most of the measurements were done in the plane including two tetragonal axes L_2 and L_4. Only one exchange narrowed line was observed at the 9 GHz band in all temperature region. Its angular dependences of the resonance line and line widths at the 9.385 GHz at various temperatures are shown in Fig. 5.

At the 35 GHz band, the exchange splitting phenomena were observed around the L_2 and L_4 axes as shown in Figs. 6 and 7. In Fig. 6, it is noticed that there exist two angles for the maximum separation corresponding to the L_2 and L_4 axes and the angle between the both axes is about 90°. The separated lines amalgamate to one line at about 29° ± 2° from the L_2 or L_4 axes. The observed exchange splitting is satisfactorily explained by the model that the local tetragonal axis of the A site points in the L_2 direction while the tetragonal axis of the B site is parallel to the L_4 axis as is pointed out by Bagguley and Griffiths[15]. A new information given in Figs. 6 and 7 is the temperature dependence of the exchange splitting. If the exchange constant J_{AB} were temperature independent, the splitting pattern should not depend on temperature. However, a clear temperature dependence is observed in Figs. 6 and 7. This means that the exchange constant becomes large as temperature decreases. The detailed discussions will be shown in §4.

At the 45 GHz band, the similar exchange splitting pattern was obtained as shown in Figs. 8 and 9. At the 35.758 GHz the

two split lines amalgamate to one line below about 70 K, while at the 45.35 GHz two separated lines can be observed.

The frequency dependence of the exchange splitting at room temperature is summalized in Fig. 10.

(b) Resonance Shifts

Temperature dependences of the resonance line from room temperature to 1.2 K at the 9.385 GHz in the field parallel to the L_2 and L_4 axes are shown in Fig. 11. The resonance lines shift with decreasing temperature to lower and higher field sides when an external field H is applied to the L_2 and L_4 directions, respectively.

The temperature dependences of the exchange splitting lines above about 70 K at the 35.640 GHz are shown in Figs. 12 and 13, when the external field H is applied parallel to the L_2 and L_4 axes, respectively. The magnitude of the exchange splitting becomes small with decreasing temperature as was explained in (a) in this section. This means that the exchange constant J_{AB} clearly depends on temperature. With decreasing temperature below about 70 K, the temperature dependent shifts of the amalgamated line were observed at the 35.640 GHz. When the external field H is applied parallel to the L_2 axis, the line shifts to higher field side between about 70 K and 0.5 K as shown in Fig. 12. When the field H is applied parallel to the L_4 axis, the shift is opposite as shown in Fig. 13.

In the 45 GHz band, similar temperature dependence of the exchange splittingwas observed above 70 K. However, the amalgama-

tion does not occur even in the low temperatures and the lower field lines always shift to lower field side below about 20 K as shown in Figs. 14 and 15. The intensities of the lower field lines become weaker and weaker with decreasing temperature below some tens Kelvin. When the external field H is applied parallel to the L_2 axis, the intensity of lower field line diminishes and the resonance line disapperas below about 3 K while the higher field line slightly shifts to higher field as shown in Fig. 14. When the field H is parallel to the L_4 axis, both resonance lines shift to lower field side and they become constant below about 0.5 K as shown in Fig. 15.

(c) Line Width

Angular dependences of the maximum slope width at 9 GHz band are shown in Fig. 5. The widths increase with increasing temperature above about 100 K in both L_2 and L_4 directions from about 80 Gauss to 150 Gauss. The temperature dependences of the line width are shown in Fig. 16.

The line widths in the 45 GHz band become sharper and sharper with decreasing temperature down to about 0.5 K and it becomes constant below about 0.5 K. Above 100 K the line widths rapidly decrease with decreasing temperature. The temperature dependences of the line widths at 45.388 GHz with the field H parallel to L_2 and L_4 axes are shown in Figs. 17 and 18, respectively. The widths in Figs. 17 and 18 are given by the full-half width.

§ 4 Discussions

(1) Temperature Dependence of Exchange Interaction

The temperature dependent exchange constant J_{AB} is estimated by using the data in Figs. 6, 8, 12, 13, 14 and 15, as is shown in Fig. 19. The experimental results shows that the exchange interaction $2J_{AB}/k_B$ between Cu^{2+} ions increases with decreasing temperature up to 0.24 K. Below about 70 K, J_{AB} becomes constant and it is about two times larger than that at room temperature. Our data of J_{AB} at room temperature is slightly larger than that of Bagguley and Griffiths[15] as shown in Fig. 19.

There are two possible mechanisms for explaining the temperature dependence. One of the mechanisms is expressed in the following way: if there are two competing ferro- and antiferromagnetic interactions between the A and B sites and a small difference in temperature coefficients between the ferro- and antiferromagnetic interaction exists,[17] the temperature dependence of the resultant exchange interaction will occur. The other one is that the exchange path between copper ions is modifyed by the rotational motion of H_2O molecules connecting the A and B sites ions. It is known from the NMR experiment[33] that the rotational vibration is strongly temperature dependent. Anyway, however, there is no definite evidence for explaining the large temperature dependence in J_{AB}.

(2) Paramagnetic Resonance Shift at Low Temperature

The shift of the resonance lines between about 20 K and 0.5 K as is shown in Figs. 14 and 15 can be explained in the following way. $CuSO_4 \cdot 5H_2O$ has two inequivalent sites A and B with different $\hat{g}$-tensors and the both sites are coupled with a relatively weak exchange interaction compared with the difference of the Zeeman energy. When the one site spins in $CuSO_4 \cdot 5H_2O$ is just on resonance, the other site spins is at rest. The spins at rest give the molecular field due to the weak exchange coupling to the other site spins. As this molecular field should be proportional to the polarization of the spins at rest, the shift depends on both the temperature and magnetic field. The mechanism of the shift considered here different from the shift introduced by Nagata et al.[34), 35)] for explaining the shift in low dimensional magnets.

The shift discussed here was first presented by McMillan and Opechowski[36), 37)] using the technique of the moment expansion method. They calculated the first moment by using the trancation method of the total Hamiltonian taking into account the dissimilarity of the A and B spins under the condition that $\Delta g \mu_B H >> 2J_{AB}$. One of the experimental example to this theory was done by Svare and Seidel[38)] in $K_2Cu(SO_4)_2 \cdot 6H_2O$. However, it is not suitable to apply above theory to the shift in the present case of $CuSO_4 \cdot 5H_2O$ because the exact calculation of the first moment is difficult and the condition is not always well satisfied.

Recently, the molecular field approach to the shift of the resonance lines was done by Kuroda et al.[18)] taking into account the H/T effect in order to analize the exchange splitting in some

copper compounds such as $(NH_4)_2CuCl_4 \cdot 2H_2O$, $(NH_4)_2CuBr_4 \cdot 2H_2O$ and $Cu(NH_3)_4SO_4 \cdot H_2O$ in submillimater ESR experiments at liquid ^4He temperature using pulse high magnetic field at Osaka University. This treatment is based on the classical molecular field theory of ferrimagnetic materials developed by Wangsness[39].

The essential point of the theory is as follows. When there are two inequivalent spins with different g-tensors g_A and g_B in crystal, the system can be regarded as a two sublattice system of M_A and M_B with different g-tensors g_A and g_B, respectively. The treatment is not appropriate at high temperature region but it is applicable at low temperature because the polarizations of the sublattice magnetizations become large. The two sublattices are connected to each other by the molecular field coming from the exchange interaction between inequivalent sites A and B. The temperature dependence of the resonance shift can be estimated by the temperature dependence of the sublattice moments and it can be easily be calculated.

The resonance frequencies ω^+ and ω^- given by Wangsness[39] in a spherical and isotropic ferrimagnet can be written by

$$\omega^{\pm} = \{\gamma H - \frac{A}{2}(\gamma_A M_{Bz} + \gamma_B M_{Az})\}$$

$$\pm \frac{1}{2}[\{\Delta\gamma H - A(\gamma_A M_{Bz} - \gamma_B M_{Az})\}^2 + 4\gamma_A\gamma_B A^2 M_{Az} M_{Bz}]^{1/2} \quad (3)$$

where γ_A and γ_B are the gyromagnetic ratios of the two sublattices M_A and M_B, respectively. γ and $\Delta\gamma$ are defined as $\gamma = (\gamma_A + \gamma_B)/2$ and $\Delta\gamma = \gamma_A - \gamma_B$. The molecular field constant A is given by

$A = 2zJ_{AB}/N\gamma_A\gamma_B h^2$, where N is the number of the spins in a sublattice, z is the number of interacting spins. M_{Az} and M_{Bz} are the magnetic moments along the field for A and B sublattices, respectively. The transverse components of them are assumed to be small. The shifts ΔH^+ and ΔH^- corresponding to ω^+ and ω^-, respectively, are written as

$$\Delta H^+ = -\frac{1}{2}\{\delta H + A(M_{Az} + M_{Bz})\} + \frac{1}{2}[\{\delta H + A(M_{Bz} - M_{Az})\}^2 + 4A^2 M_{Az} M_{Bz}]^{1/2} \quad (4)$$

and

$$\Delta H^- = \frac{1}{2}\{\delta H - A(M_{Az} + M_{Bz})\} - \frac{1}{2}[\{\delta H + A(M_{Bz} - M_{Az})\}^2 + 4A^2 M_{Az} M_{Bz}]^{1/2}, \quad (5)$$

Where δH is the difference of the resonance fields at sufficiently high temperatures.

Temperature dependence of the resonance field was calculated as follows. As the exchange interaction J_{AB} between A and B sites was obtained by ESR measurements around 70 K to be $2|J_{AB}|/k_B$ = 0.236 K, the molecular field constant A is calculated with z = 2 assuming J_{AB} to be ferromagnetic. The temperature dependence of M_{Az} is obtained by using the experimental results of NMR[10]. On the other hand, the temperature dependence of M_{Bz} is obtained by a simple Brillouin function because the B site is paramagnetic.

Hence, the shifts of the resonance fields ΔH^+ and ΔH^- can be calculated by using eqs. (4) and (5), respectively.

The calculated ΔH^+ and ΔH^- for the 45 GHz region are shown in Figs. 20 and 21, where the experimental results are also given. Satisfactory agreement between the theory and experiments is obtained for the B site, while a considerable deviation is found for the A site shift. The deviation in the A site may be explained by considering the short-range ordering effect[34]. However, the numerical estimation is difficult because the calculation of the correlation function in our case is not so simple.

When the exchange interaction is ferromagnetic, the intensity of the lower field resonance should be weak[18] and the experimental results support it. This result means that our assumption of the ferromagnetic J_{AB} is correct.

In 9 GHz region, a relation $\Delta g\mu_B H \leq 2J_{AB}$ holds so that the resonance lines belonging to two different Cu^{2+} ions are amalgamated by the exchange interaction. The molecular field theory can also be applicable for this condition. The resonance formula for the low frequency mode is written as[39]

$$\omega = \gamma_{eff} H, \tag{6}$$

where

$$\gamma_{eff} = \frac{M_{Az} + M_{Bz}}{M_{Az}/\gamma_A + M_{Bz}/\gamma_B}. \tag{7}$$

The experimental results of the shift in $CuSO_4 \cdot 5H_2O$ can satisfact-

orily be described by the theory as shown in Fig. 22.

As shown in Figs. 17 and 18, the line widths decrease with decreasing temperature and they become constant below 0.5 K. If the A site is antiferromagnetic below about 100 mK[11], the short-range order broadening may occur near T_N but it is not observed. This may be understood by the model that the external field surpresses the spin fluctuation and the broadening effect is reduced.

References

1). K. Oshima : Thesis in Osaka University.

2). M. Ikebe and M. Date : J. Phys. Soc. Jpn. 30 (1971) 93.

3). Y. Morimoto and M. Date : J. Phys. Soc. Jpn. 29 (1970) 1093.

4). K. Okuda, K. Oshima and M. Date : J. Phys. Soc. Jpn. 44 (1978) 801.

5). K. Oshima, K Okuda and M. Date : J. Phys. Soc. Jpn. 44 (1978) 757.

6). K. Okuda and K. Kadowaki : J. Phys. Soc. Jpn. 46 (1979) 45.

7). to be published in J. Phys. Soc. Jpn.

8). to be published in J. Phys. Soc. Jpn.

9). S. Wittekoek, N. J. Poulis and A. R. Miedema : Physica 30 (1964) 1051.

10). S. Wittekoek, T. O. Klaassen and N. J. Poulis : Physica 39 (1968) 293.

11). M. W. Van Tol and N. J. Poulis : Physica 69 (1973) 341.

12). T. O. Klaasen and N. J. Poulis : Phys. Rev. Lett. 36 (1976) 1252.

13). R. D. Arnold and A. F. Kip : Phys. Rev. 75 (1949) 1199.

14). J. Wheatley and D. Halliday : Phys. Rev. 75 (1949) 1412.

15). D. M. S. Bagguley and J. H. E. Griffiths : Proc. Roy. Soc. A201 (1950) 366.

16). H. Abe and K. Koga : J. Phys. Soc. Jpn. 18 (1963) 153.

17). T. Okuda and M. Date : J. Phys. Soc. Jpn. 28 (1970) 308.

18). S. Kuroda : J. appl. Phys. 50 (1979) 7762.

19). C. A. Beevers and H. Lipson : Proc. Roy. Soc. A146 (1934) 570.

20). G. E. Bacon and N. A. Curry : Proc. Roy. Soc. A266 (1962) 95.

21). K. S. Krishnan and A. Mookherji : Phys. Rev. 54 (1938) 533.

22). R. J. Benzie and A. H. Cooke : Proc. Phys. Soc. 64 (1951) 124.

23). T. H. Geballe and W. F. Giauque : J. Am. Chem. Soc. 74 (1952) 3513.

24). A. R. Miedema, H. Van Kempen, T. Haseda and W. J. Huiskamp : Physica 28 (1962) 119.

25). R. J. Anderson and W. F. Giauque : J. Chem. Phys. 46 (1967) 2413.

26). W. F. Giauque, R. A. Fisher, E. W. Hornung and G. E. Brodale : J. Chem. Phys. 48 (1968) 3728.

27). W. F. Giauque, E. W. Hornung, G. E. Brodale and R. A. Fisher : J. Chem. Phys. 48 (1968) 3906.

28). W. F. Giauque, G. E. Brodale, R. A. Fisher and E. W. Hornung : J. Chem. Phys. 49 (1968) 1848.

29). W. F. Giauque, R. A. Fisher, E. W. Hornung and G. E. Brodale : J. Chem. Phys. 53 (1970) 3733.

30). S. Wittekoek and N. J. Poulis : Physica 32 (1966) 693.

31). L. S. J. M. Henkens, K. M. Diederix, T. O. Klaassen and N. J. Poulis : Physica 81B (1976) 259.

32). T. O. Klaassen, L. S. J. M. Henkens and N. J. Poulis : Physica 86-88B (1977) 634.

33). G. Soda and T. Chiba : J. Chem. Phys. 50 (1969) 439.

34). K. Nagata and Y. Tazuke : J. Phys. Soc. Jpn. 32 (1972) 337.

35). K. Nagata, Y. Tazuke and K. Tsushima : J. Phys. Soc. Jpn. 32 (1972) 1486.

36). M. McMillan and W. Opechowski : Can. J. Phys. 38 (1960) 1168.

37). M. McMillan and W. Opechowski : Can. J. Phys. 39 (1961) 1369.

38). I. Svare and G. Seidel : Phys. Rev. A134 (1964) 172.

39). R. K. Wangsness : Phys. Rev. 91 (1953) 1085.

Figure Caption

Fig. 1. Crystal structure of $CuSO_4 \cdot 5H_2O$ projected on the ac plane. Unit cell consists of two inequivalent Cu^{2+} ions at A (0,0,0) and B (1/2,1/2,0) positions with different tetragonal axes L_2 and L_4, respectively. Lattice constants and interaxial angles are also shown. The nomenclatures were quoted from Beevers and Lipson[19].

Fig. 2. Local octahedral atomic arrangement around two inequivalent Cu^{2+} ions A (0,0,0) and B (1/2,1/2,0). Atomic distances are also shown.

Fig. 3. Angular relation between two tetragonal axes L_2 and L_4, and crystal axes a, b and c. Interaxial angle θ between two tetragonal axes L_2 and L_4 is 94.7°.

Fig. 4. Probable exchange linkages about Cu^{2+} ion at A (0,0,0).

Fig. 5. Angular dependence of the amalgamated line and its width at 9.385 GHz at various temperature.

Fig. 6. Angular dependence of the exchange splitting in L_2L_4-plane at 35.758 GHz above 70 K. Two exchange split lines were observed around L_2 and L_4 axes forming two circles in the plane and they shrink with decreasing temperature.

Fig. 7. Angular dependence of the amalgamated line in L_2L_4 plane at 35.758 GHz in low temperature region. Only one line is observed in all directions. Angular dependence of the exchange splitting at room temperature is also given in the figure.

Fig. 8. Angular dependence of the exchange splitting in L_2L_4 plane at 45.35 GHz above 70 K. Two exchange split lines

are observed around L_2 and L_4 axes.

Fig. 9. Angular dependence of the exchange splitting in L_2L_4 plane at 45.515 GHz in low temperature region. Angular dependence of the exchange splitting at room temperature is also given in the figure.

Fig. 10. Frequency dependence of the exchange splitting at room temperature when the external field H is parallel to L_2 axis. Exchange splitting occurs at 18 GHz and the estimated exchange constant $2|J_{AB}|/ k_B$ is about 0.12 K.

Fig. 11. Temperature dependent shifts of the amalgamated line at 9.411 GHz when the external field H is parallel to L_2 and L_4 axes.

Fig. 12. Temperature dependence of the exchange splitting at 35.640 GHz from room temperature down to about 100 mK when external field H is parallel to L_2 axis. The temperature dependent exchange splitting is observed above 70 K.

Fig. 13. Temperature dependence of the exchange splitting at 35.640 GHz from room temperature down to about 100 mK when the external field H is parallel to L_4 axis. The temperature dependent exchange splitting is observed above 70 K.

Fig. 14. Temperature dependence of the exchange splitting at 45.388 GHz from room temperature down to about 100 mK when the external field H is parallel to L_2 axis. Below about 3 K, the lower field resonance line diminishes and disappears.

Fig. 15. Temperature dependence of the exchange splitting at 45.388 GHz from room temperature down to about 100 mK when the external field H is parallel to L_4 axis.

Fig. 16. Temperature dependence of the amalgamated lines at 9.411 GHz when the external field H is parallel to L_2 and L_4 axes, respectively.

Fig. 17. Temperature dependence of the resonance line widths at 45.388 GHz when the external field H is parallel to L_2 axis.

Fig. 18. Temperature dependence of the resonance line widths at 45.388 GHz when the external field H is parallel to L_4 axis.

Fig. 19. Temperature dependence of the exchange interaction J_{AB} between A and B sites Cu^{2+} ions. Exchange constants obtained by Bagguley et al.[15] at room temperature are also given by open circles, respectively.

Fig. 20. Comparison between experimental results and molecular field theory at 45.388 GHz when the external field H is parallel to L_2 axis.

Fig. 21. Comparison between experimental results and molecular field theory at 45.388 GHz when the external field H is parallel to L_4 axis.

Fig. 22. Comparison between experimental results and molecular field theory at 9.411 GHz when the external field H is parallel to L_2 and L_4 axes, respectively.

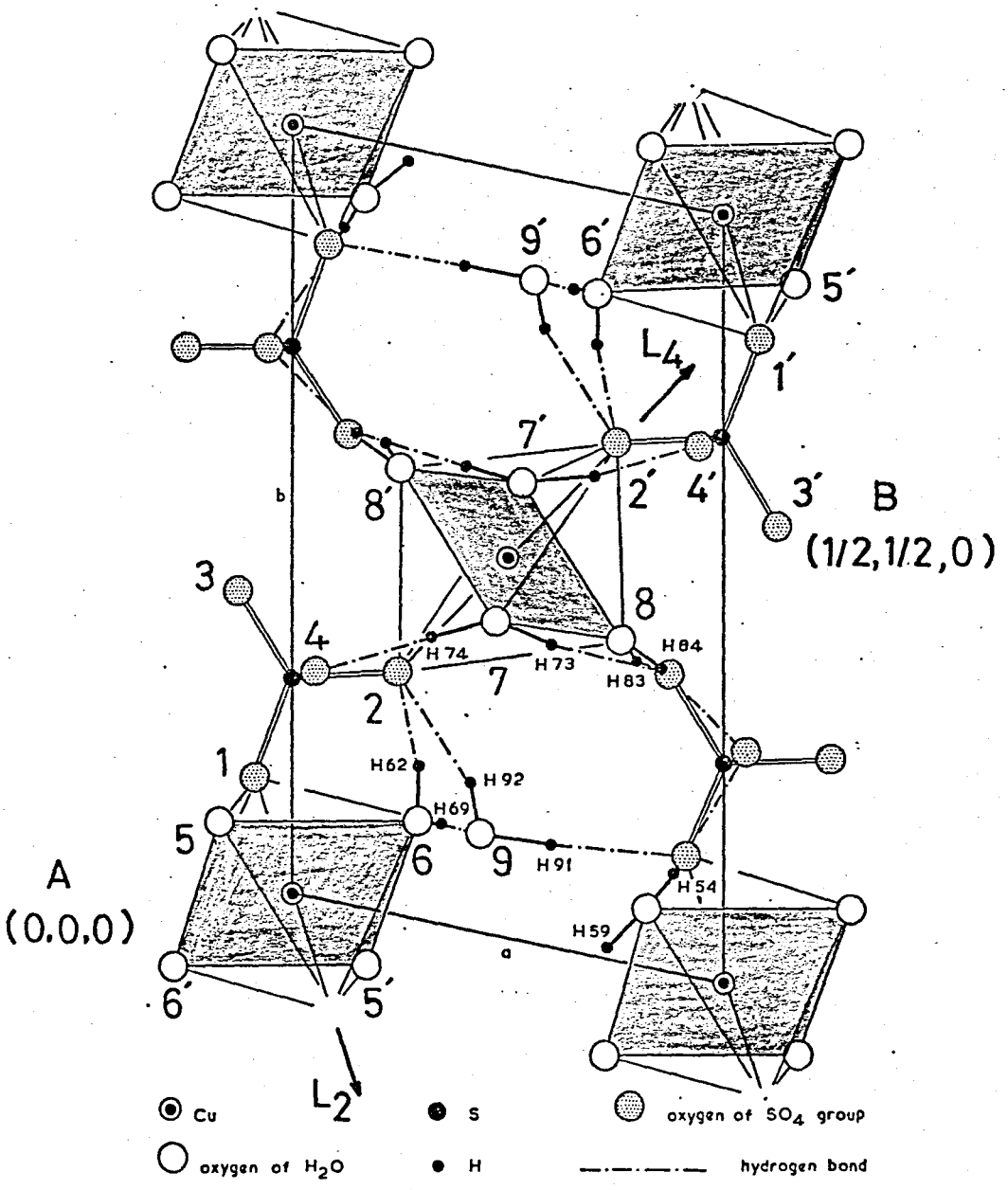

$$\begin{cases} a = 6.141 \text{ Å} \\ b = 10.736 \text{ Å} \\ c = 5.986 \text{ Å} \end{cases} \qquad \begin{cases} \alpha = 82^{\circ}16' \\ \beta = 107^{\circ}26' \\ \gamma = 102^{\circ}40' \end{cases}$$

triclinic

space group C_i^1

Fig. 1

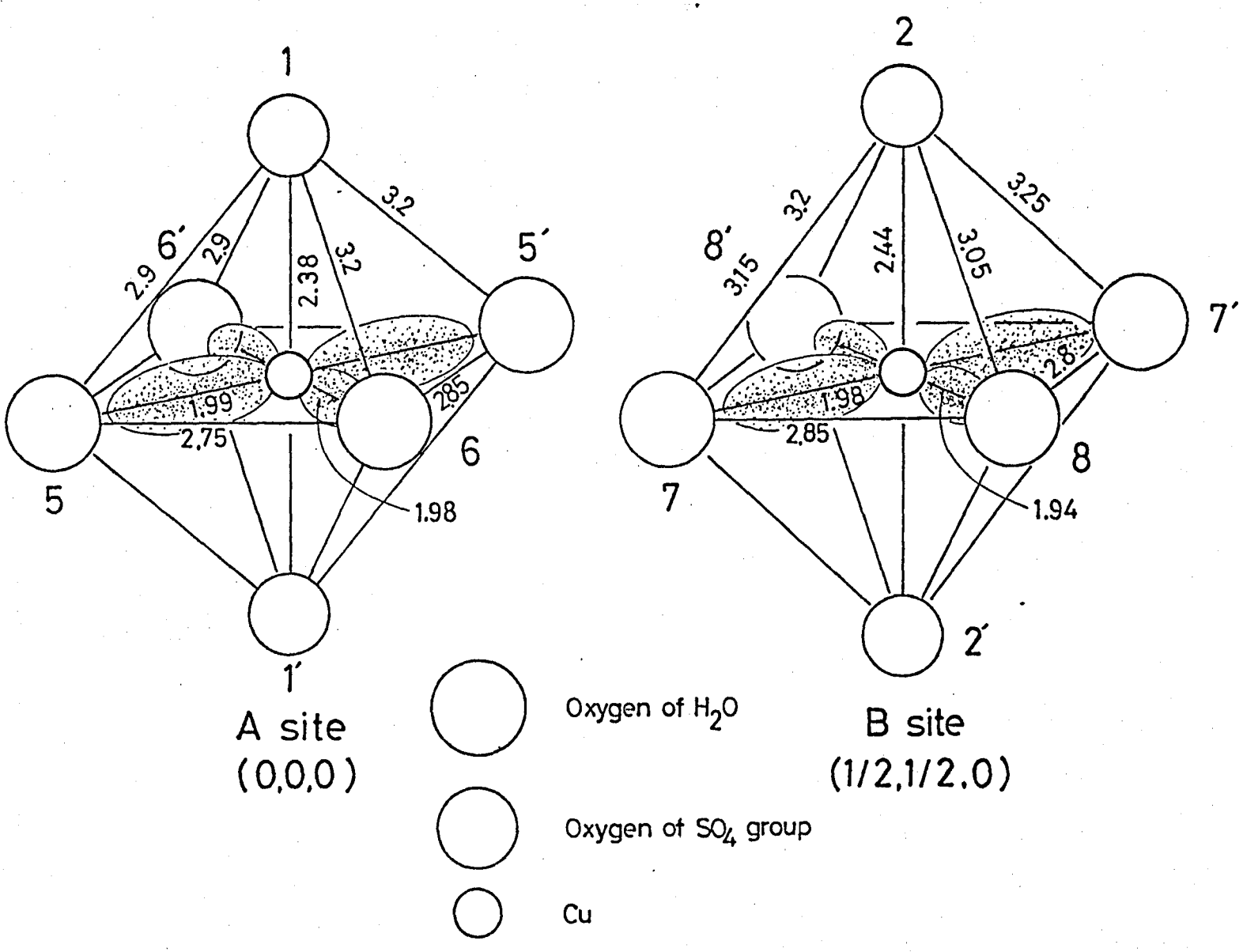
1
2
2.9
6'
2.9
2.38
3.2
3.2
5'
1.99
2.75
2.85
6
5
1.98
1'
A site
(0,0,0)
3.2
3.15
8'
2.44
3.05
3.25
7'
1.98
2.85
2.8
8
7
1.94
2'
B site
(1/2,1/2,0)
Oxygen of H_2O
Oxygen of SO_4 group
Cu

Fig. 2

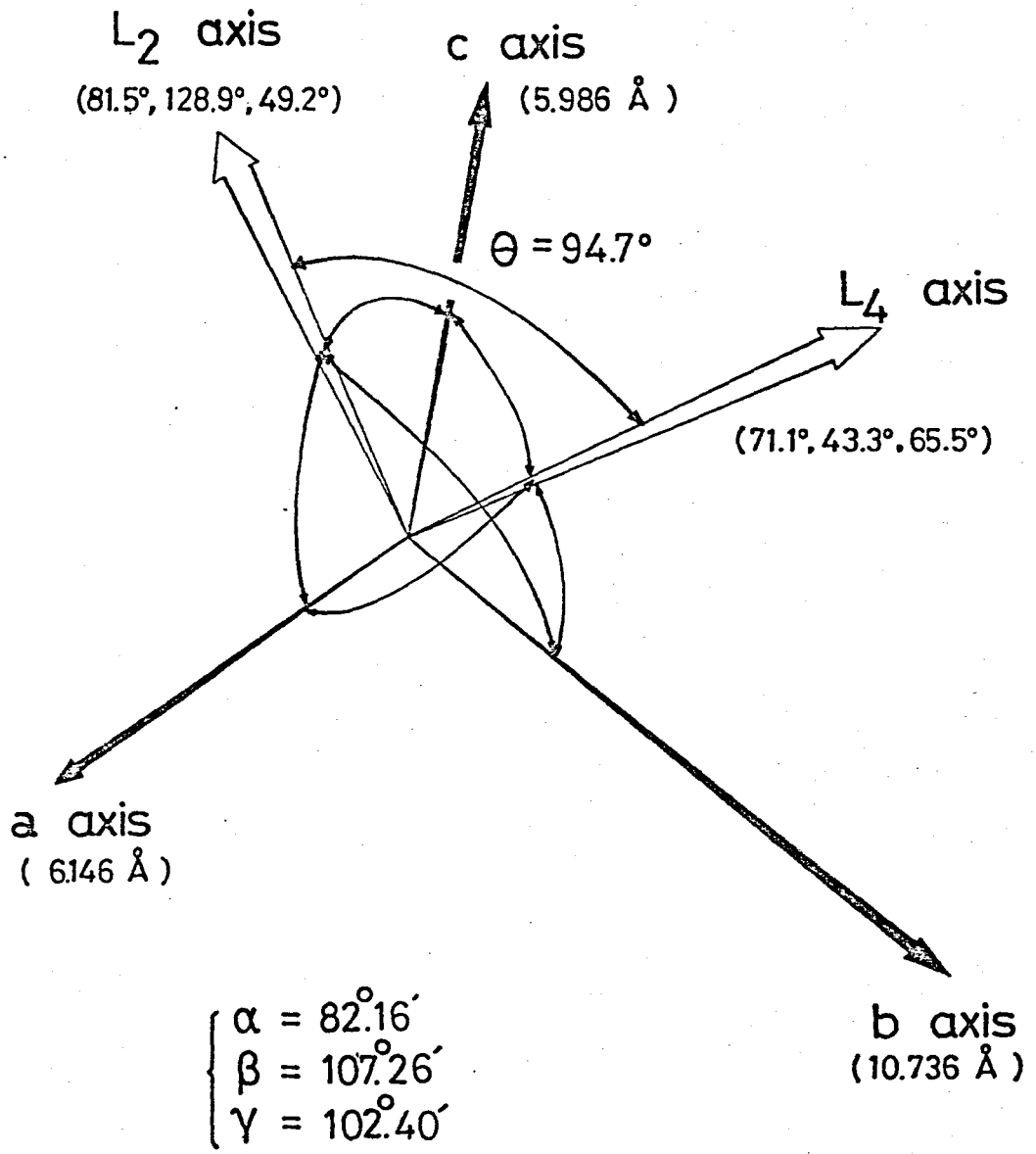
L2 axis
(81.5°, 128.9°, 49.2°)
c axis
(5.986 Å)
θ = 94.7°
L4 axis
(71.1°, 43.3°, 65.5°)
a axis
(6.146 Å)
α = 82°16′
β = 107°26′
γ = 102°40′
b axis
(10.736 Å)

Fig. 3

Cu^{2+} (0, 0, 0)

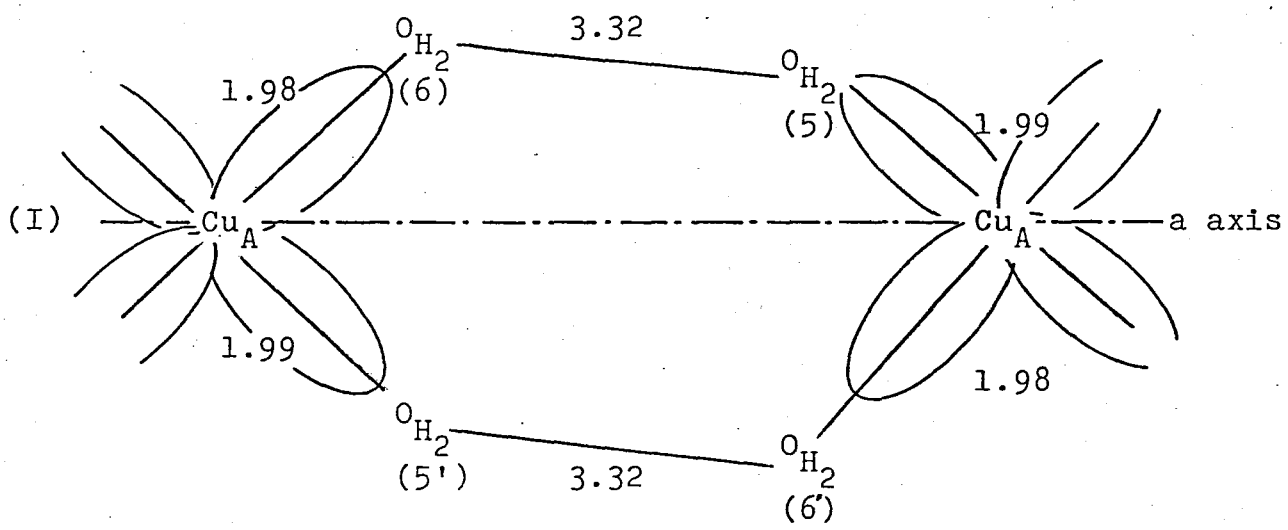

total 7.29 Å

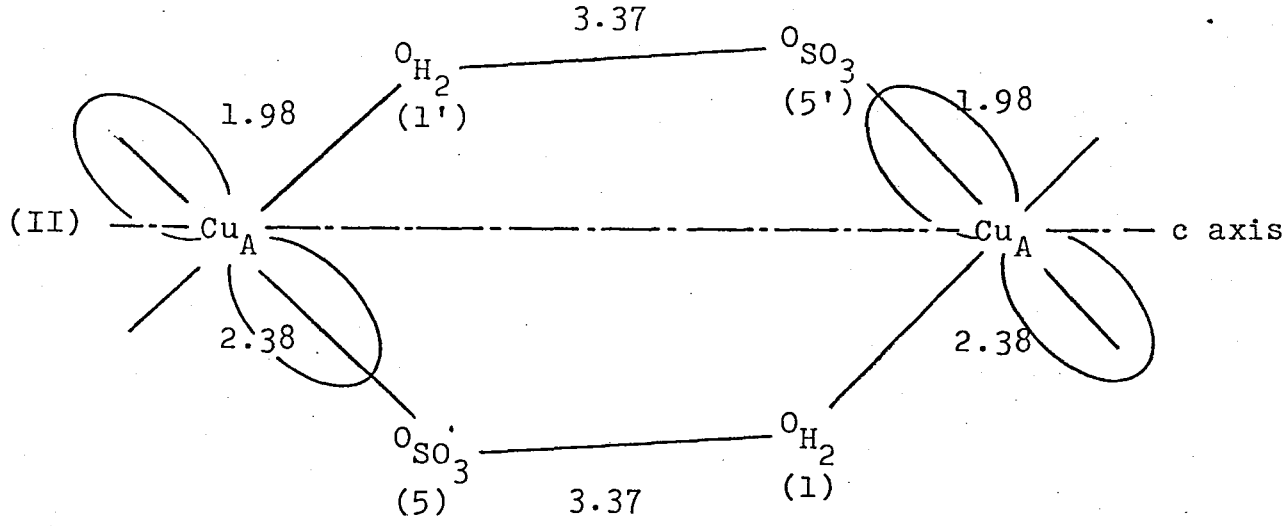

total 7.73 Å

Fig.4

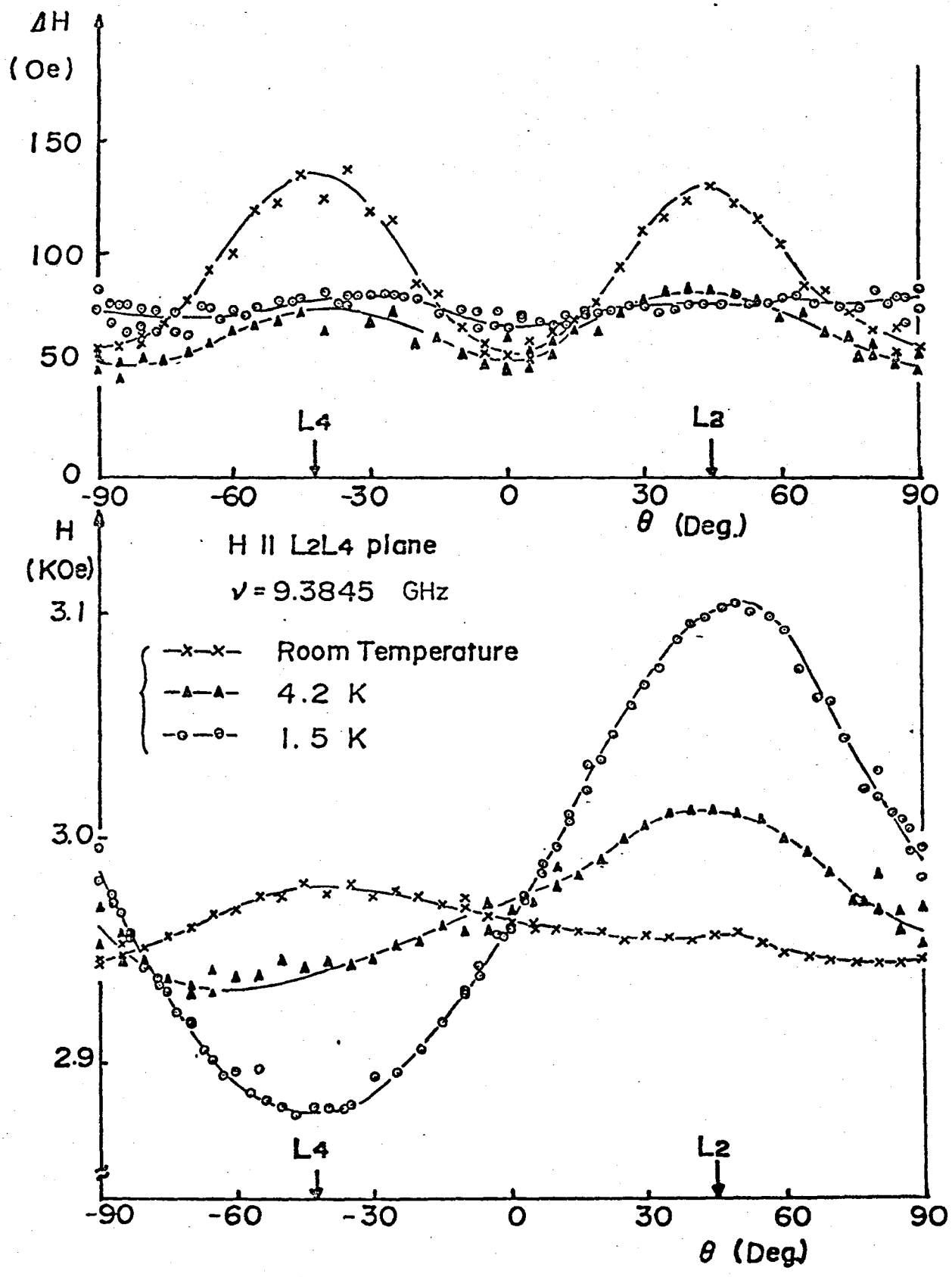
ΔH
(Oe)
150
100
50
0
L4
L2
-90
-60
-30
0
30
60
90
θ (Deg.)
H
(KOe)
H ll L2L4 plane
ν = 9.3845 GHz
Room Temperature
4.2 K
1.5 K
3.1
3.0
2.9
L4
L2
-90
-60
-30
0
30
60
90
θ (Deg.)

Fig. 5

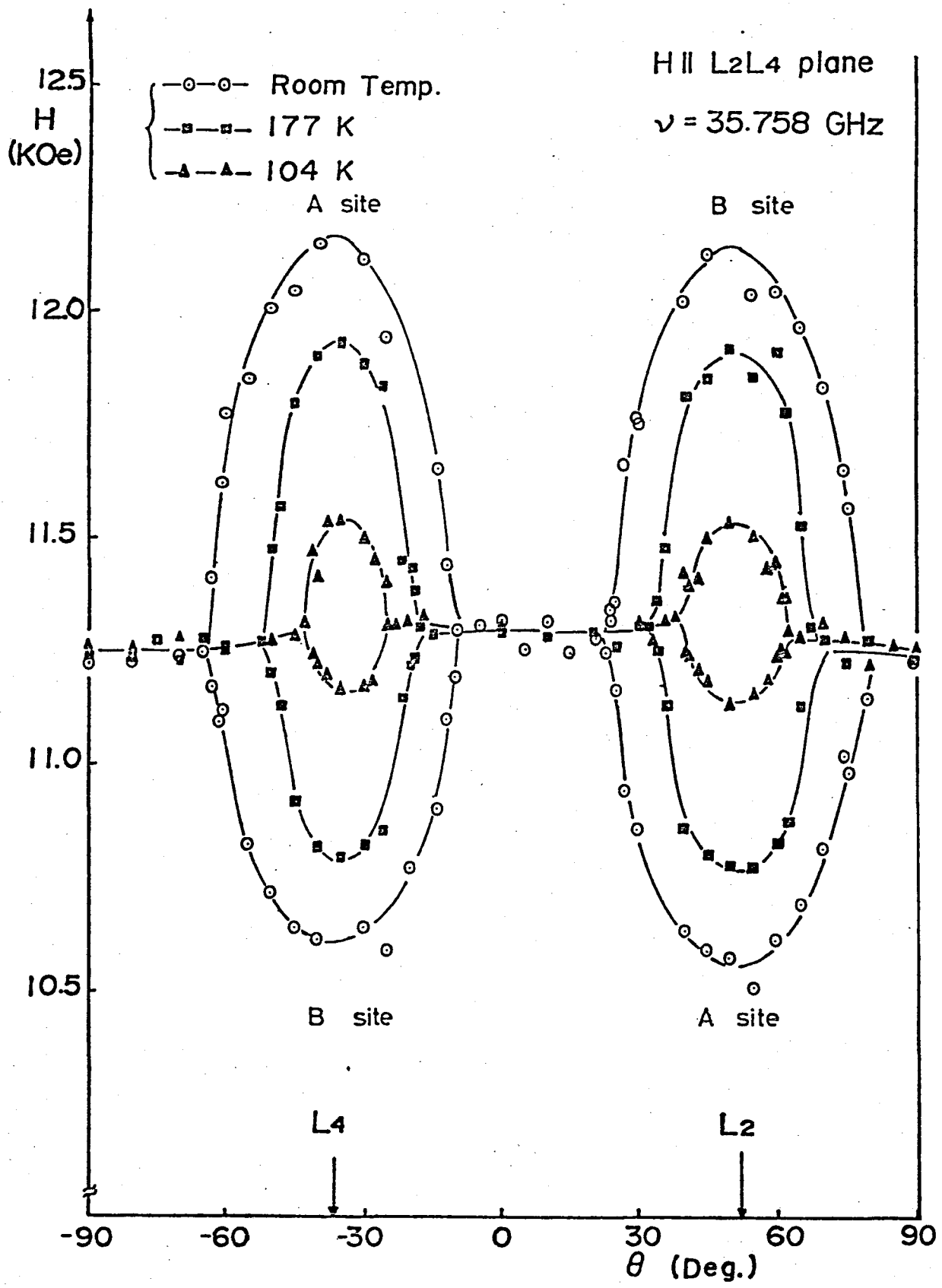
H ll L2L4 plane
ν = 35.758 GHz
Room Temp.
177 K
104 K
H (KOe)
12.5
12.0
11.5
11.0
10.5
A site
B site
B site
A site
L4
L2
-90
-60
-30
0
30
60
90
θ (Deg.)

Fig. 6

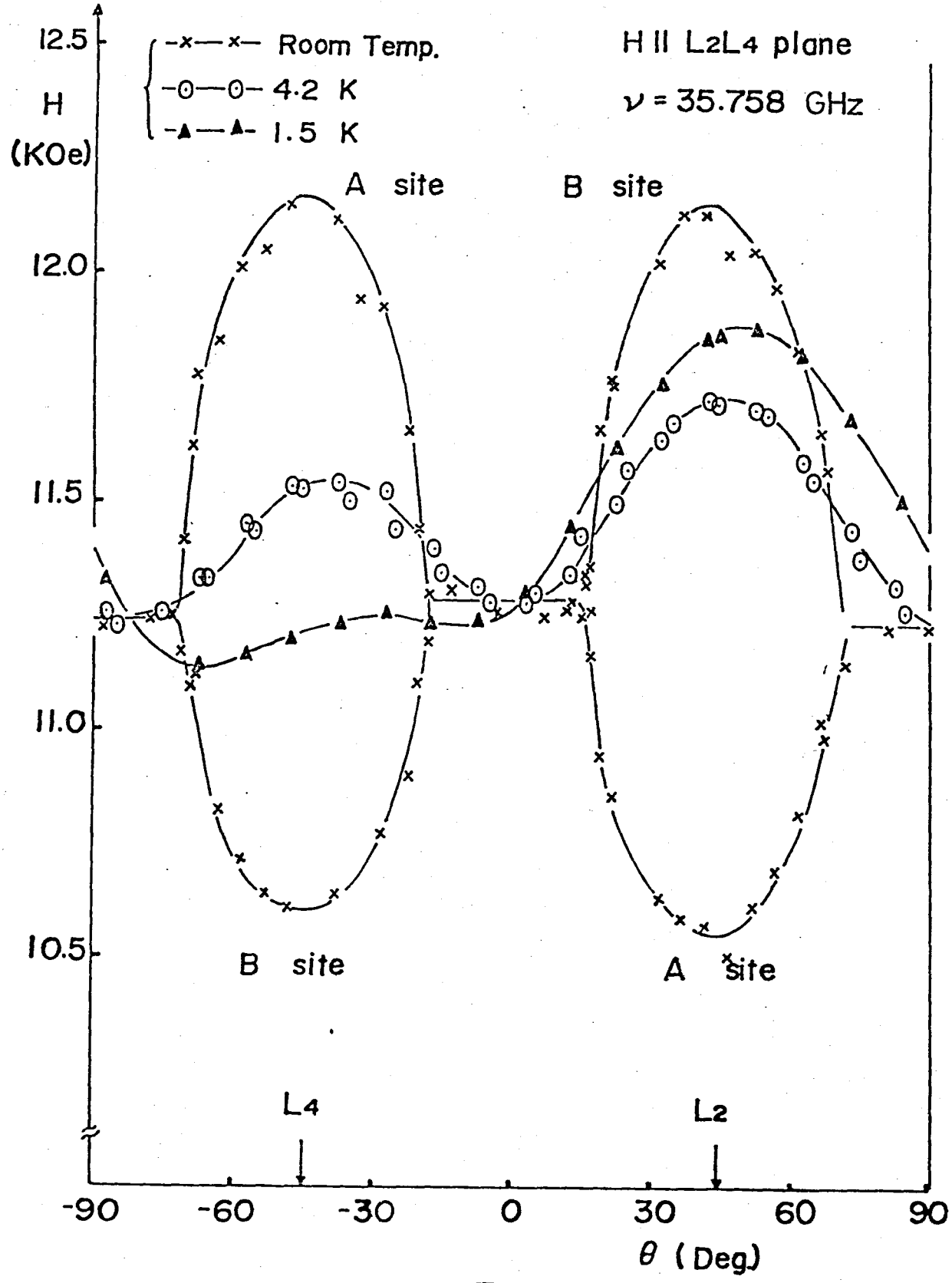
12.5
H
(KOe)
12.0
11.5
11.0
10.5
-x—x- Room Temp.
-o—o- 4.2 K
-▲—▲- 1.5 K
H II L2L4 plane
ν = 35.758 GHz
A site
B site
B site
A site
L4
L2
-90
-60
-30
0
30
60
90
θ (Deg)

Fig.7

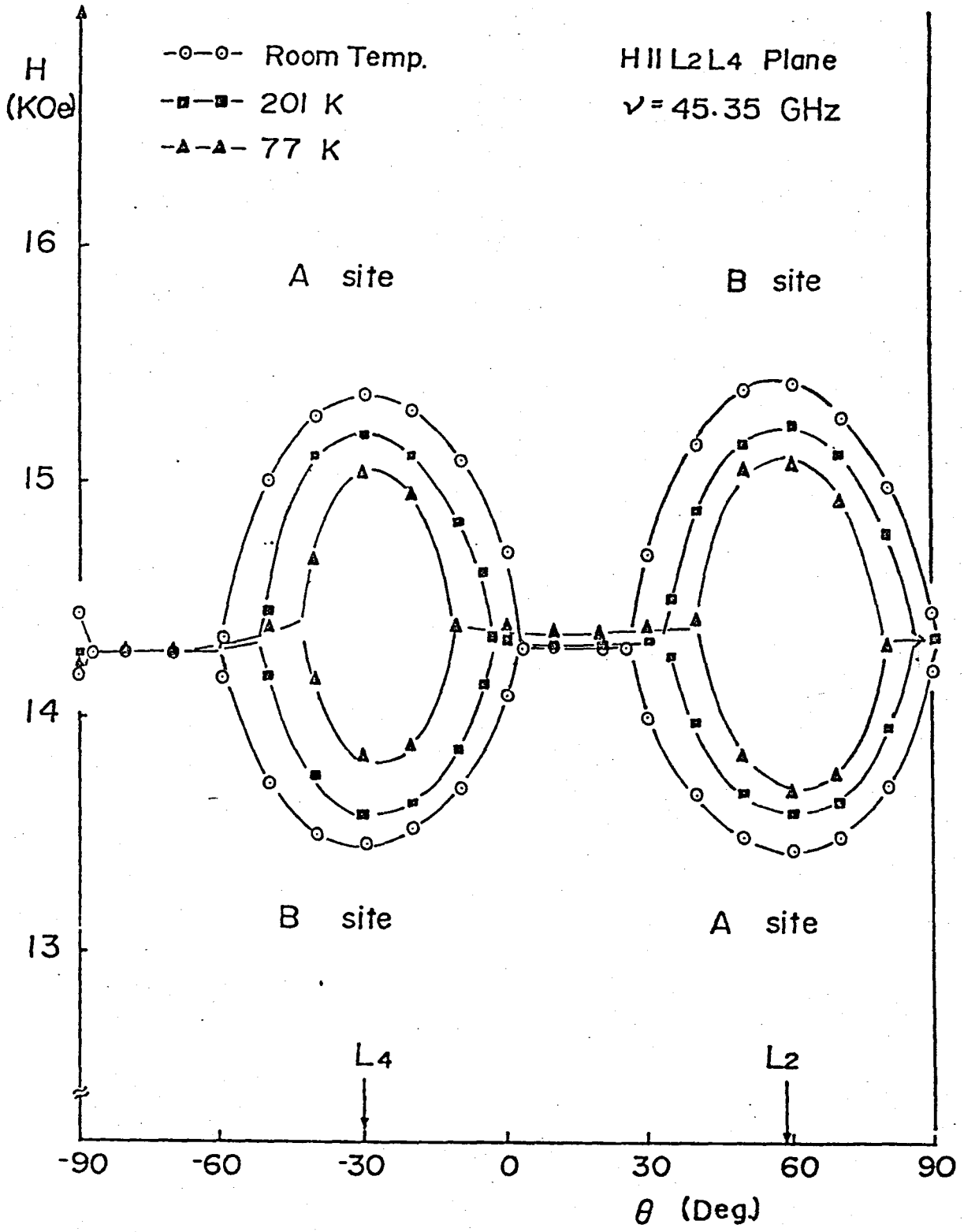
H
(KOe)
-o-o- Room Temp.
-■-■- 201 K
-▲-▲- 77 K
H II L2 L4 Plane
ν = 45.35 GHz
16
15
14
13
A site
B site
B site
A site
L4
L2
-90
-60
-30
0
30
60
90
θ (Deg)

Fig. 8

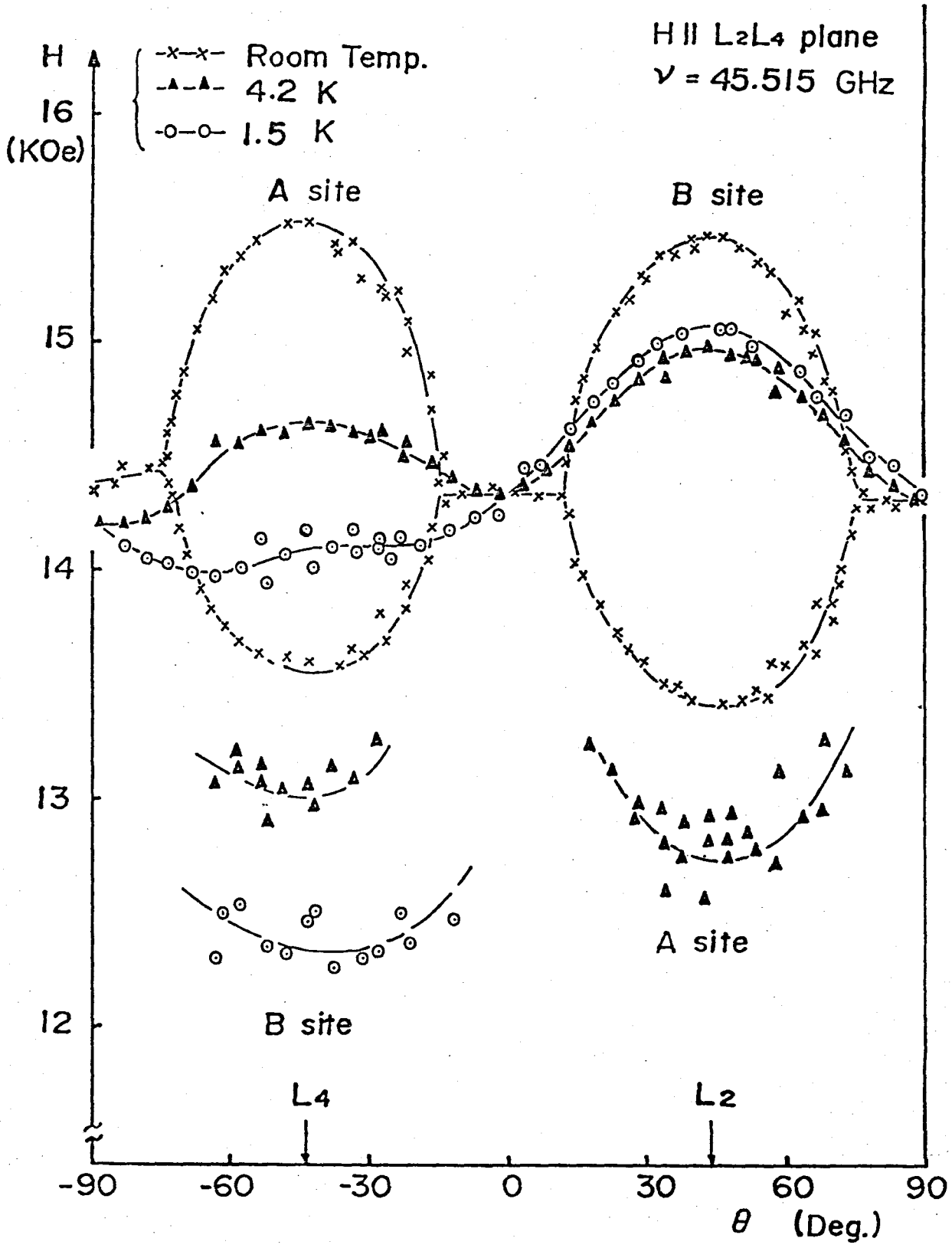
H
16
(KOe)
15
14
13
12
-×-×- Room Temp.
-▲-▲- 4.2 K
-o-o- 1.5 K
H ll L2L4 plane
ν = 45.515 GHz
A site
B site
A site
B site
L4
L2
-90
-60
-30
0
30
60
90
θ (Deg.)

Fig.9

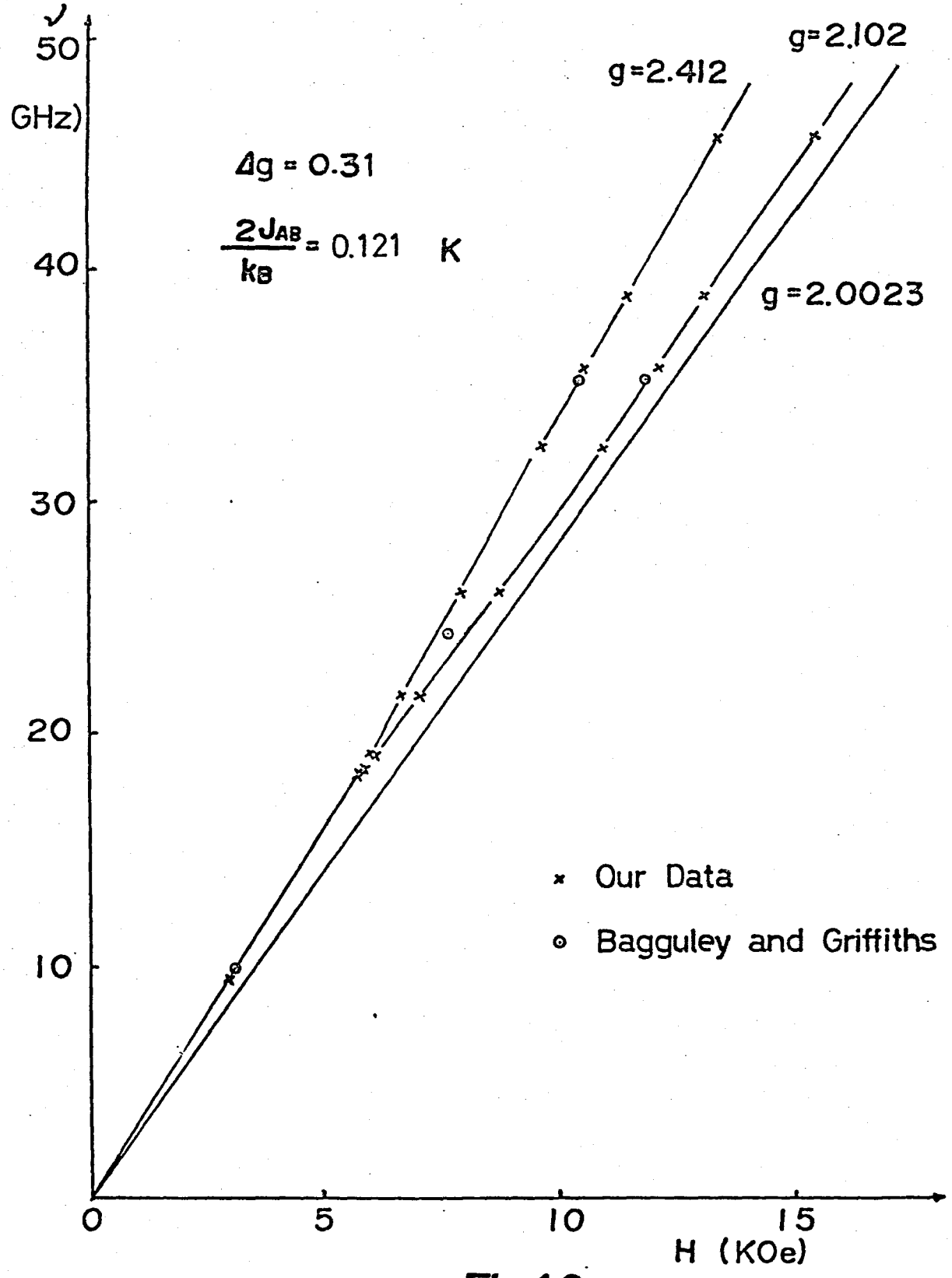
ν
50
GHz)
40
30
20
10
0
5
10
15
H (KOe)
g=2.412
g=2.102
g=2.0023
Δg = 0.31
2JAB/kB = 0.121 K
× Our Data
⊙ Bagguley and Griffiths

Fig.10

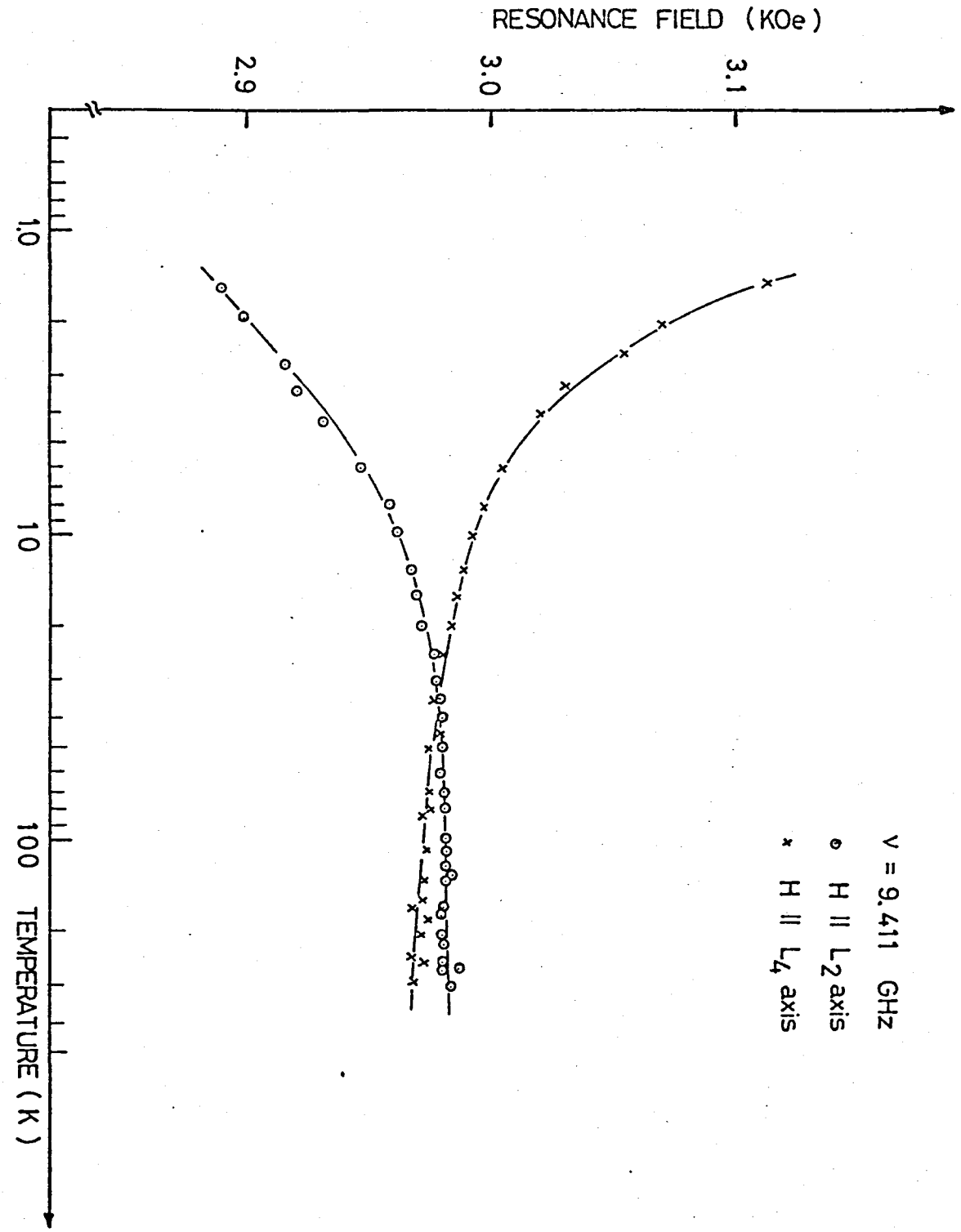
RESONANCE FIELD (KOe)
2.9
3.0
3.1
1.0
10
100
TEMPERATURE (K)
ν = 9.411 GHz
o H // L2 axis
x H // L4 axis

Fig.11

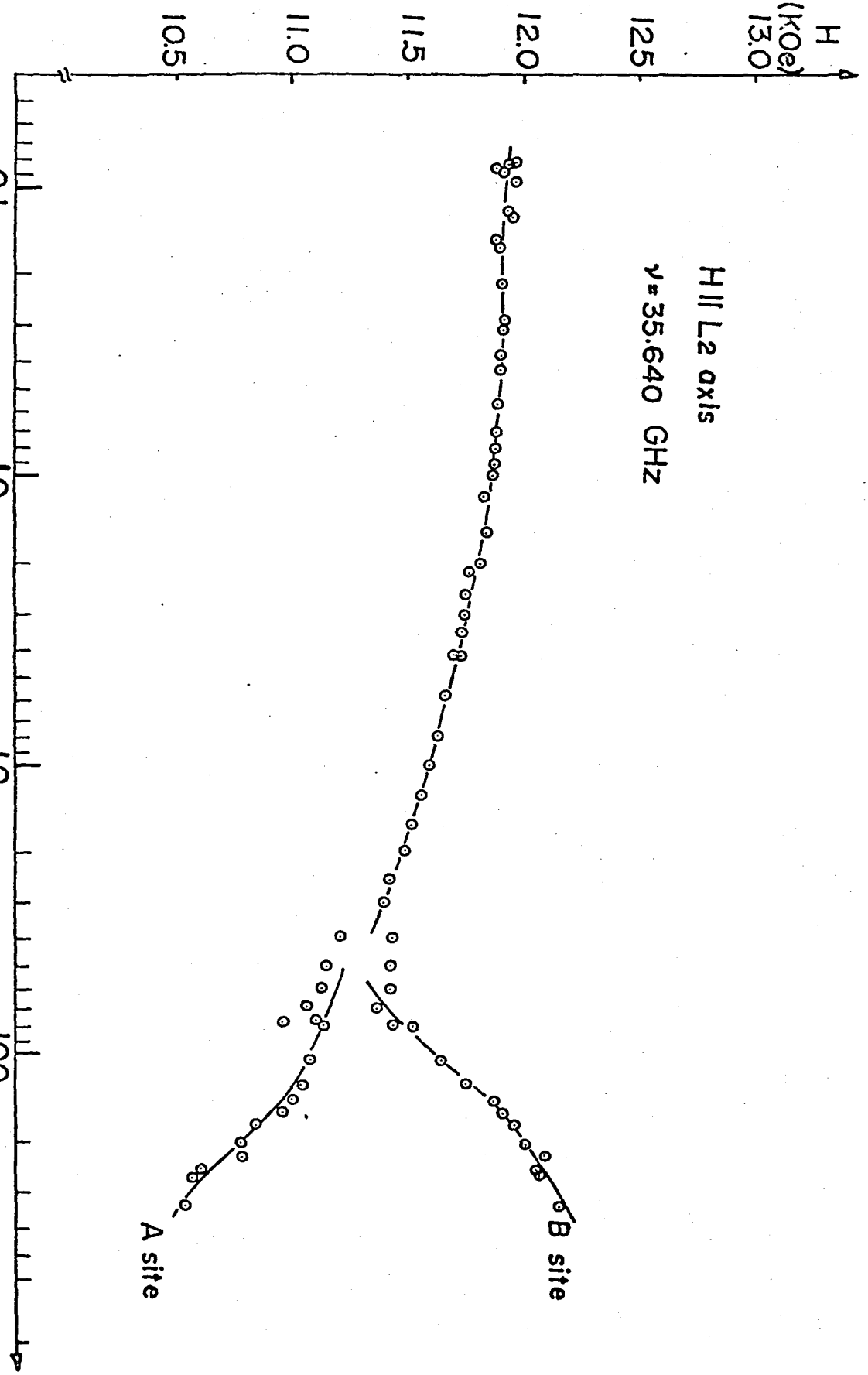
H (KOe)
13.0
12.5
12.0
11.5
11.0
10.5
H // L2 axis
ν = 35.640 GHz
A site
B site
0.1
1.0
10
100
Temperature (K)

Fig.12

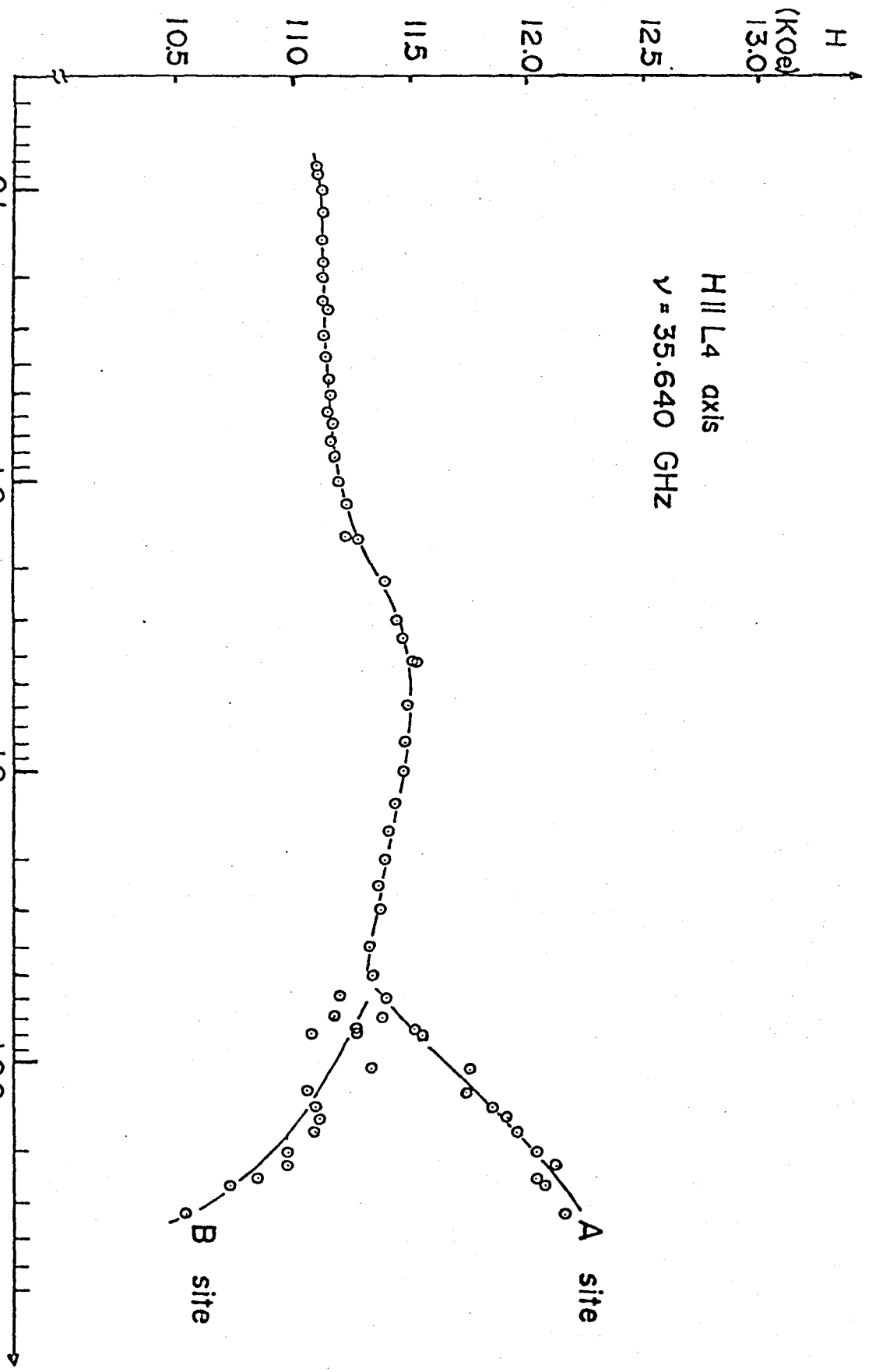
H
(KOe)
13.0
12.5
12.0
11.5
11.0
10.5
H ⊥ L4 axis
ν = 35.640 GHz
A site
B site
0.1
1.0
10
100
Temperature (K)

Fig.13

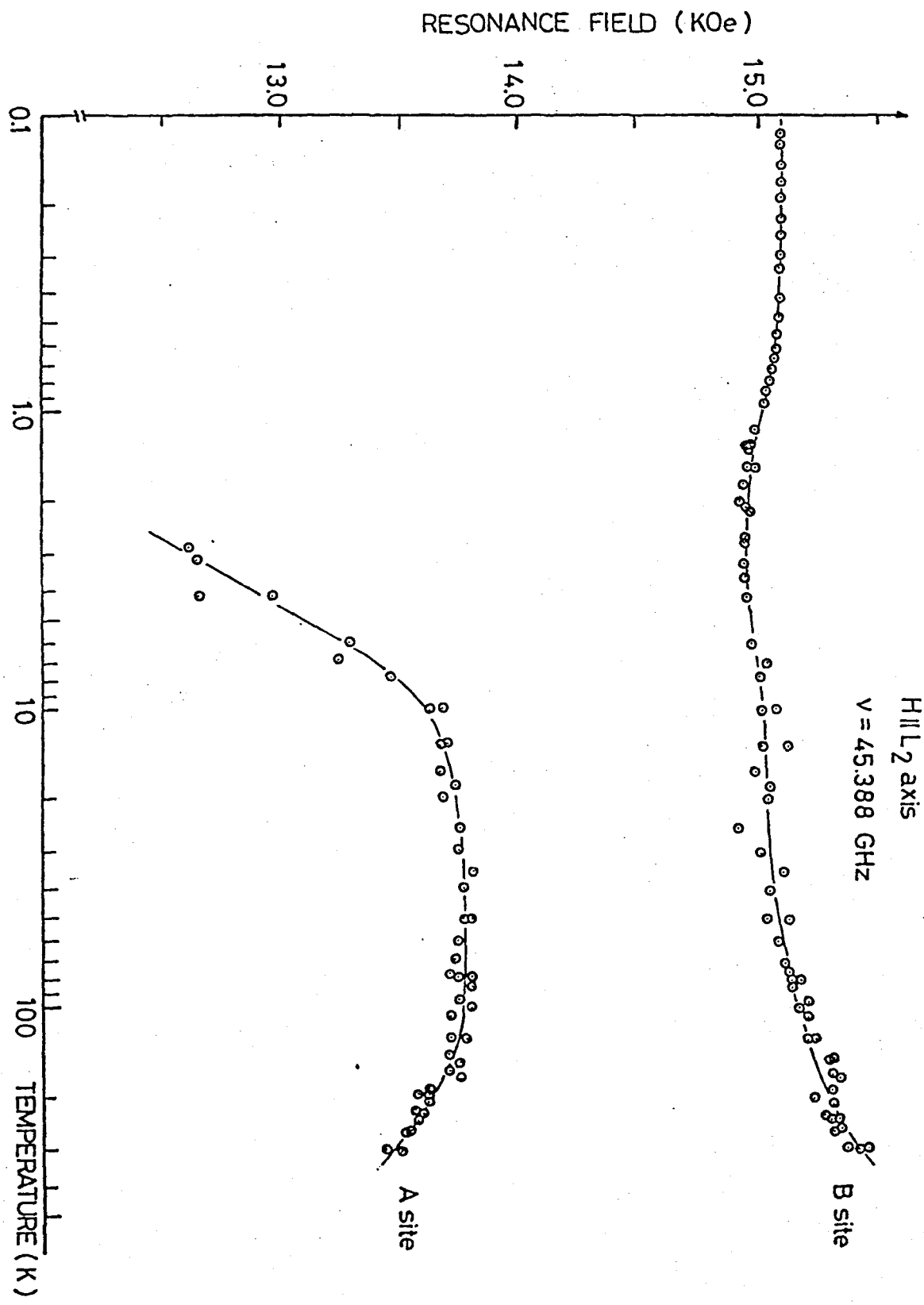
RESONANCE FIELD (KOe)
15.0
14.0
13.0
0.1
1.0
10
100
TEMPERATURE (K)
H // L2 axis
ν = 45.388 GHz
B site
A site

Fig.14

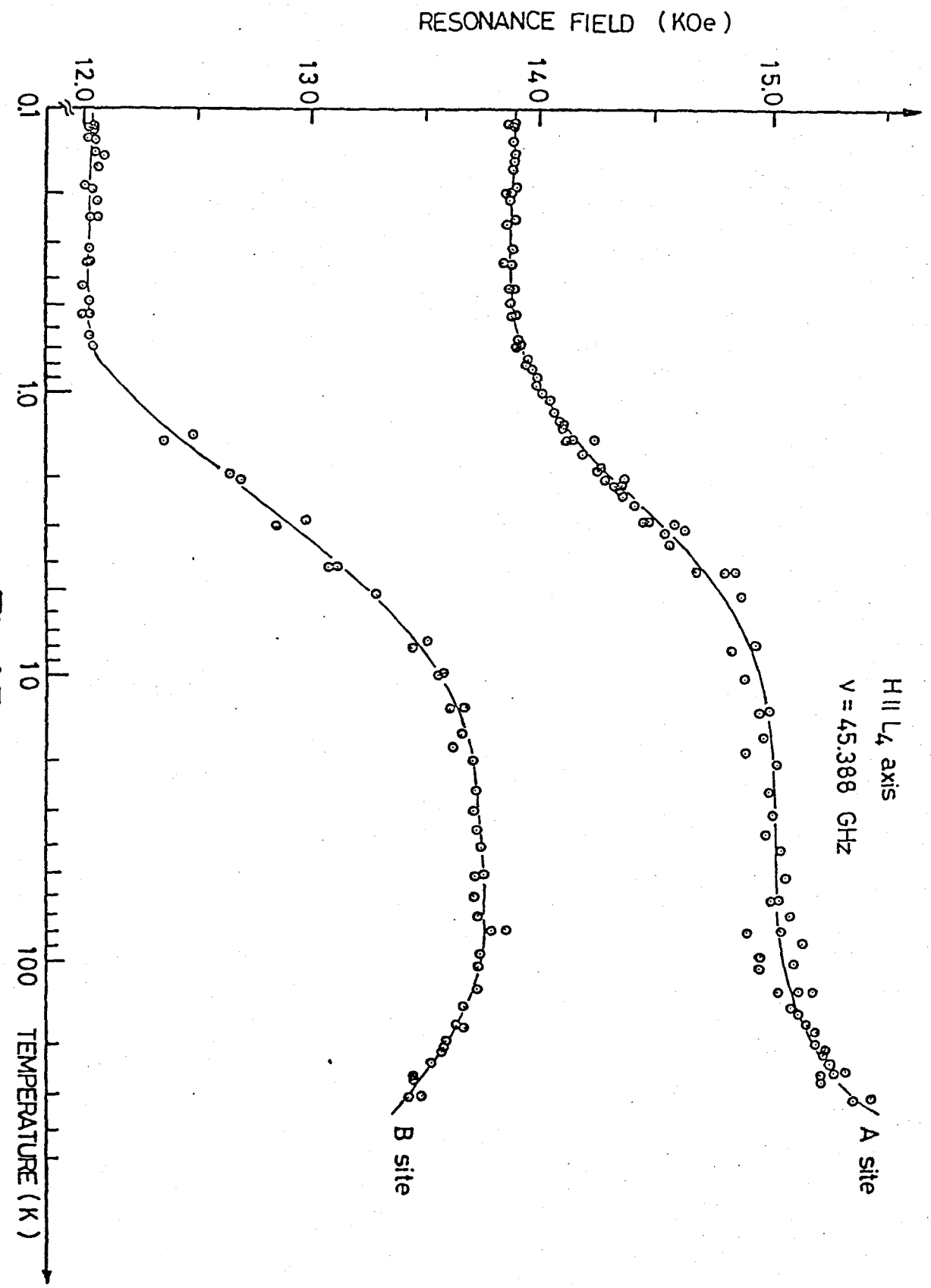
RESONANCE FIELD (KOe)
12.0
13.0
14.0
15.0
0.1
1.0
10
100
TEMPERATURE (K)
H ⊥ L4 axis
ν = 45.388 GHz
A site
B site

Fig.15

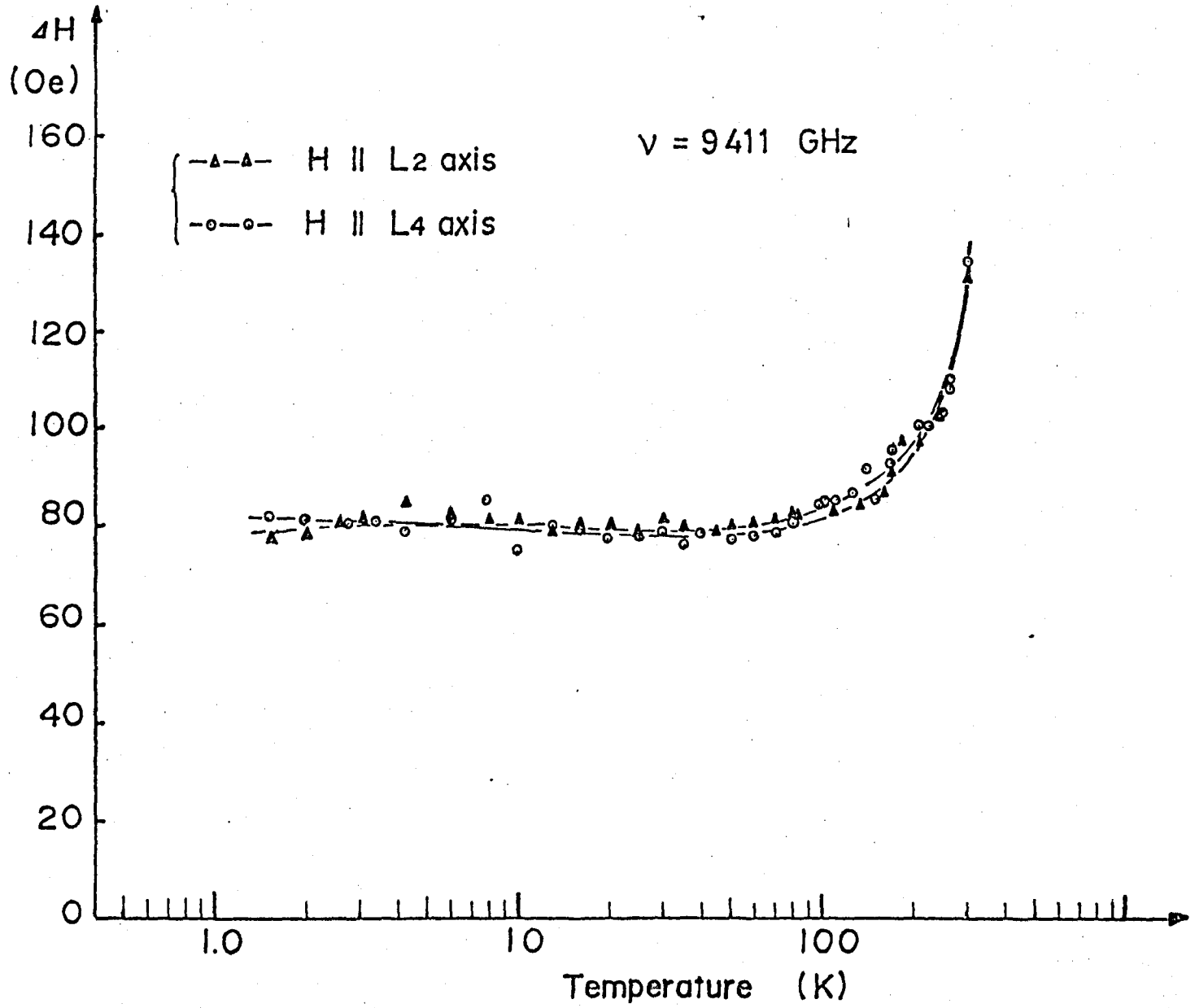
ΔH
(Oe)
160
140
120
100
80
60
40
20
0
H ∥ L2 axis
H ∥ L4 axis
ν = 9411 GHz
1.0
10
100
Temperature (K)

Fig.16

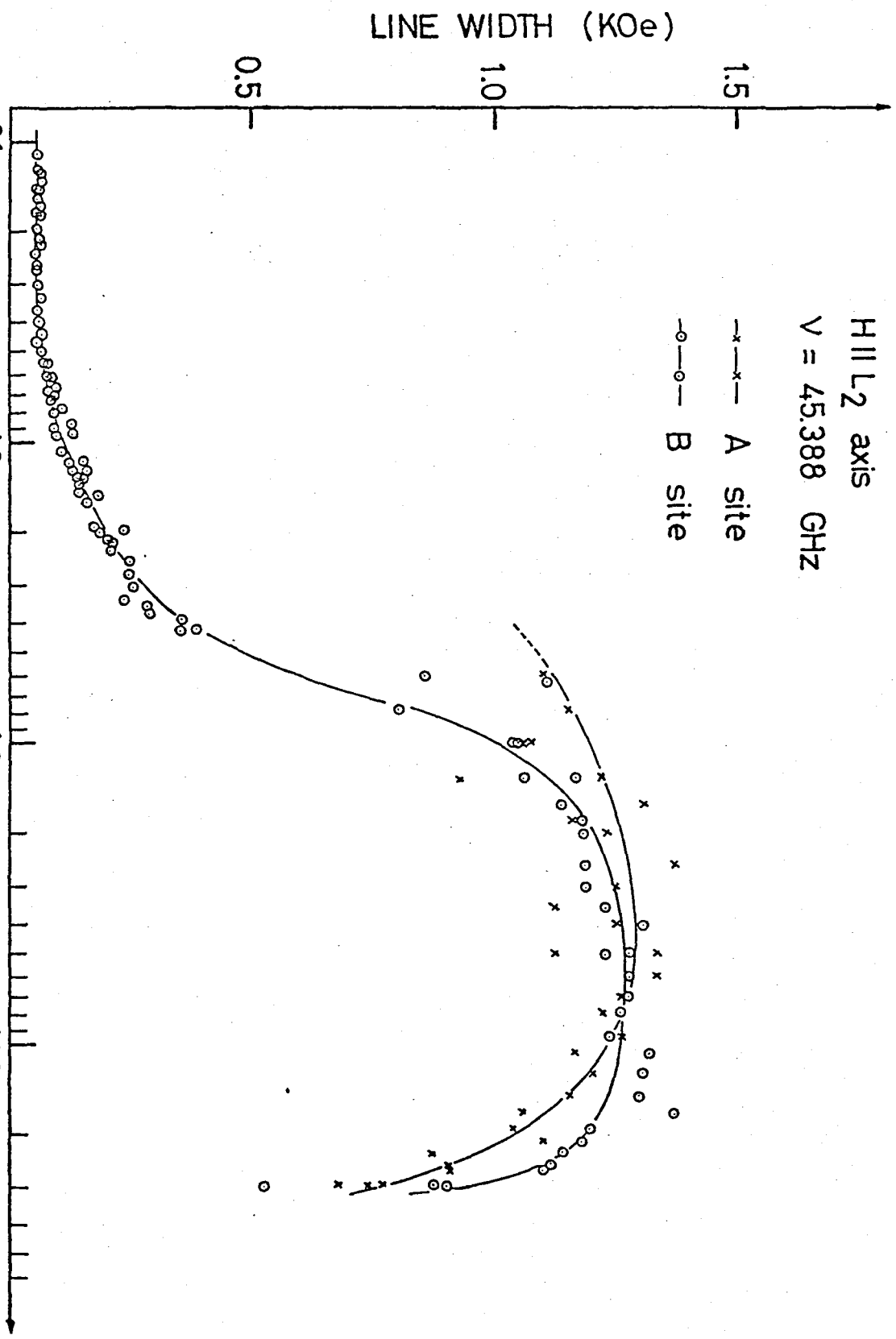
LINE WIDTH (KOe)
0.5
1.0
1.5
0.1
1.0
10
100
TEMPERATURE (K)
H ⊥ L2 axis
V = 45.388 GHz
A site
B site

Fig.17

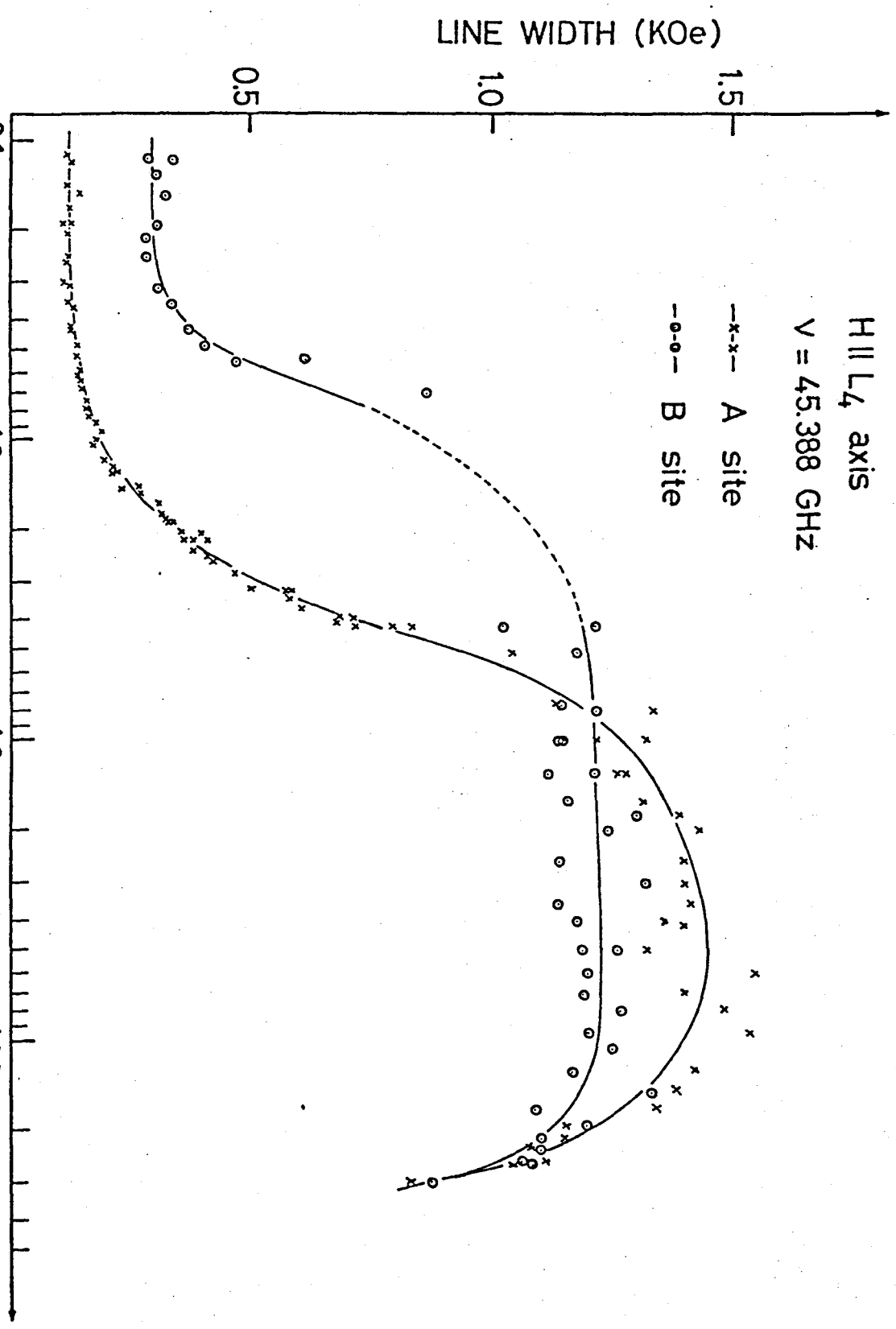
LINE WIDTH (KOe)
0.5
1.0
1.5
0.1
1.0
10
100
TEMPERATURE (K)
H ⊥ L4 axis
ν = 45.388 GHz
-x-x- A site
-o-o- B site

Fig.18

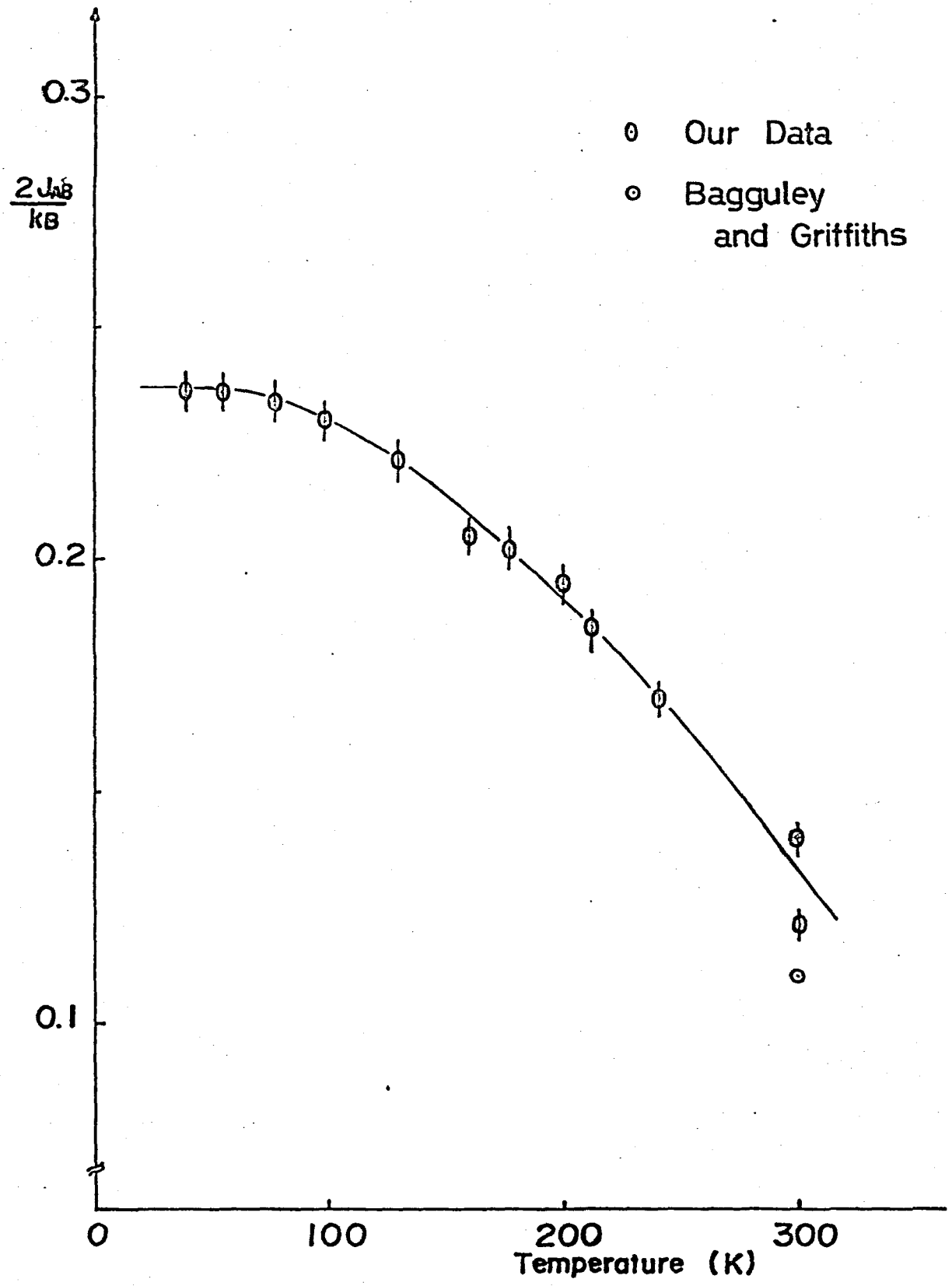
0.3
0.2
0.1
2JnB/kB
Our Data
Bagguley and Griffiths
0
100
200
300
Temperature (K)

Fig.19

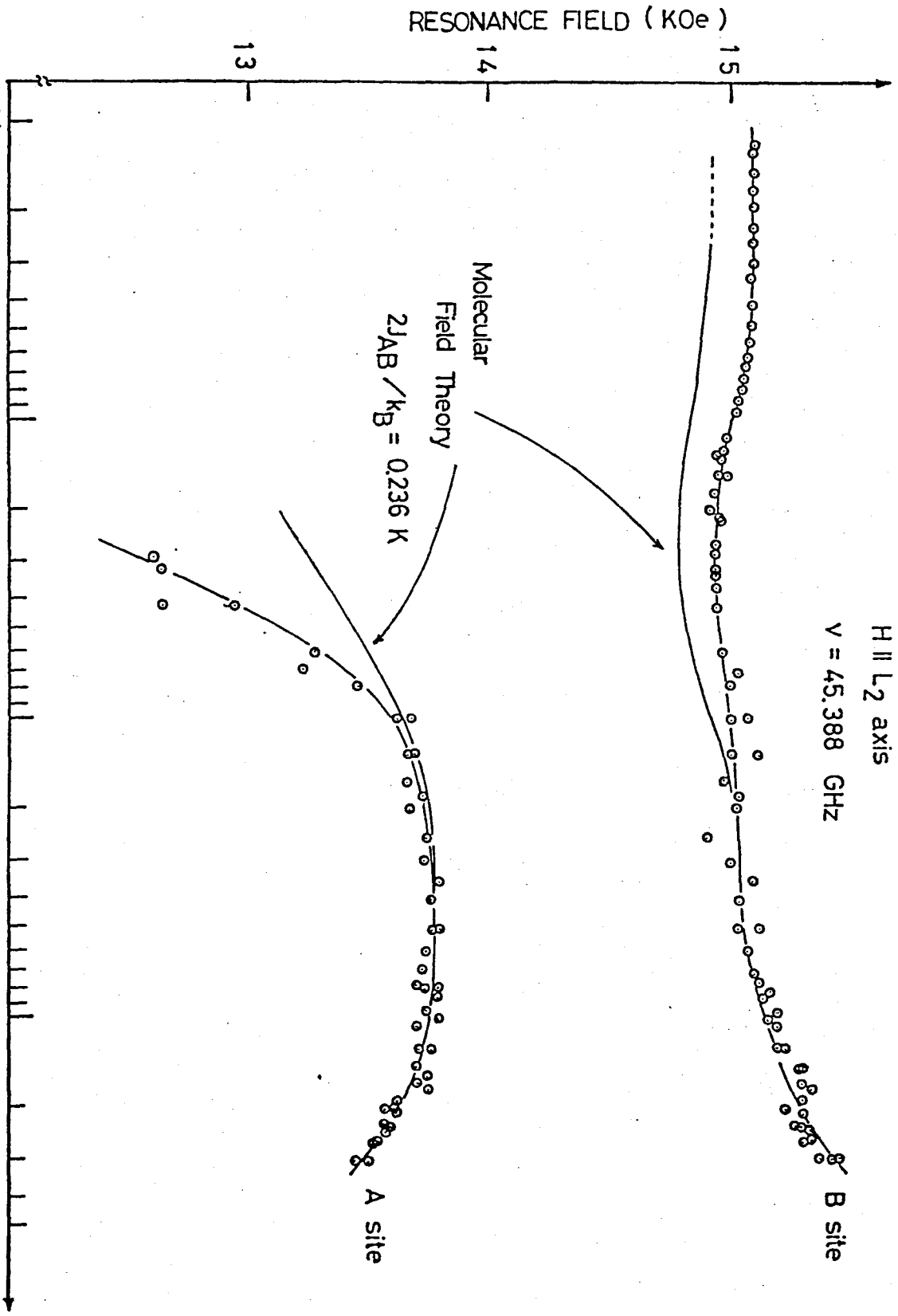
RESONANCE FIELD (KOe)
13
14
15
0.1
1.0
10
100 TEMPERATURE (K)
H ⊥ L2 axis
ν = 45.388 GHz
B site
A site
Molecular
Field Theory
2JAB / kB = 0.236 K

Fig. 20

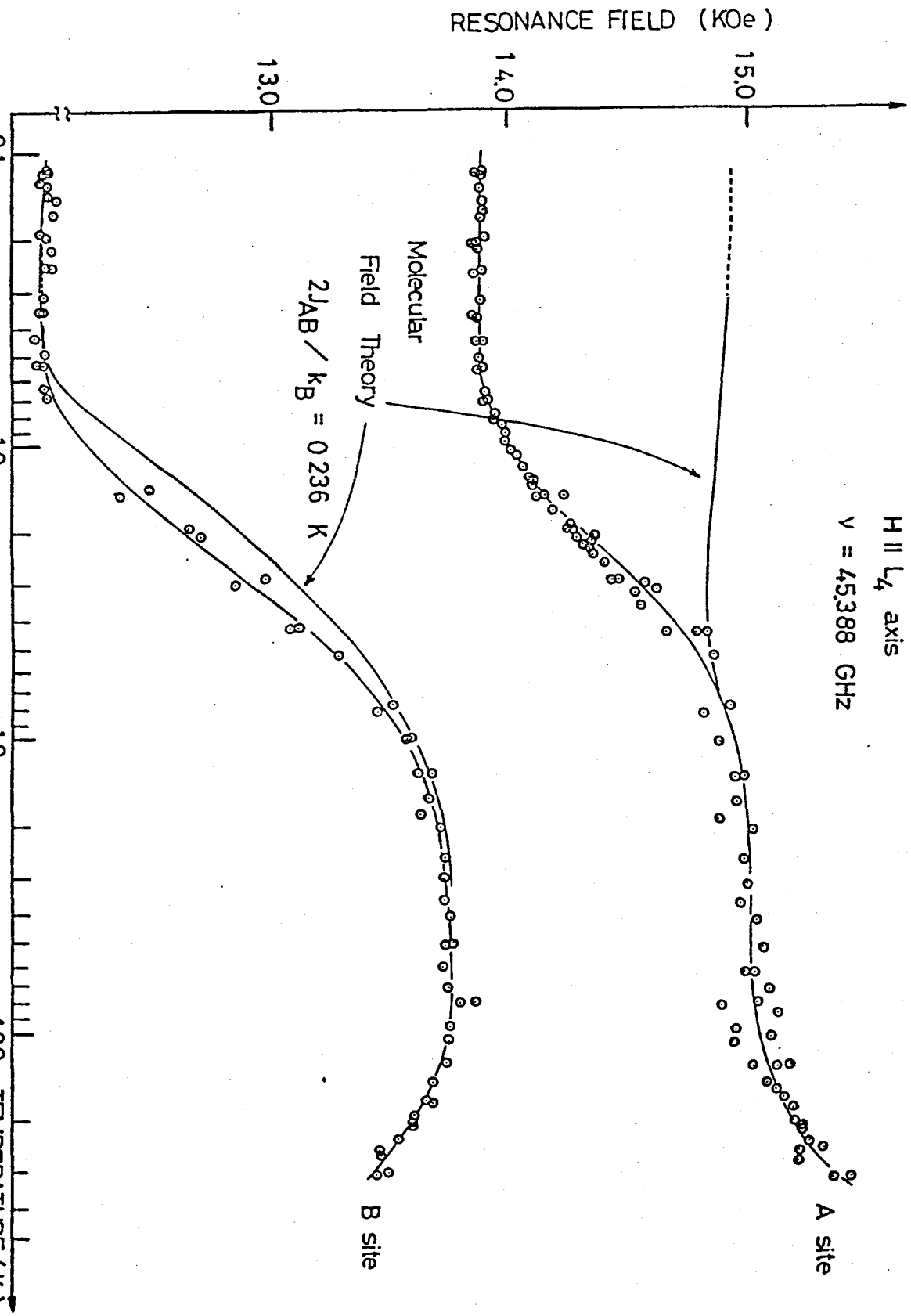
RESONANCE FIELD (KOe)
15.0
14.0
13.0
H ∥ L4 axis
ν = 45.388 GHz
A site
B site
Molecular
Field Theory
2JAB / kB = 0.236 K
0.1
1.0
10
100 TEMPERATURE (K)

Fig.21

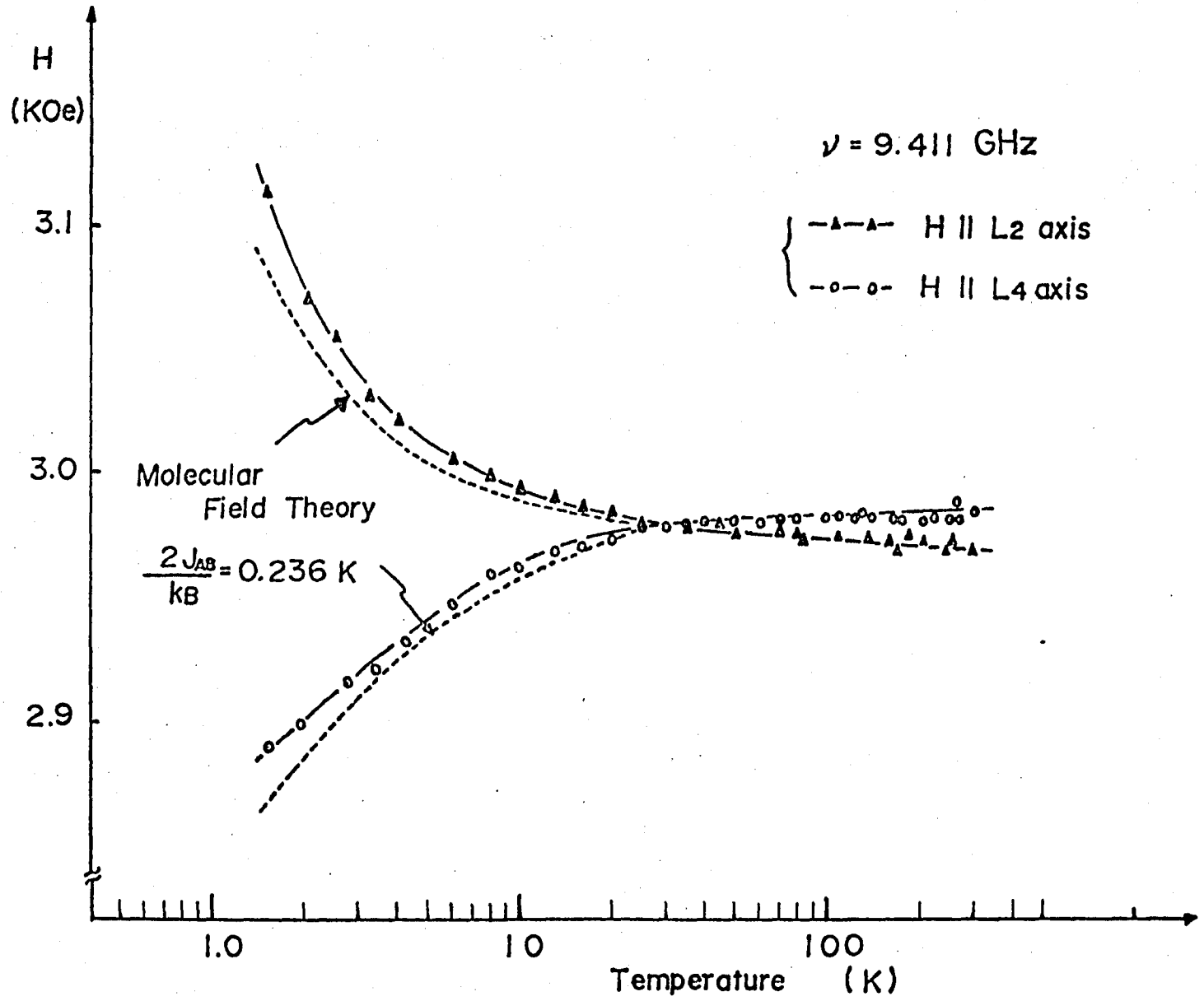
H
(KOe)
3.1
3.0
2.9
ν = 9.411 GHz
H ll L2 axis
H ll L4 axis
Molecular
Field Theory
2 JAB / kB = 0.236 K
1.0
10
100
Temperature (K)

Fig.22

Part III

Magnetic and Superconducting Phase Transitions in $Er_cY_{1-c}Rh_4B_4$

Synopsis

In magnetoresistance measurements in $Er_cY_{1-c}Rh_4B_4$ from its superconducting transition temperature T_{c1} to 80 mK, the T_{c1} and the reentering temperature T_{c2} were determined as a function of the concentration of Er. Comparing our results with the recent theory of Maekawa et al., the exchange interaction J' among local spins and I between local spins and superconducting electrons were estimated as $J' \simeq 0.3$ K and $I^2N(0) \simeq 0.046$ K, where N(0) is the density of state. A sudden decrease of H_{c2} at T_{c2} suggesting the first order transition was observed in a high concentration region.

In magnetization measurements from 4.2 K to 0.5 K up to 29 kOe, an anomalous temperature dependence of magnetization suggesting the presence of a new phase predicted by the theory was found in $ErRh_4B_4$ in narrow temperature region between 1.0 K and about 1.4 K in low fields $H \simeq 0 \sim 400$ Oe.

§ 1 Introduction

Since the discovery of the re-entrant superconductivity in the ternary compounds $(RE)Rh_4B_4$ by Fertig et al.[1] and in the ternary Chevrel-phase compounds $(RE)_xMo_6S_8$ and $(RE)_xMo_6Se_8$ ($x = 1.0 \sim 1.2$) by Ishikawa et al.[2], where (RE) means a rare earth element, there have been growing interest on superconductivity and magnetic properties in these compounds containing a rare earth ion with localized moment. Generally speaking, in the case of impurity spins in superconductors the fluctuation of local spins inside a superconductor acts on a Cooper pair as a pair-breaker, therefore, weakens the BCS coupling. So the T_{c1} usually strongly depends on the concentration of impurity spins. However, one of the surprising features of our superconductors is an extreemly weak depression of T_{c1} in spite of the presence of localized magnetic moment. Recently, the theoretical formulations of these problems for superconducting and magnetic transition temperatures in the rare earth ternary superconductors were presented by Maekawa and tachiki[3] as functions of the intra- and interatomic exchange interactions and the concentration of local spins. To verify their theory, it is desired to investigate the dependence of T_c and T_M on the concentration of local spins.

Another surprising feature in these ternary compounds is the coexistence of superconductivity and magnetic long range order. Up to the present, the coexistence of superconductivity and antiferromagnetic order on Chevrel-phase compounds $(RE)_{1.2}Mo_6S_8$ for RE = Gd, Dy and Tb was comfirmed by neutron scattering experiments.[4),5),6)] In addition to these compounds, the coexistence have

been inferred in $Er_{1.2}Mo_6S_8$[7], and the same kinds of selenide compounds[8),9)]. However, no clear experimental evidence have been found for the coexistence of superconductivity and long-range ferromagnetic order. Actually, in a ferromagnetic superconductor $ErRh_4B_4$ which becomes superconducting at T_{c1} = 8.7 K and returns to normal state at $T_{c2} \simeq 0.8$ K[1),10)], heat capacity[1),11),12)] and neutron diffraction experiments[13),14)] have shown that the destruction of superconductivity at T_{c2} is accompanied by the development of long-range ferromagnetic order of magnetic ions. Quite recently, the appearence of helical spin order in ferromagnetic superconductor $ErRh_4B_4$ in the superconducting state just above the ferromagnetic ordering temperature is theoretically expected[15),16),17),18)]. However, this possibility is still controversial. There is no obvious experimental result for verifying the coexistence of the superconductivity and helical spin ordering near T_{c2} except for the suggestive neutron scattering data[13),14).19)]. To investigate this possibility we have precisely measured the magnetization of $ErRh_4B_4$ around T_{c2} by using newly developed fluxgate magnetometer. The concentration dependence of T_{c1} and T_{c2} and the temperature and concentration dependence of the upper critical field H_{c2} in $Er_cY_{1-c}Rh_4B_4$ are also measured.

§ 2 Crystal and Electronic Structure

X-ray diffraction experiment of $(RE)Rh_4B_4$ was performed by Vandenberg et al.[20] as a series of investigation of crystal structures of ternary rhodium borides. The compounds $(RE)Rh_4B_4$ with RE = Y, Nd, Sm, Gd, Tb, Dy, Ho, Er, Tm, Lu and Th have the same crystal structure with body-centered tetragonal lattice and space group $P4_2/nmc$ which is shown in Fig. 1. However, some elements such as Sc, La, Ce, Pr, Eu and Yb do not form $(RE)Rh_4B_4$ compounds. Th, Y, Nd, Sm, Er, Tm and Lu form superconducting compounds while Gd, Tb, Dy and Ho yield ferromagnetic phase with no superconductivity. Their superconducting transition temperatures are by far the highest yet observed for any borides. This superconducting behavior is in sharp contrast to that previously found for the ternary Chevrel-phase compounds $(RE)_xMo_6S_8$[21] and $(RE)Mo_6Se_8$[22], where $x = 1.0 \sim 1.2$. Every rare earth compound has been to form a Chevrel-phase sulphide and selenide with the exception of the Ce and Eu compounds, and they are all superconducting.

A comparison of electronic and magnetic properties in the series of these ternary rhodium boride compounds in particularly interesting. Though any obvious differences in the crystal and magnetic structures can not be found in the series of these compounds, quite different electronic and magnetic properties appears. The a/c ratio is almost constant in all these compounds and the value of the effective moment μ_{eff} does not show any anomalous behavior. The series of these compounds can be clearly divided to two groups, i. e., Gd, Tb, Dy and Ho group with ferromagnetic

and no superconducting phase, and Er, Tm and Lu group with superconducting phase. Especially, there exist a clear difference between the neighboring rare earth ions Ho and Er. $HoRh_4B_4$[23] is ferromagnetic below 6.5 K while $ErRh_4B_4$ shows the superconducting transition at 8.7 K. However, the effective magnetic moments of both rare earth ions are close to each other. It is 10.6 μ_B for Ho and 9.6 μ_B for Er and the difference is only 10 %. This fact suggests that the electronic and magnetic properties of these ternary rhodium boride compounds may strongly be modified by delicate changes in the electronic structure, magnetic interactions and so on. In Chevrel-phase compounds it is experimentally concluded that the superconducting properties are mainly determined by the Mo_6^- clusters and their relative positions[24]. The exchange interactions among 4f local spins are mainly produced by 6s conduction electrons and the contribution coming from 4d electrons, i.e., the superconducting electrons due to Mo_6^- is negligibly small. It is believed that the electronic and magnetic interaction mechanisms of $(RE)Rh_4B_4$ are similar to those of the Chevrel-phase compounds. This picture in ternary rhodium boride compounds $(RE)Rh_4B_4$ was supported by the selfconsistent energy band calculations[25),26),27] and was also adopted to the theory of Maekawa and Tachiki[3].

The relatively weak magnetic interaction between the 4f localized moments by 5d and 6s electron bands of Er atoms leads to a magnetic ordering at T_M. However, once the superconducting state has been realized, the exchange interaction is reduced because of disappearence of polarization of conduction electrons due to the superconductivity.

§ 3 Experimental

(1) Sample Preparation

The sample of $Er_cY_{1-c}Rh_4B_4$ was synthesized from high purity oxide Er_2O_3 (99.9 %) and elements Rh (99.9 %), B (99.8 %) and Y (99.9 %) from Shinetsu Chemical Co. Ltd.. In order to get a high stoichometry, considerable care was taken as follows. The first step is the synthesis of binary compounds MB_4, where M means Er or Y. Generally speaking, the hexaboride MB_6 is more stable compared with MB_2, MB_4 and MB_{12}. In ErB_6, however, it is exceptionally unstable[28]. ErB_4 was made from Er_2O_3 by using the induction heating method according to the reaction given by

$$Er_2O_3 + 10\,B \longrightarrow 2\,ErB_4 + B_2O_3\ (\text{gas}). \qquad (1)$$

The procedure is as follows. Powdered Er_2O_3, which is of pale pink, is mixed with powdered boron. The mixture was pressed by 100 kg/cm^2 in the form of disk (13 mm in diameter and 3 ∿ 5 mm in thickness). The disk was heated by induction furnace in a graphite crucible at about 2000 °C for one hour. The excess boron get off as a gas of B_2O_3 during the chemical reaction. Other compounds, ErB_2 and ErB_{12} were not found in our disk. Synthesized ErB_4 is gray. YB_4 was made by conventional arc-melting method. When induction method was used, it was difficult to make a single phase of YB_4. The reason is not yet clear. Probably the cooling speed in the arc-melting method is faster than that of the induction method and YB_2 or YB_6 can not be produced under the rapid cooling procedure. The reaction is thus simply explained according to

the following as

$$Y + 4\ B \longrightarrow YB_4 \qquad (2)$$

This tetraboride is gray. and can easily distinguish from hexaboride which is blue. As the second step, the ternary compounds MRh_4B_4 were prepared by induction or arc-melting of two constituents MB_4 and Rh under 1/3 atmospheric pressure of Ar according to the following reaction formula as

$$MB_4 + 4\ Rh \longrightarrow MRh_4B_4 \qquad (M = Er \text{ or } Y) \qquad (3)$$

The synthesized sample of MRh_4B_4 was confirmed by X-ray diffraction. In the final step, $Er_cY_{1-c}Rh_4B_4$ and YRh_4B_4 were synthesized by arc-melting with appropriate mixture of $ErRh_4B_4$ and YRh_4B_4.

The annealing were done at 1050 °C for one week and an X-ray analysis was done to check the crystal structure. The X-ray analysis also shows that a weak trace of RhB phase remaines in addition to the tetragonal $Er_cY_{1-c}Rh_4B_4$ phase. The impurity phase is almost independent of the heat treatments and the concentration of Er.

The concentration of Er was determined by X-ray flourescence method. As the results, the concentration c of 13 kinds of ternary borides were produced with c = 0.00, 0.13, 0.17, 0.26, 0.29, 0.44, 0.53, 0.65, 0.71, 0.72, 0.82, 0.88 and 1.00.

(2) Experimental Procedure

The measurements of dc electrical resistance of $Er_cY_{1-c}Rh_4B_4$ was done using adiabatic demagnetization refrigerator combined to ^3He stage from 4.2 K down to 80 mK. Above 4.2 K the conventional cryostat was used. Superconducting transition temperature T_{c1} and the reentrant temperature T_{c2} were determined by measuring the magnetoresistance using conventional four-probe method. The sample was cut by spark cutter in the form of about 0.5 mm × 0.5 mm × 1 cm and copper wires of 0.05 mm in diameter were spot welded on to the sample. The data below 1 K were taken with increasing temperature only. The current used in the present resistance measurements was 1 mA for all cases. The fluxflow resistance which usually appears in large current measurements was negligible in the present small current measurement.

Two kinds of magnetization measurements were done by the fluxgate magnetometer method using two kinds of ^3He cryostats down to about 0.5 K. One of the measurements is due to the extracting sample method and the other one is the temperature variation method under a fixed magnetic field. The magnetic field is always supplied parallel to the long dimension of the sample. Absolute value of the magnetization was calibrated by comparing with the static measurements with the same sample by the Faraday method. The characteristics of these apparatus are described in B in Part (I) in detail.

§ 4 Results and Discussions

(1) Magnetoresistance Measurements

The magnetoresistance curves were taken in the temperature range from 80 mK up to T_{c1} for a whole concentration region in $Er_cY_{1-c}Rh_4B_4$. Typical examples at 80 mK are shown for c = 1.00, 0.44 and 0.17 in Fig. 2. The virgin curve for c = 0.44 rises abruptly at a threshold field H_s of about 2 kOe, and reaches a normal resistance at about 4 kOe. For decreasing field the curve does not follow the virgin curve but gives a finite resistance value at zero field. After that, the magnetoresistance curve follows the initial decreasing field curve with field up and down as shown by double arrows in Fig. 2. Similar virgin behavior was observed in a concentration region c = 0.44 $\sim$ 0.65, where the threshold field H_s decreased with increasing the concentration. No such virgin curve was observed in high (c = 0.70 $\sim$ 1.00) and low (c = 0.00 $\sim$ 0.40) concentration regions. Instead, only a reversible curve was observed for the field up and down as is shown in Fig. 2. The cause for the peculiar virgin behavior in the region c = 0.44 $\sim$ 0.65 might be that below T_M an inhomogeneous superconducting phase remains, because of the closeness to the critical concentration C_c = 0.43 for long-range magnetic order as is shown below. This inhomogeneous superconducting phase disappears after the initial increasing field. The temperature dependence of the magnetoresistance curve was taken for all concentrations and an example for c = 0.44 is shown in Fig. 3. The resistance value at zero field falls to zero at 0.11 K and a hysteresis curve was observed up to about 0.5 K. Hereafter, we define the

temperature at which the zero field resistance in non-virgin state falls to zero as the lower critical temperature T_{c2}, and the temperature at which it returns to the normal value at high temperature as T_{c1}. The hysteresis curves were observed in a narrow temperature region above T_{c2} for the concentrations c = 0.44 ∿ 1.00.

The temperature dependences of electrical resistance at various magnetic fields are also shown in Fig. 4 for c = 1.00, 0.44 and 0.17 as the typical examples. The destruction of superconductivity at T_{c2} at zero field for c = 1.00 is relatively sharp with appreciable hysteresis. Fertig et al[1]. found a small peak near T_{c2} but it was not observed in our data.

The obtained concentration dependences of T_{c1} and T_{c2} are shown in Fig. 5. Open and black circles denote T_{c1} and T_{c2}, respectively. The present results of T_{c1} = 8.7 K and T_{c2} = 0.79 K in $ErRh_4B_4$ are in agreement with the results of Matthias et al.[1), 10)]. They showed that the transition at T_{c2} in $ErRh_4B_4$ found from the magnetoresistance coincides with the onset of long-range magnetic order of Er sublattice. So we assume that the temperature T_{c2} coincides with the magnetic ordering temperature T_M in a whole concentration region in $Er_cY_{1-c}Rh_4B_4$. The concentration dependence of T_M in the present system is given by Oguchi's theory[29)] in a magnetically diluted system as[3)]

$$T_M/J' = 2/\ln\{z'/(z'-4)\}, \qquad (4)$$

where J′ is the nearest neighbor exchange interaction among Er spins and z′ is the reduced concentration defined by z′ = 1 +

$7c\{1-(1-c)^8\}$. By best fitting eq. (4) with the observed concentration dependence in T_{c2}, the value of J' was estimated as $J' \simeq 0.30$ K, and the theoretical line was calculated as shown by the dashed line in Fig. 5. The observed T_{c2} shows good agreement with the theoretical line of T_M and suggests a critical concentration of $C_c \simeq 0.43$ for the long range magnetic order. The concentration dependence of T_{c1} reduced by the transition temperature T_{c0} without magnetic spins is given by Maekawa and Tachiki[3] as

$$T_{c1}/T_{c0} = \exp[1/g_{BCS}N(0) - 1/\{g_{BCS}N(0) - \frac{6I^2N(0)Co'}{T_{c1}} \frac{1}{f_2} \ln(1+\frac{f_2}{f_1})\}], \quad (5)$$

where g_{BCS} and I are the BCS interaction parameter and the exchange interaction between local spins and superconducting electrons, respectively. $N(0)$ is the density of state and Co' is the reduced concentration defined by $Co' = c\{1-(1-c)^8\}\frac{1}{3}S(S+1)$. f_1 and f_2 are functions of T_{c1}, J' and concentration c[3]. These parameters are given by Maekawa and Tachiki[3]. Their theory is applicable in high concentration region. So we tried a quantitative comparison of eq. (5) with our experimental results in high concentration regions. The parameter $I^2N(0)$ in eq. (5) is the most decisive factor for determining the increaseing rate in T_{c1} when the concentration c decreases from c = 1. By best fitting eq. (5) with our results in a high concentration region, the value of $I^2N(0)$ was determined as 0.046 K. The other parameters were taken as T_{c0} = 10 K and $g_{BCS}N(0) = 0.3$[3]. The theoretical line for T_{c1} is given

by a solid line in Fig. 5.

In this paper we define the upper critical field H_{c2} as the field at which the electrical resistance begins to rise from zero with increasing magnetic field. The anisotropy of H_{c2}[31] is expected in the present crystal which has a tetragonal symmetry, and the anisotropy may induce a broad transition at the upper critical field in the polycrystalline specimen as seen in Figs. 2 and 3. Thus, our defined H_{c2} may correspond to a minimum value in the anisotropic H_{c2}. The temperature dependence of H_{c2} was measured in a whole concentration region and the results are shown in Fig. 6. H_{c2} in the Er doped compounds has a broad peak near 4 K and decreases with decreasing temperature. The decrease in H_{c2} at low temperatures is explained as follows[32]: in the mixed state the persistent current of vortices induces a magnetic field and this field polarizes the Er spin moments. Along the vortex current, the spin magnetization contributes to the magnetic flux. The total flux which is the sum of the spin and current contributions is quantized. Then this flux quantization leads to the following facts: the vortex current is drastically affected by the spin polarization of Er at low temperatures and the current inversion occurs in some part of the vortex. The current inversion causes the attractive force between the vortices. As the result, when the spin magnetization increases at low temperatures, the superconducting state becomes unstable and H_{c2} decreases. The sample with low concentrations of Er ions ($c = 0.3 \sim 0.17$) showed a clear small minimum of H_{c2} near 0.2 K as is shown in Fig. 6. It was noted in Fig. 6 that H_{c2}, in high concentration specimens with

c = 1.0 ∿ 0.8, decreases suddenly at T_{c2}. This sudden decrease in H_{c2} suggests the first order transition at T_{c2}[15]. It was also noted that the zero field resistance below T_{c2} is about 60 % of normal values and the positive magnetoresistance was observed as shown in Fig. 2. The origin of the reduced resistance below T_{c2} may be due to partially remained superconducting phase in polycrystalline sample. The reduction disappears by applying a magnetic field.

(2) Magnetization Measurements

Precise temperature dependences of magnetization in $ErRh_4B_4$ were measured between 0.5 K and about 2.0 K up to 29 kOe as shown in Figs. 7 and 8. In the case of H = 215 Oe, for example, the magnetization is negative and constant down to about 1.1 K due to the Meissner effect. Then the magnetization increases crossing the zero line and becomes constant below about 0.8 K. As the electrical resistance appears at 0.83 K with decreasing temperature in the same field, the induced magnetization may be due to the onset of the ferromagnetic transition. The transition temperature determined from the magnetoresistance is shown by open circles on the magnetization curve. When the temperature increases from about 0.5 K to about 2 K, a large hysteresis is observed. Generally speaking the magnetic moment persists even above T_{c2} determined from the magnetoresistance. The main part of the excess large magnetic moment observed under the increasing temperature may come from the residual vortecies persisted in the sample. However, the magnetization at H = 215 Oe shows a curious plateau

between 1 K and 1.4 K and this might reflect the existence of the helical spin ordering. The hysteresis decreases as the field increases and it is not observed above about 2 kOe. The magnetization curve under a strong field is shown in Fig. 8. The value of the induced magnetization at 0.5 K is about 6.5 μ_B/Er ion even at about 29 kOe and it is considerably smaller than that of 9.0 μ_B/Er expected from the ground state $^4I_{15/2}$ of Er^{3+}. We also tried to observe the high field magnetization curve by using the D-1 Magnet of The High Magnetic Field Laboratory, Osaka University and the results is given in Fig. 9.

The magnetization curves in $ErRh_4B_4$ at various temperature around T_{c2} were also measured by extracting sample method only in low field regions up to 3 kOe as shown in Fig. 10. The magnetic field in Fig. 10 means a measured field under the increasing field scan. In the low field region above 0.8 K, i.e., higher than T_{c2} the negative magnetization due to the Meissner effect is observed and the magnitude is $-H/4\pi$ up to H_{c1}. Above H_{c1} the Meissner state is destroyed and the magnetization begins to increase as shown in Fig. 10. Therefore, the magnetization curve shows the minimum at the critical field H_{c1}. The temperature dependence of H_{c1} is shown in Fig. 11. The determination of H_{c1} in these material is usually very difficult. However, we can find it because the fluxgate magnetometer is very sensitive even at low field region. In Fig. 11, H_{c2} obtained by the magnetoresistance measurments is also given. It is noticed that all magnetization curves below T_{c2} does not show the temperature dependence. Simply speaking, the magnetization curve looks like a paramagnetic magneti-

zation. There is no hysteresis loop. If the crystal has the domain structure such as usual ferromagnets, a large hysteresis should be expected in the magnetization curve. The reason is not clear yet.

The hysteresis curve in $ErRh_4B_4$ above T_{c2} at 1.33 K, where the hysteresis is largest, is shown in Fig. 12. In the virgin state, the magnetization is diamagnetic below H_{c1} due to the Meissner effect. Above H_{c1} the vortex state is stabilized between H_{c1} and H_{c2}. As seen in the usual type II superconductors the vortex state is irreversible to magnetic field. Therefore, once the vortex state is stabilized, the vortices are trapped and remain in the specimen after removing the magnetic field. The hysteresis curve in Fig. 12 may be explained by the vortex trapping. The hysteresis decreases as temperature increases and diminishes at T_{c2}.

§ 5 Concluding Discussions

Electrical and magnetic properties of $ErRh_4B_4$ and the mixed crystal with YRh_4B_4 are studied and many informations are obtained as are summerized below. The first aim of the present paper is to find the concentration dependences of T_{c1}, T_{c2} and H_{c2} in the mixed crystals and to check the recent theory of Maekawa and Tachiki[3]. The agreement with the theory is satisfactory except the dilute region of Er. $I^2N(0)$ was obtained to be 0.046 K from the concentration dependence of T_{c1}. This value means that the exchange coupling between localized 4f electron of Er^{3+} and super-

conducting 4d electrons of Rh is very weak. This means that the localized magnetic moment does not give a strong influence upon the superconducting electrons. However, the magnetic coupling between 4f electrons via 6s band is not so weak and the ferromagnetic order below T_{c2} may occur due to the indirect coupling and the superconducting state may be destroyed by this magnetization. This model was proposed by Maekawa and Tachiki[3] and our experimental results does not contradict to their theory. In pure $ErRh_4B_4$, the temperature dependence of H_{c2} suggests the first order transition near 0.8 K. However, the confirmation is difficult by looking at H_{c2} only.

The temperature dependence of H_{c1} is obtained in pure $ErRh_4B_4$ down to its ferromagnetic critical temperature T_{c2}. This can be obtained by using the fluxgate magnetometer which is very effective even in a very weak field.

As predicted by the theory[15),16),17),18)] and suggested by neutron scattering data[13),14),19)], some anomalous behaviors in magnetoresistance, magnetization curve etc. should be expected if the helical spin order appears near T_{c2}. We found an anomalous large hysteresis and a curious plateau in the magnetization curve between 1.0 K and 1.4 K. This may suggest the coexistence of the helical spin order in the superconducting state. However, the low field magnetization curve around this temperature region does not show any anomalies. It is also curious that the anomalous magnetization plateau in decreasing temperature can not be found. In the ferromagnetic state, the magnetization curve does not show the hysteresis. This means that the remanence is negligibly small.

It is also interesting that the magnetization curve does not show a steep increase but show a gradual, say a paramagnetic, magnetization. The high field magnetization up to 360 kOe was also measured but a large increase in magnetization was not found.

Finally, one must say about the necessity of the single crystal experiment. We now have no informations about the magnetic anisotropy of the ferromagnetic state, the domain structure and the electrical conductivity tensor. These are very important for investigating the further details of the magnetic and electrical properties of these compounds. We once tried to make a single crystal with aid of Professor T. Komatsubara in Tohoku University. However, no good single crystals were obtained. It is still doubtful whether one can make a good single crystal in the series of the mixed $Er_cY_{1-c}Rh_4B_4$ compound or not.

References

1) W. A. Fertig, D. C. Johnston, L. E. DeLong, R. W. McCallum, M. B. Maple and B. T. Matthias : Phys. Rev. Lett. 38 (1977) 987.

2) M. Ishikawa and Ø. Fischer : Solid State Commun. 23 (1977) 37.

3) S. Maekawa and M. Tachiki : Phys. Rev. B18 (1978) 4688.

4) D. E. Moncton, G. Shirane, W. Thomlinson, M. Ishikawa and Ø. Fischer : Phys. Rev. Lett. 41 (1978) 1133.

5) W. Thomlinson, G. Shirane, D. E. Moncton, M. Ishikawa and Ø. Fischer : J. Appl. Phys. 50 (1979) 1981.

6) C. F. Majkrzak, G. Shirane, W. Thomlinson, M. Ishikawa, Ø. Fischer and D. E. Moncton : Solid State Commun. 31 (1979) 773.

7) M. Ishikawa and Ø. Fischer : Solid State Commun. 24 (1977) 747.

8) R. W. McCallum, D. C. Johnston, R. N. Shelton and M. B. Maple Solid State Commun. 24 (1977) 391.

9) R. W. McCallum, D. C. Johnston, R. N. Shelton, W. A. Fertig and M. B. Maple : Solid State Commun. 24 (1977) 501.

10) H. R. Ott, W. A. Fertig, D. C. Johnston, M. B. Maple and B. T. Matthias : J. Low Temp. Phys. 33 (1978) 159.

11) H. B. MacKay, L. D. Woolf, M. B. Maple and D. C. Johnston : Phys. Rev. Lett. 42 (1979) 918.

12) L. D. Woolf, D. C. Johnston, H. B. MacKay, R. W. McCallum and M. B. Maple : J. Low Temp. Phys. 35 (1979) 651.

13) D. E. Moncton, D. B. McWhan, J. Eckert, G. Shirane and W.

Thomlinson : Phys. Rev. Lett. 31 (1977) 1164.

14) D. E. Moncton : J. Appl. Phys. 50 (1979) 1990.

15) H. Matsumoto, H. Umezawa and M. Tachiki : Solid State Commun. 31 (1979) 157.

16) E. I. Blount and C. M. Varma : Phys. Rev. Lett. 42 (1979) 1079.

17) L. N. Bulaevski, A. I. Rusinov and M. Kulić : Solid State Commun. 30 (1979) 59.

18) M. V. Jarić and M. Belić : Phys. Rev. Lett. 42 (1979) 1015.

19) D. E. Moncton, G. Shirane and W. Thomlinson : International Conference of Magnetism (München) 1979.

20) J. M. Vandenberg and B. T. Matthias : Proc. Natl. Acad. Sci. USA 74 (1977) 1336.

21) Ø. Fischer, A. Treyvand, R. Chevrel and M. Sergent : Solid State Commun. 17 (1975) 721.

22) R. N. Shelton, R. W. McCallum and H. Adrin : Phys. Lett. 56A (1976) 213.

23) D. C. Johnston, W. A. Fertig, M. B. Maple and B. T. Matthias : Solid State Commun. 26 (1978) 141.

24) Ø. Fischer : Proceedings of the 14th International Conference on Low Temperature Physics (Otaniemi, Finland, 1975) Vol. V p172.

25) T. Jarlborg, A. J. Freeman and T. J. Watson-Yang : Phys. Rev. Lett. 39 (1977) 1032.

26) A. J. Freeman and T. Jarlborg : J. Appl. Phys. 50 (1979) 1876.

27) G. K. Shenoy, B. D. Dunlap, F. Y. Fradin, C. W. Kimball, W.

Potzel, F. Probst and G. M. Kalvius : J. Appl. Phys. 50 (1979) 1872.

28) H. A. Eick and P. W. Gilles : J. Chem. Phys. 81 (1959) 5030.

29) T. Oguchi and T. Obata : J. Phys. Soc. Jpn. 27 (1969) 1111.

30) A. A. Abrikosov and L. P. Gor'kov : Soviet Phys. JETP 12 (1961) 1243.

31) M. Decroux, Ø. Fischer, R. Flukiger, B. Seeber, R. Delesclefs and M. Sergent : Solid State Commun. 25 (1978) 393.

32) M. Tachiki, H. Matsumoto and H. Umezawa : Phys. Rev. 20 (1979) 1915.

Figure Caption

Fig. 1. Crystal structure of $(RE)Rh_4B_4$.

Fig. 2. Magnetoresistance curves of $Er_cY_{1-c}Rh_4B_4$ with c = 0.17, 0.44 and 1.00 at 80 mK. $R_{max.}$ means the resistance in the normal state at high fields.

Fig. 3. Magnetoresistance curves of $Er_{0.44}Y_{0.56}Rh_4B_4$ as a parameter of temperature.

Fig. 4. Temperature dependences of the magnetoresistance in various fields in $Er_cY_{1-c}Rh_4B_4$ with c = 1.00, 0.44 and 0.17.

Fig. 5. Concentration dependences of T_{c1} and T_{c2} in $Er_cY_{1-c}Rh_4B_4$. Open and black circles denote T_{c1} and T_{c2}, respectively.

Fig. 6. Temperature dependence of H_{c2} in $Er_cY_{1-c}Rh_4B_4$ as a parameter of Er concentration.

Fig. 7. Temperature dependence of magnetization around T_{c2} in $ErRh_4B_4$ in low magnetic field region. The phase boundaries between paramagnetic and superconducting phase, and ferromagnetic and normal phase are shown by the solid lines (open circles mean the ferromagnetic transition temperatures with decreasing temperatures and squares mean that with increasing temperatures).

Fig. 8. Temperature dependence of magnetization around T_{c2} in $ErRh_4B_4$ in high magnetic field region up to 29 kOe.

Fig. 9. Magnetization curves in $ErRh_4B_4$ under the high magnetic field up to 360 kOe at 4.2 K and 1.3 K.

Fig. 10. Low field magnetization curves of $ErRh_4B_4$ at various temperatures obtained by extracting sample method.

Fig. 11. Temperature dependences of H_{c1} and H_{c2} in $ErRh_4B_4$.

Fig. 12. Hysteresis curve in $ErRh_4B_4$ at 1.33 K.

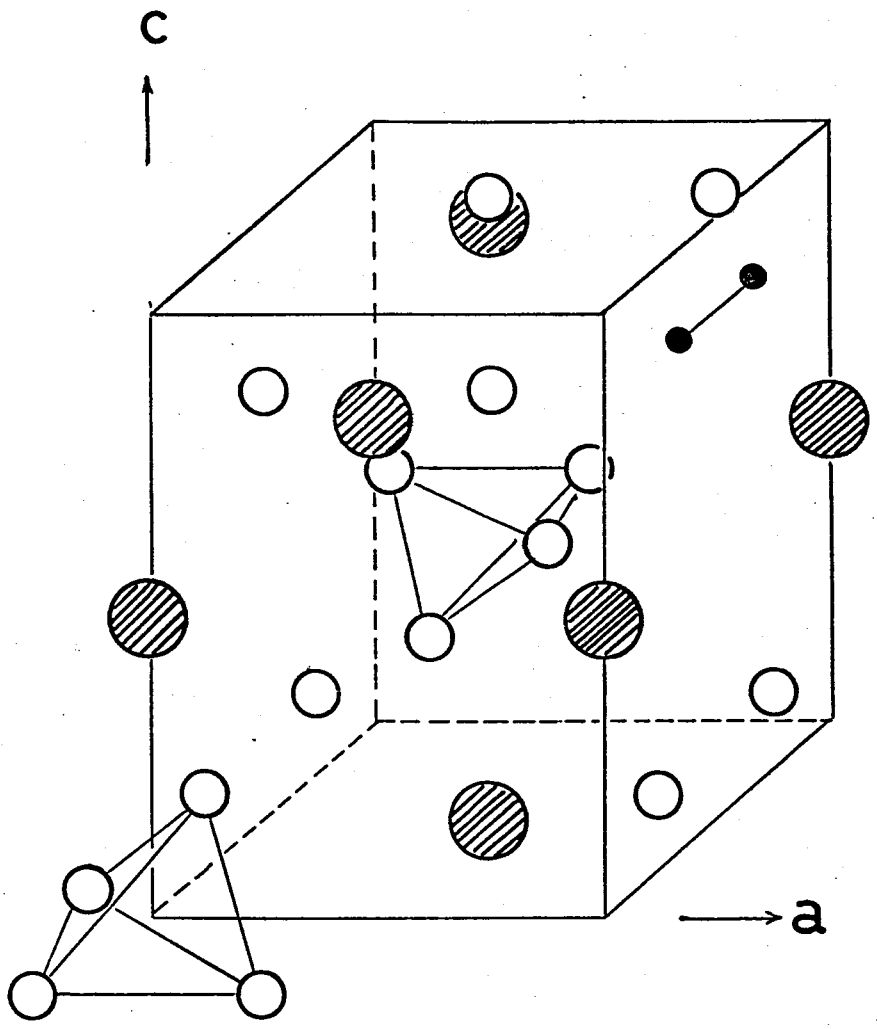

RE ○ Rh • B

space group $P_{42/nmc}$

RE = Y, Nd, Sm, Gd, Tb, Dy, Ho
Er, Tm, Lu, Th

Fig.1

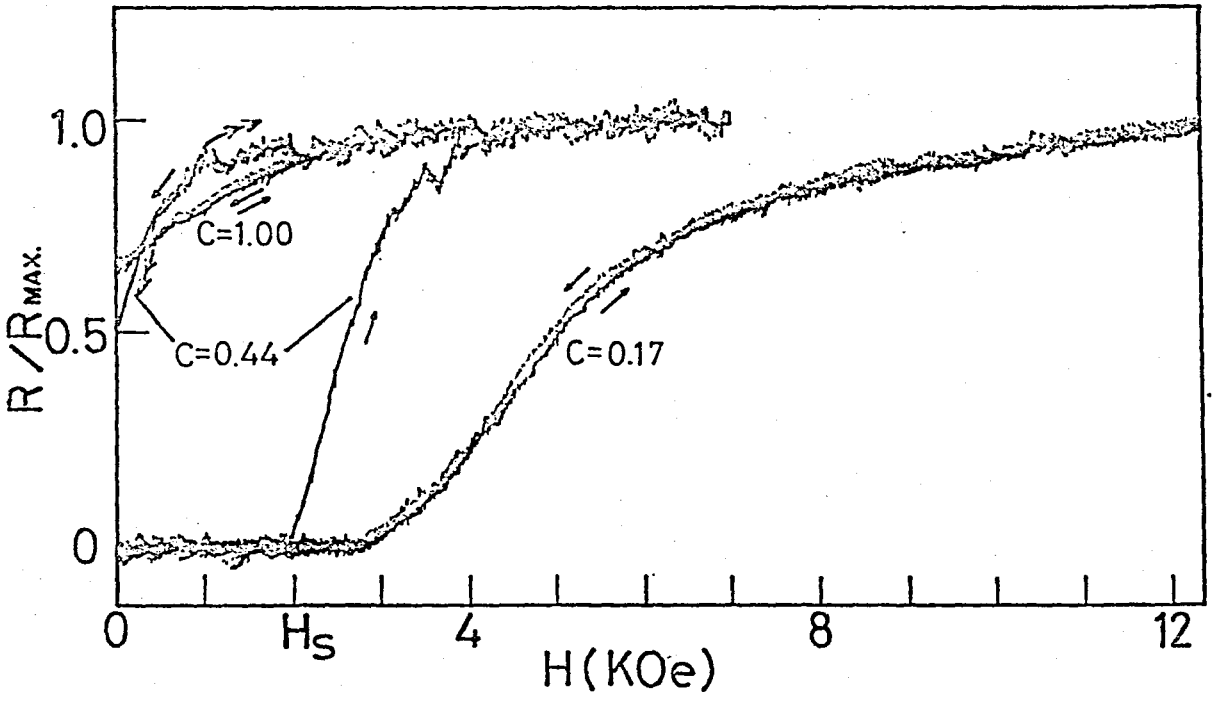

Fig. 2

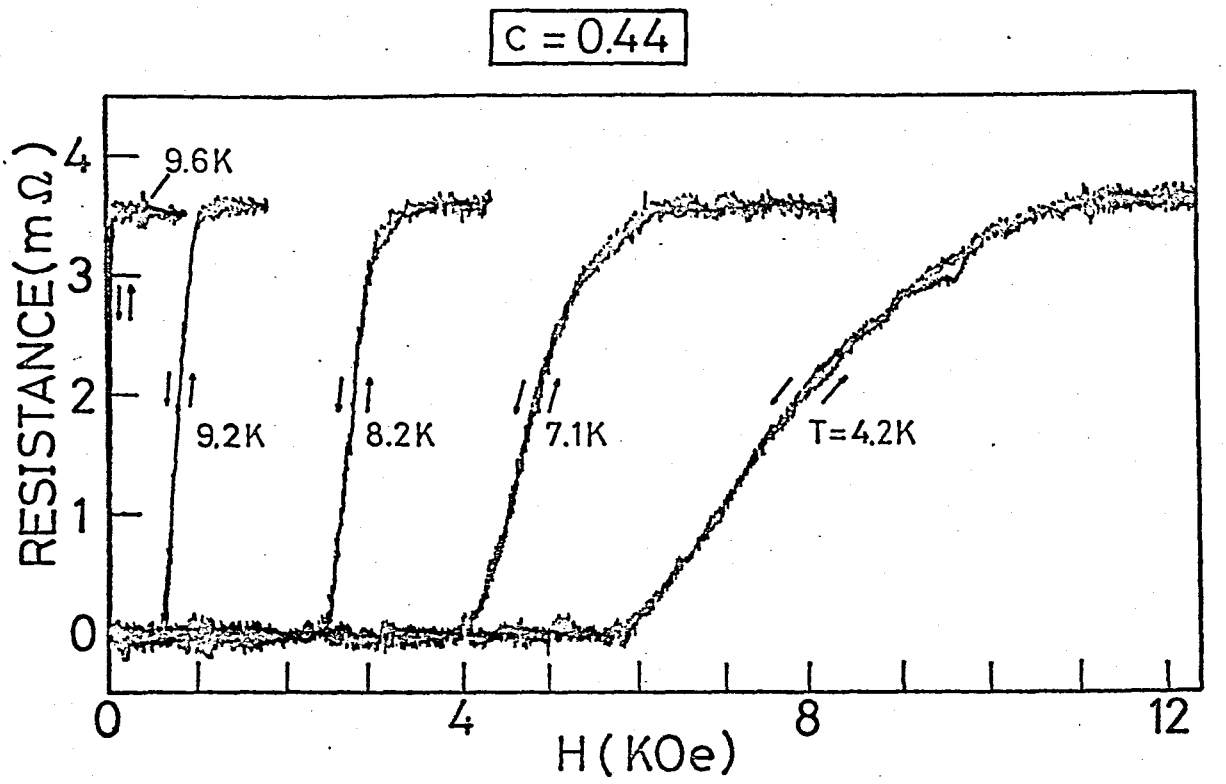
c = 0.44
RESISTANCE(mΩ)
4
3
2
1
0
9.6K
9.2K
8.2K
7.1K
T=4.2K
0
4
8
12
H (KOe)

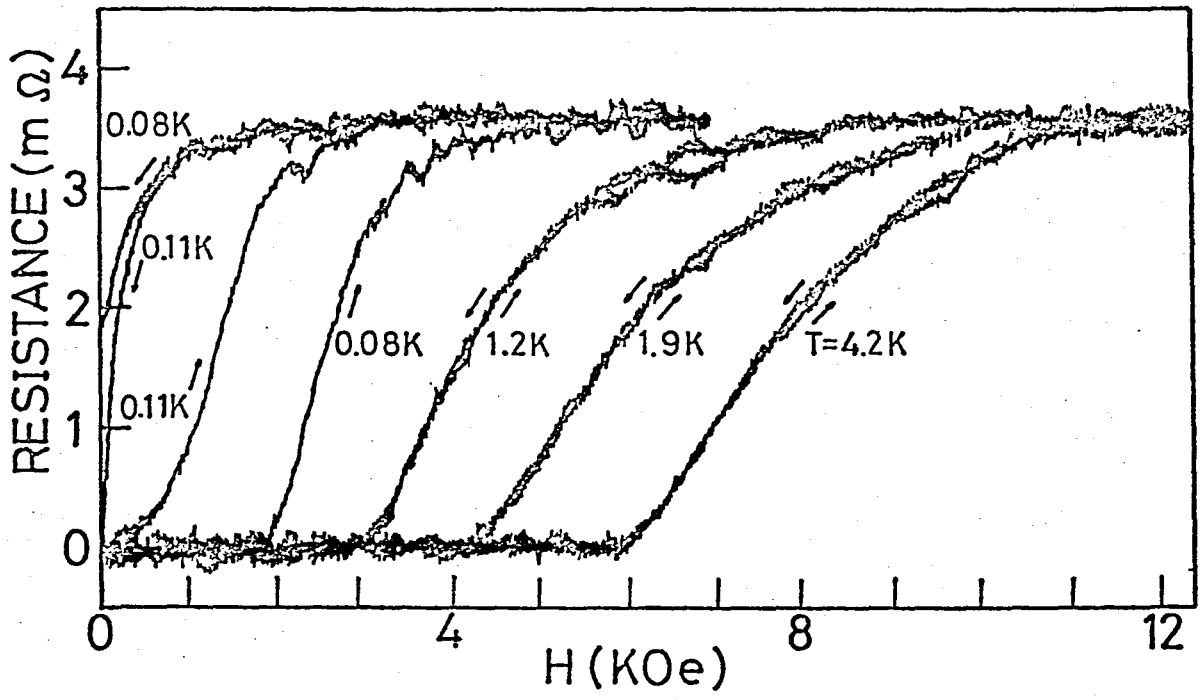
RESISTANCE (mΩ)
4
3
2
1
0
0.08K
0.11K
0.11K
0.08K
1.2K
1.9K
T=4.2K
0
4
8
12
H (KOe)

Fig. 3

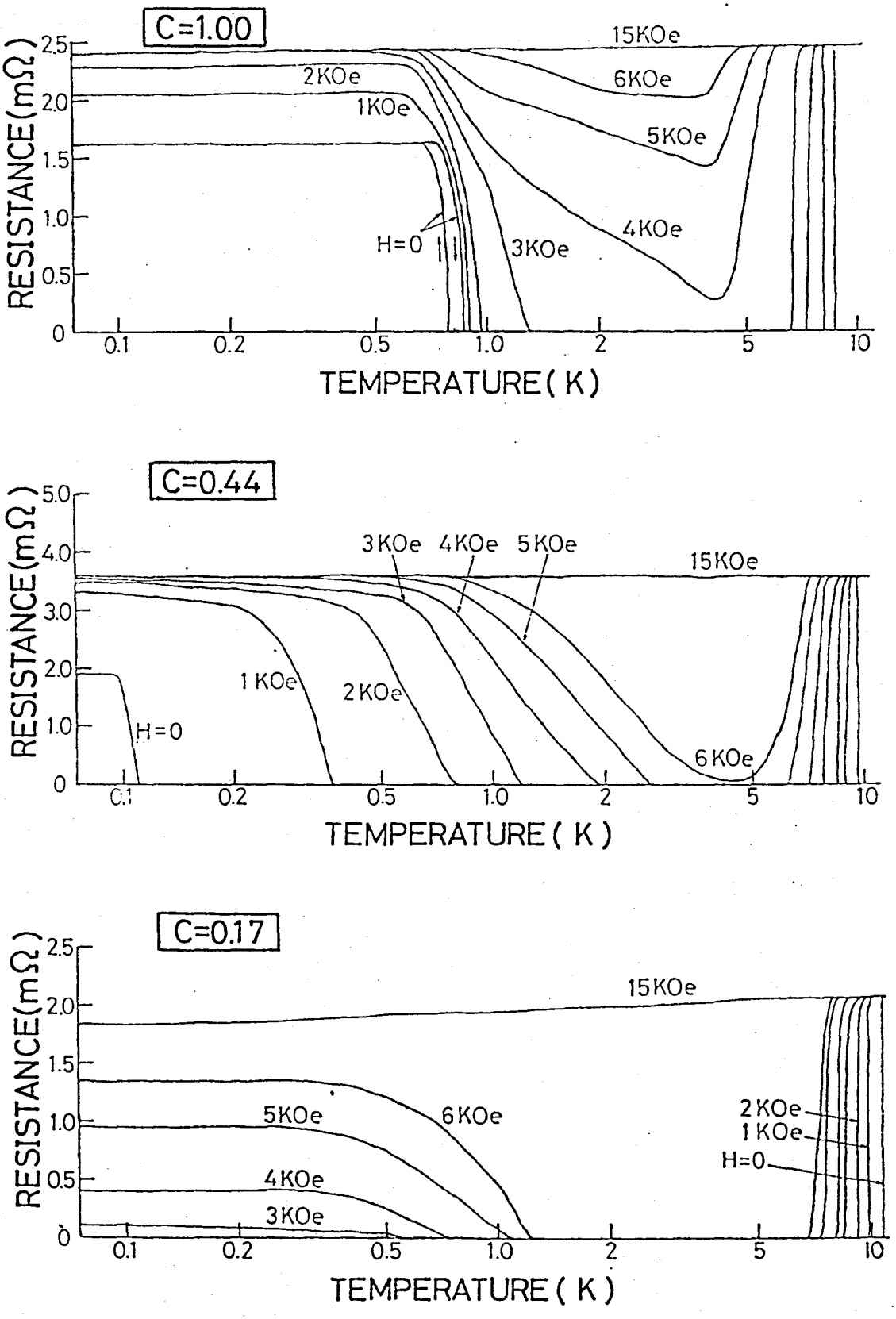
C=1.00
15KOe
2KOe
6KOe
1KOe
5KOe
4KOe
H=0
3KOe
RESISTANCE(mΩ)
TEMPERATURE(K)
C=0.44
3KOe 4KOe 5KOe
15KOe
1 KOe
2KOe
H=0
6KOe
RESISTANCE(mΩ)
TEMPERATURE (K)
C=0.17
15KOe
5KOe
6KOe
2KOe
1KOe
H=0
4KOe
3KOe
RESISTANCE(mΩ)
TEMPERATURE (K)

Fig. 4

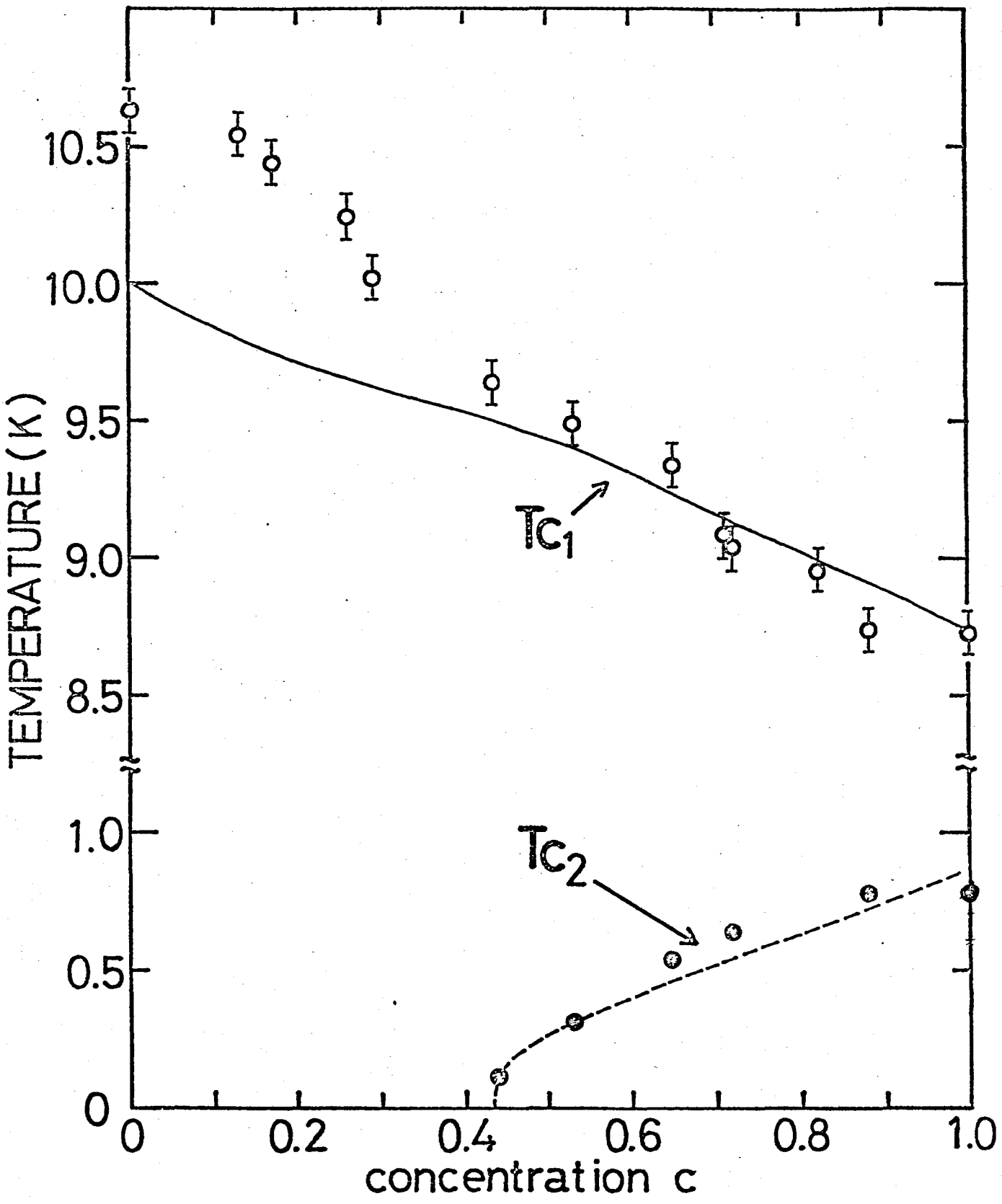
10.5
10.0
9.5
9.0
8.5
1.0
0.5
0
TEMPERATURE (K)
Tc1
Tc2
0
0.2
0.4
0.6
0.8
1.0
concentration c

Fig.5

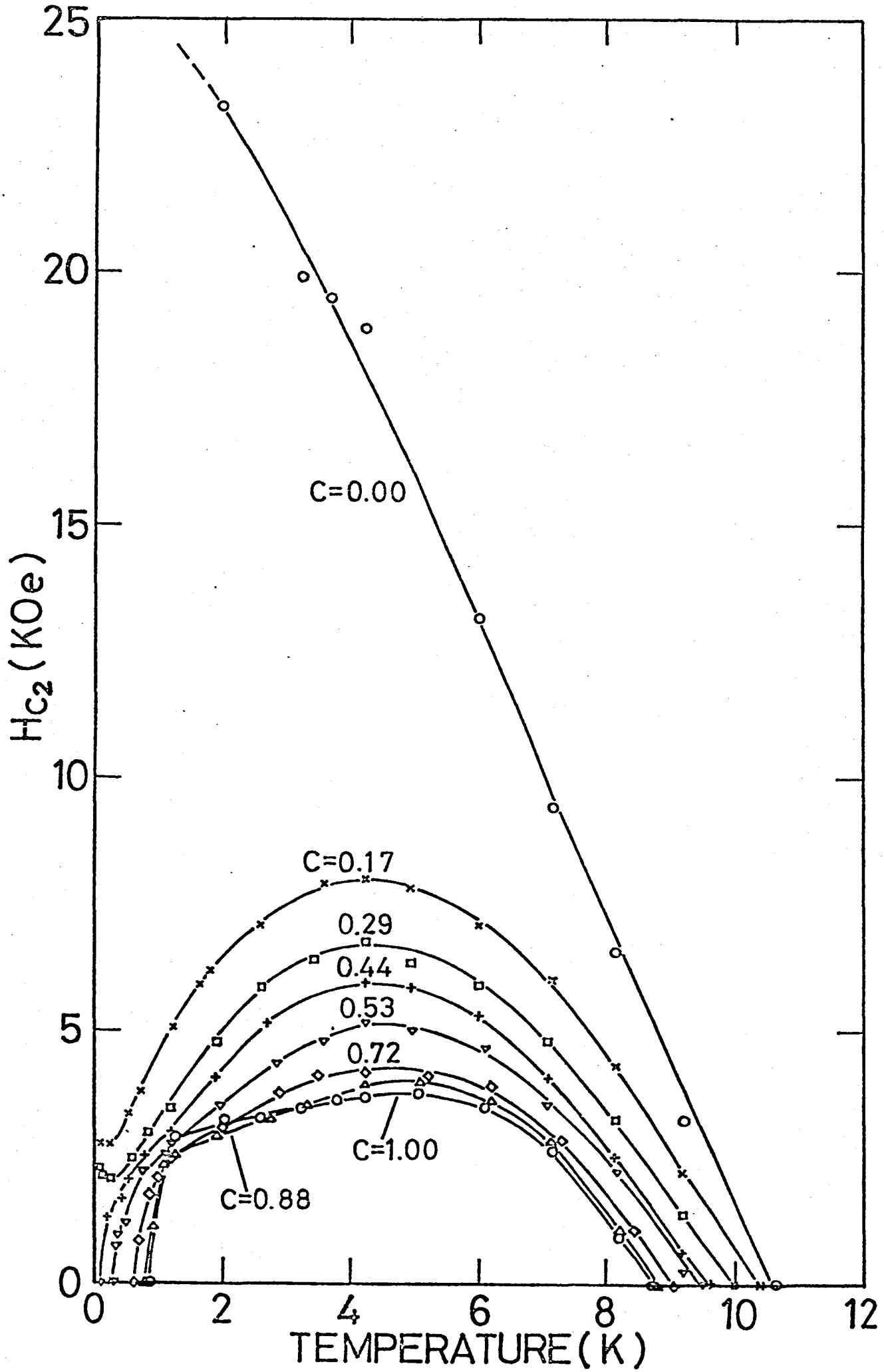
25
20
15
10
5
0
0
2
4
6
8
10
12
H_{c_2} (KOe)
TEMPERATURE (K)
C=0.00
C=0.17
0.29
0.44
0.53
0.72
C=1.00
C=0.88

Fig. 6

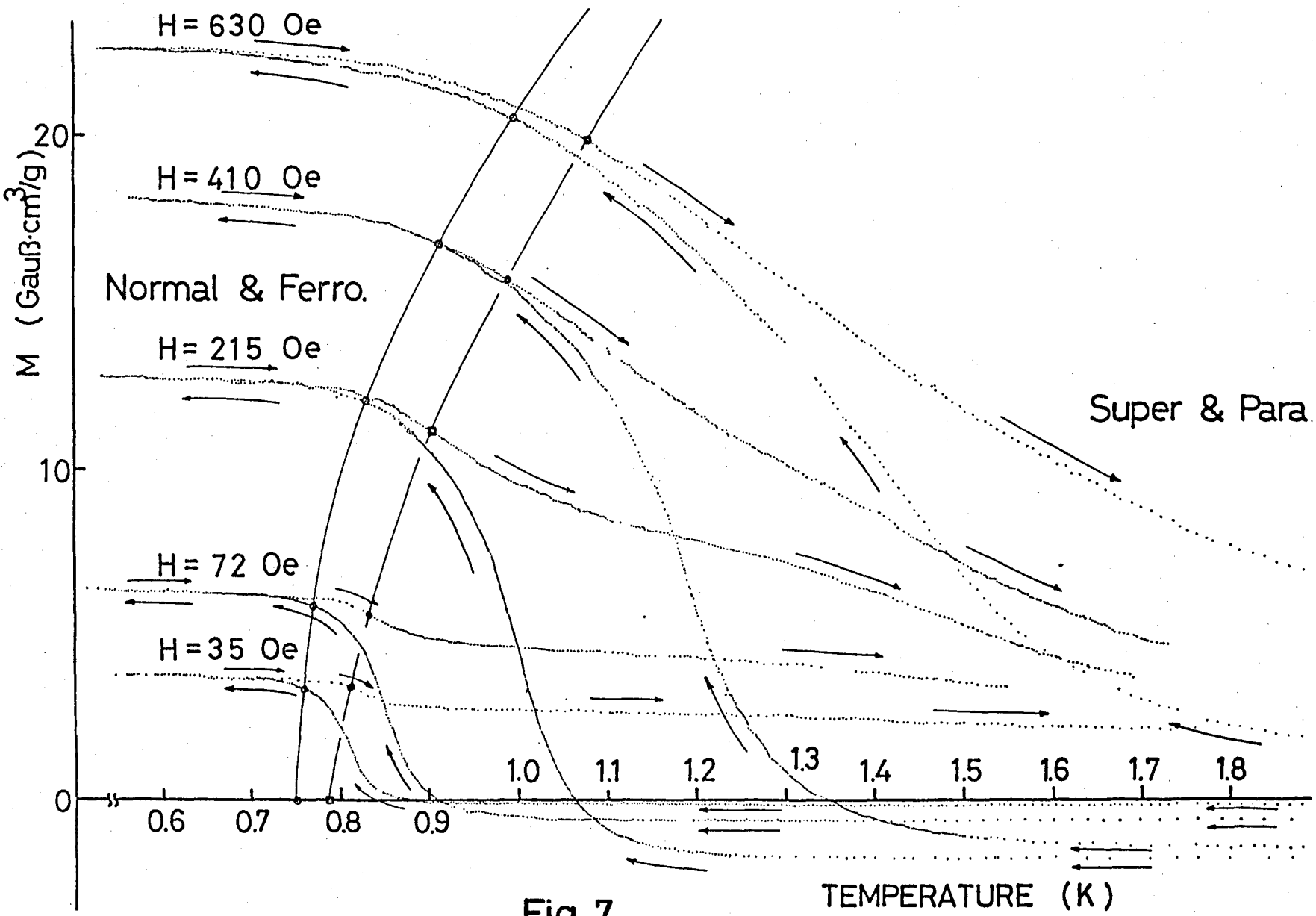
H= 630 Oe
H= 410 Oe
Normal & Ferro.
H= 215 Oe
Super & Para
H= 72 Oe
H= 35 Oe
M (Gauß·cm³/g)
20
10
0
0.6
0.7
0.8
0.9
1.0
1.1
1.2
1.3
1.4
1.5
1.6
1.7
1.8
TEMPERATURE (K)

Fig. 7

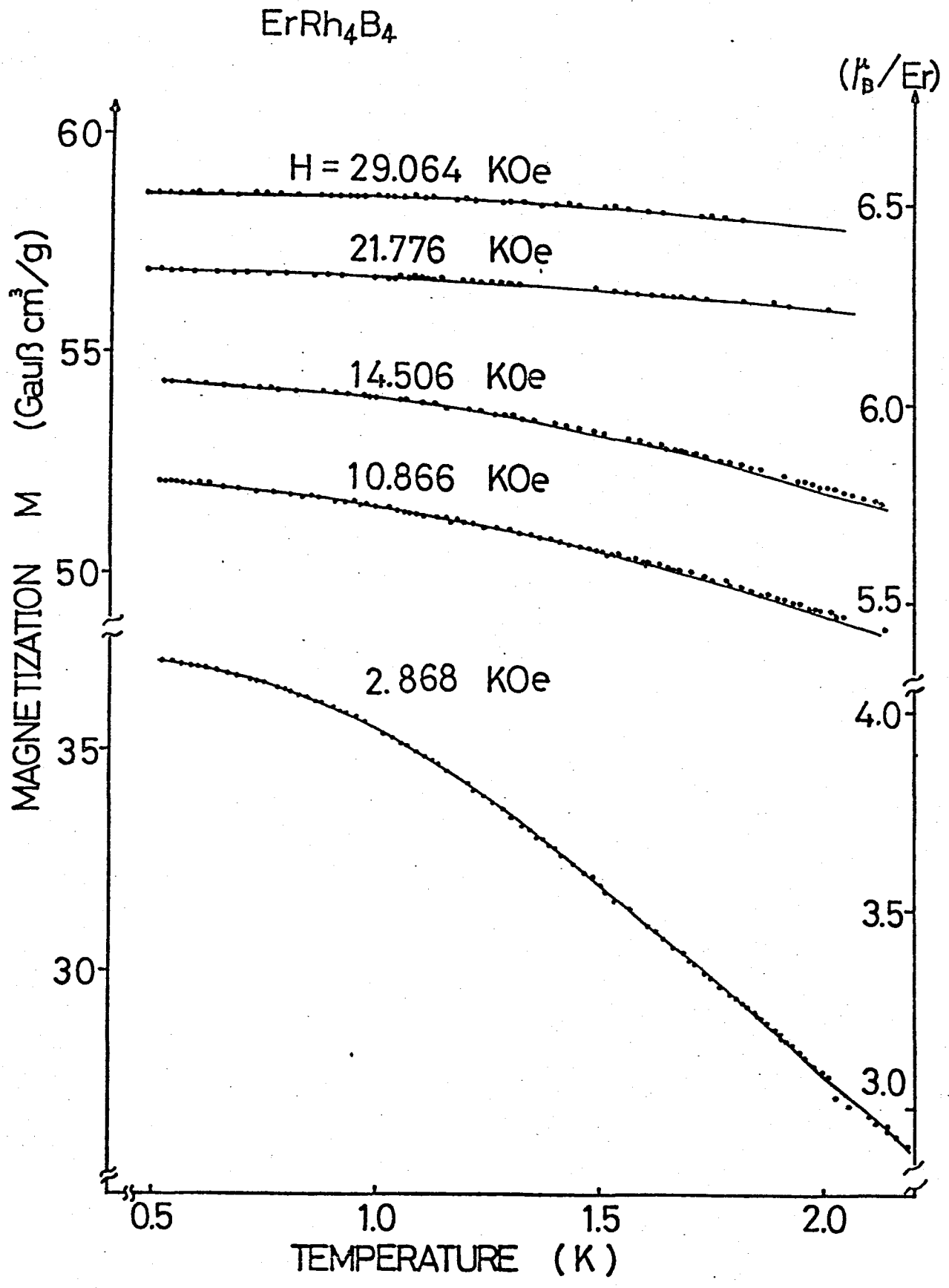
ErRh4B4
(μB/Er)
H = 29.064 KOe
21.776 KOe
14.506 KOe
10.866 KOe
2.868 KOe
MAGNETIZATION M (Gauß cm³/g)
60
55
50
35
30
6.5
6.0
5.5
4.0
3.5
3.0
0.5
1.0
1.5
2.0
TEMPERATURE (K)

Fig. 8

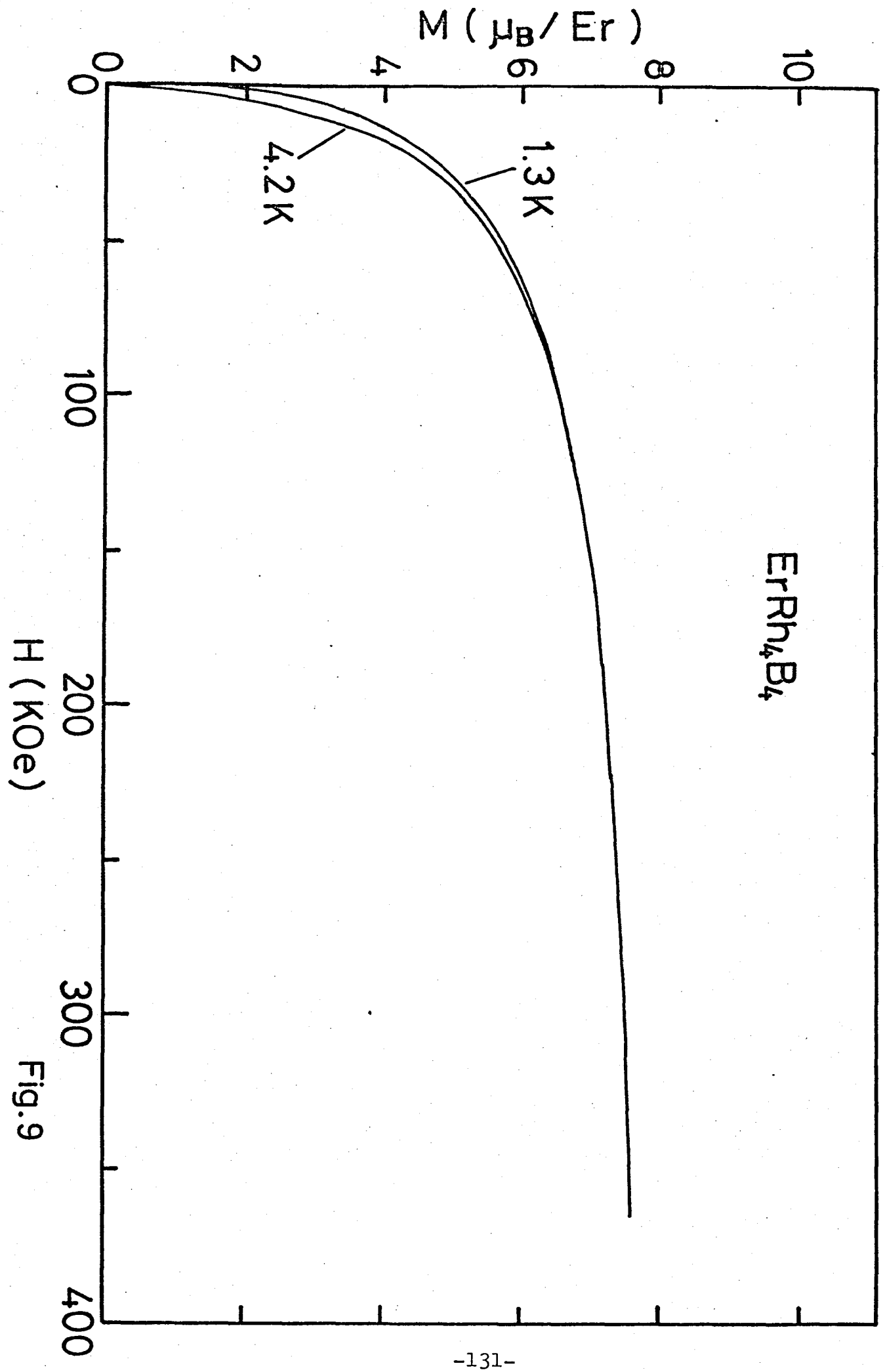

Fig.9

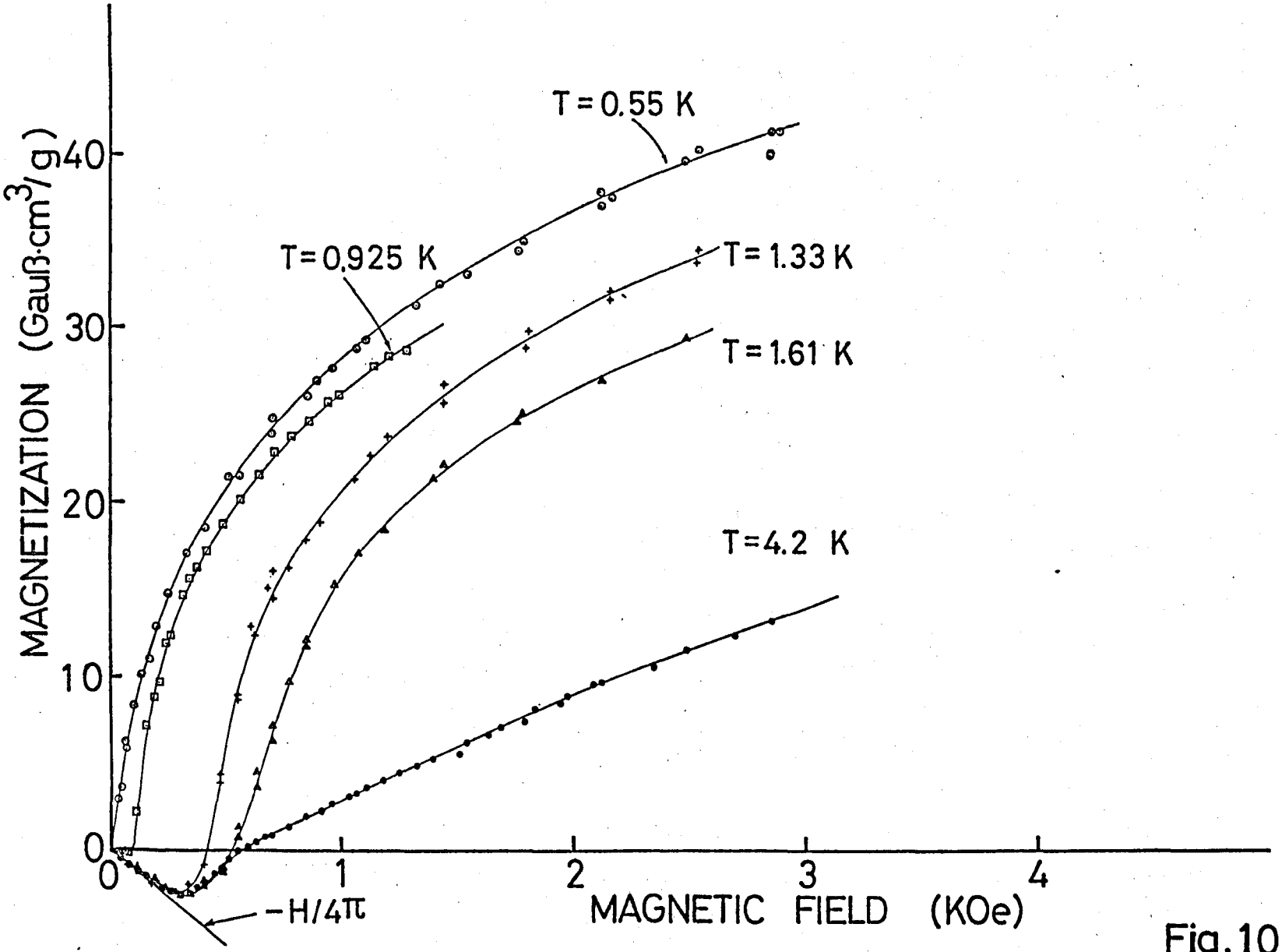
T = 0.55 K
T = 0.925 K
T = 1.33 K
T = 1.61 K
T = 4.2 K
MAGNETIZATION (Gauß·cm³/g)
40
30
20
10
0
0
1
2
3
4
MAGNETIC FIELD (KOe)
−H/4π

Fig.10

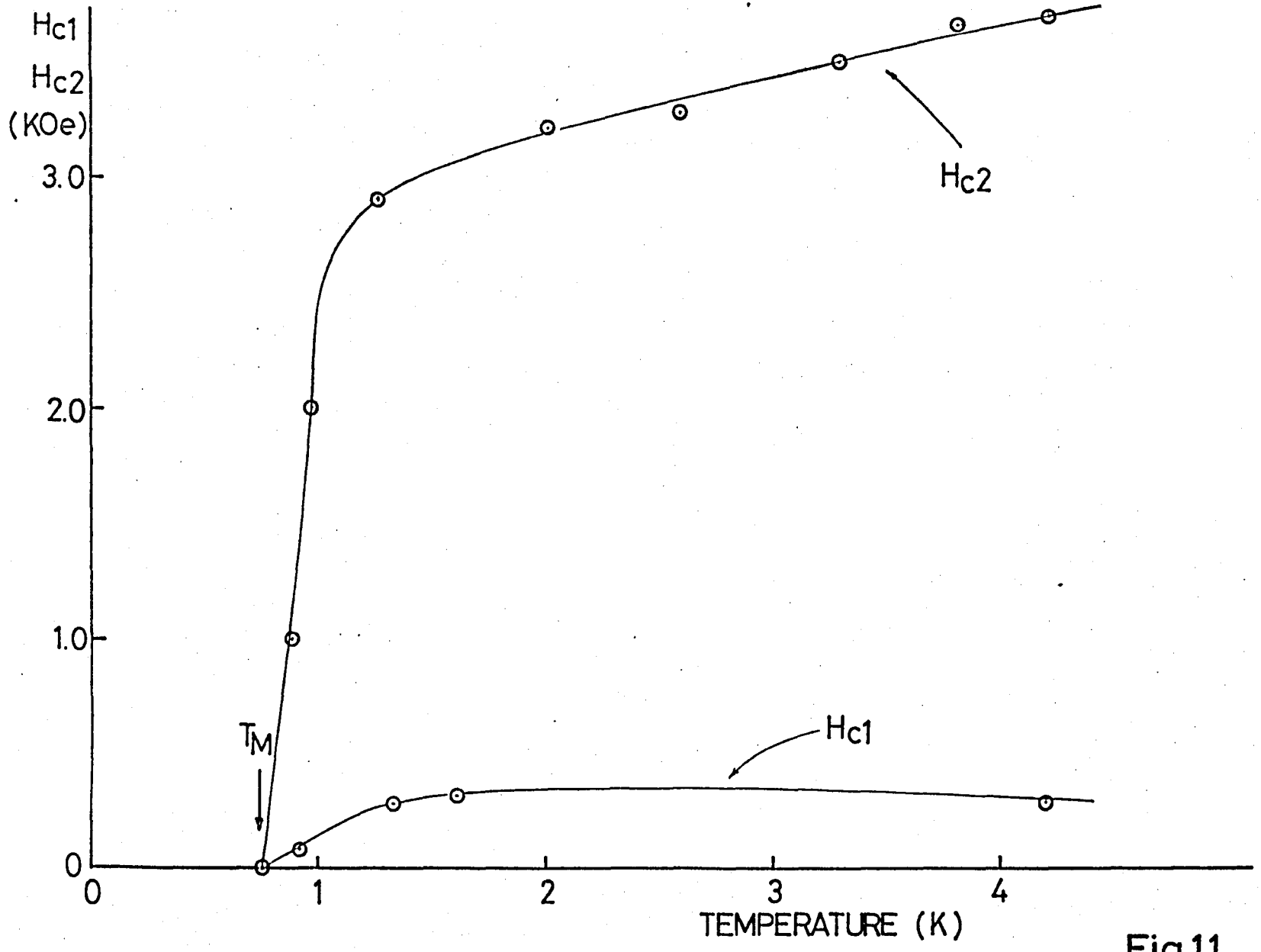

Fig.11

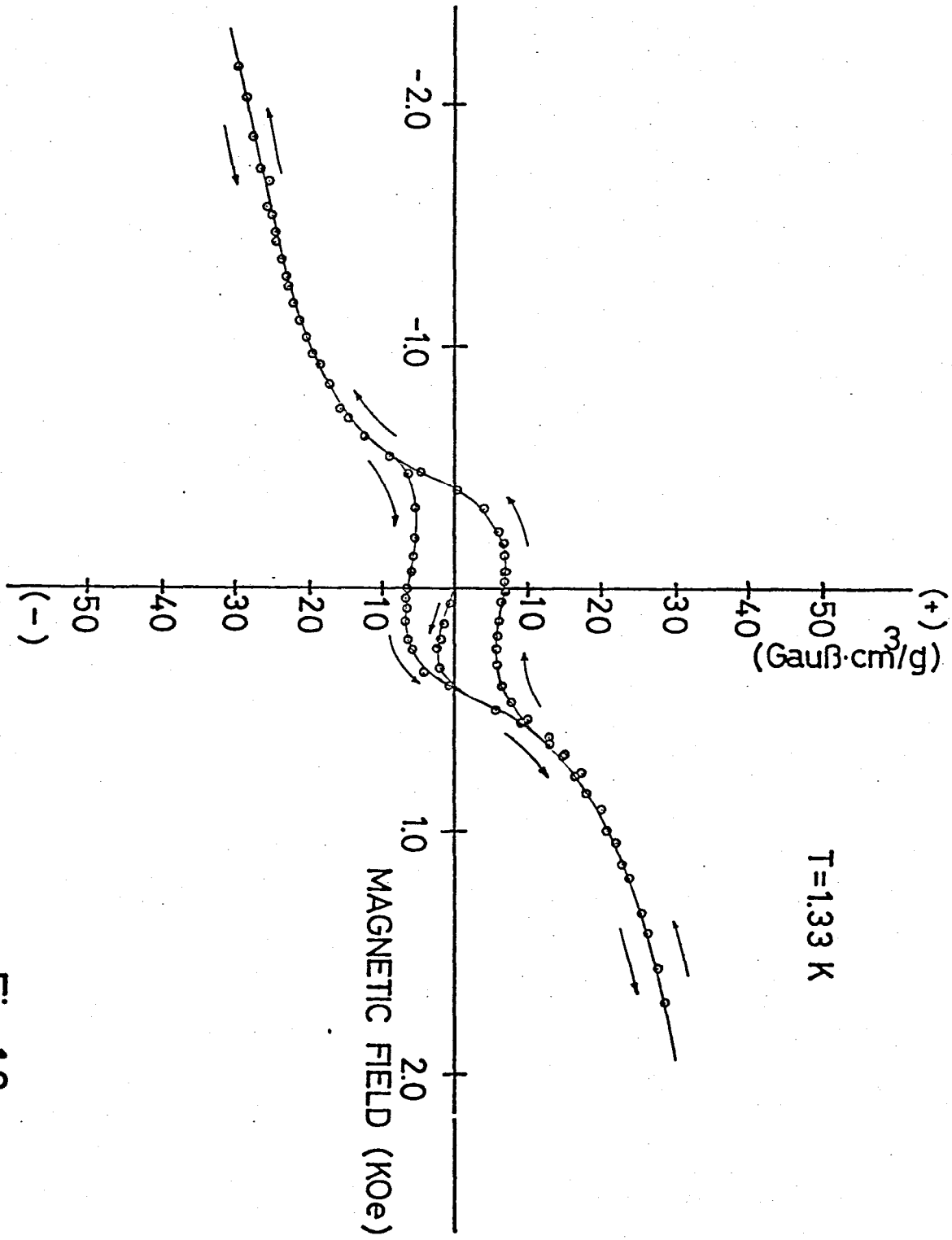
-2.0
-1.0
1.0
2.0
MAGNETIC FIELD (KOe)
(+)
(-)
-50
-40
-30
-20
-10
10
20
30
40
50
(Gauß·cm³/g)
T=1.33 K

Fig.12

Acknowledgement

The present author wishes to express his sincere gratitude to Professor Muneyuki Date for suggesting this topics of his dissertation and continuous encouragement and enlightening discussions during all phases of this study.

He is indebted to Associate Professor Kiichi Okuda as a collabolator and thanks for his valuable suggestions and discussions through this course of study.

He is also indebted to Dr. Kokichi Oshima for initial construction of the ESR cryostat in ^{3}He stage and also thanks to Mr. Yukinori Nakakura for making the sample of $Er_cY_{1-c}Rh_4B_4$.

He also thanks to all members of Date Laboratory for helpful discussions.